GALACTIC GAMMA-RAY EMISSION FROM DISCRETE AND DIFFUSE SOURCES

Thesis submitted for the degree of Doctor of Philosophy of the University of London

by

Christopher Edward Roff

Blackett Laboratory
Imperial College of
Science and Technology
London SW7 2BZ

1982

ABSTRACT

The scientific potential of gamma-ray astronomy has long been recognised because of its direct relationship to astrophysical processes involving high energy electrons and protons and because the high penetrating power of gamma rays enables them to reach the Earth from many parts of the Galaxy or universe. The first unambiguous detection of celestial gamma rays was made by Kraushaar et al (1972), who observed gamma rays from the Galactic disc with a peak intensity towards the Galactic centre. In order to measure the spectrum of the Galactic gamma emission, a series of balloon flights was carried out by the Imperial College group. The flights took place over Australia using instruments designed to detect gamma photons in the energy range $0.2<E<5.0$ GeV.

Results from the 1973 flight and the two 1975 flights are presented here. The results from the Galactic plane are consistent with the emission spectrum as reported by COS-B. Upper limits on the emission of various possible sources of gamma rays are quoted.

In the final chapter, the possible pulsar contribution to the Galactic gamma-ray emission is examined. This study was prompted following the detection of pulsed gamma radiation from the Crab and Vela radio pulsars. Using the latest pulsar data from the Molonglo Radio Observatory, Australia, the contribution is estimated to be $\lesssim 10\%$.

ACKNOWLEDGEMENTS

I am very grateful to Professor H. Elliot for the opportunity of studying in his group and I would like to thank my supervisor Dr G.K. Rochester for his invaluable guidance and interest throughout this project.

I would also like to thank Dr R.K. Sood, Dr B.T. Thomas and Mr J.B. Hughes for their assistance and support during this project.

I am grateful to the Department of Science, Australia for the use of the balloon launching facilities and to the members of the Balloon Launching Station, Mildura, for the successful balloon launches.

I am indebted to the Science Research Council for a Postgraduate Studentship.

Finally I would like to thank my family for their support and encouragement during the writing of this thesis.

CONTENTS

LIST OF FIGURES AND TABLES

Figure 5.3 Altitude as a function of local time for the three flights.

5.4a Gamma-ray production/gm atmospheric depth in the energy range $0.2<E_\gamma< 0.7$ GeV.

5.4b Gamma-ray production/gm atmospheric depth in the energy range $0.7<E_\gamma<1.0$ GeV.

5.4c Gamma-ray production/gm atmospheric depth in the energy range $1.0<E_\gamma<2.0$ GeV.

5.4d Gamma-ray production/gm atmospheric depth in the energy range $2.0<E_\gamma<3.0$ GeV.

5.4e Gamma-ray production/gm atmospheric depth in the energy range $3.0<E_\gamma<5.0$ GeV.

5.5 Atmospheric gamma-ray spectrum at 8.8 GeV cut-off rigidity compared with the π° decay theory of Perola and Scarsi together with a contribution from bremsstrahlung.

5.6 Comparison of the atmospheric spectrum measured by various experimenters, normalised to 4.5 GeV cut-off, 1 gm/cm^2 and solar minimum conditions.

5.7a Depth curve for atmospheric gamma-rays in the energy range $0.2<E<0.7$ GeV.

5.7b Depth curve for atmospheric gamma-rays in the energy range $0.7<E<1.0$ GeV.

5.7c Depth curve for atmospheric gamma-rays in the energy range $1.0<E<2.0$ GeV.

5.7d Depth curve for atmospheric gamma-rays in the energy range $2.0<E<3.0$ GeV.

5.7e Depth curve for atmospheric gamma-rays in the energy range $3.0<E<5.0$ GeV.

5.8 Gamma fluxes as a function of Galactic latitude for the 1973 flight before correction was made for atmospheric effects.

5.9 Gamma fluxes as a function of Galactic latitude for the 1975 I flight before correction was made for atmospheric effects.

5.10 Gamma fluxes as a function of Galactic latitude for the 1975 II flight before correction was made for atmospheric effects.

5.11 Gamma fluxes as a function of Galactic latitude for the 1973 flight after correcting for atmospheric effects.

Figure 6.7 Radio efficiency plotted against apparent age for the observed pulsars.

6.8a Radio efficiency of pulsars as a function of age.

6.8b Gamma efficiency of pulsars as a function of age.

6.9 COS-B observations of high energy gamma-rays plotted as a function of Galactic longitude and compared with the combined gamma emissions expected from pulsars and cosmic ray interactions with atomic and molecular hydrogen.

Table 6.1 Density values on the equatorial plane as a function of galactocentric radius.

CHAPTER I

INTRODUCTION

1.1 Introduction

Gamma-ray astronomy is the study of the most energetic photons originating in our Galaxy and beyond. The scientific potential of gamma-ray astronomy was first recognised in the early 50's. For example, in 1952, Hayakawa (1952) pointed out the effect of meson-producing nuclear interactions between cosmic rays and interstellar gas. In the same year, Hutchinson (1952) discussed the production of bremsstrahlung radiation by cosmic-ray electrons. However, the experimental development of gamma-ray astronomy was probably initiated by an important article from Morrison (1958), who predicted that a large gamma flux should be measurable near the Earth. Morrison pointed out that the most important processes for producing cosmic gamma rays were 1) pion decay, 2) bremsstrahlung, 3) inverse Compton effect and 4) synchrotron radiation. (These processes are reviewed in the following sections.)

Gamma radiation is the secondary product of various interactions between relativistic particles and matter, photons and fields. Gamma rays have a low interaction cross-section and suffer negligible absorption as they proceed along straight paths from their sites of origin. To illustrate the penetrating power, a 1 GeV gamma ray travelling along the diameter of the Galactic plane has only a 1% chance of interacting. A 1 GeV gamma ray from any part of the Universe also has only a $\lesssim$ 1% chance of interacting. Because of this high penetrating power and the direct relationship of gamma rays

to nuclear reactions involving high energy protons and electrons, gamma-ray observations may help to solve many astrophysical problems, such as the flux and indeed the origin of cosmic rays.

When gamma radiation enters the Earth's atmosphere, it is either absorbed (typical interaction length = 40 gm cm^{-2}) or lost in a sea of terrestrial gamma-rays generated by cosmic ray interactions in the atmosphere. Hence gamma-ray measurements are not, in general, feasible from the ground; experiments must be performed on high altitude balloons and satellites. Another problem which became apparent after several unsuccessful attempts to detect gamma rays was their intrinsically low intensity which is, for example, only 1/1000th of the primary cosmic ray flux. This meant that experimenters had to develop larger and more sophisticated detector systems.

The first certain detection of gamma-rays was made by Kraushaar et al (1972), with the pioneering experiment on board the OSO-3 satellite. Since then, two second generation gamma-ray detectors flown on the SAS-2 and COS-B satellites have obtained a more detailed picture of the gamma-ray sky. The most obvious feature of the sky when viewed in gamma rays is the emission from the Galactic plane, which is particularly intense within ± 40° in longitude of the Galactic centre. In this region, the gamma radiation is about an order of magnitude more intense than in directions away from the Galactic centre.

This high energy emission was interpreted by most authors as resulting primarily from diffuse processes in interstellar space-cosmic ray nuclei interacting with interstellar matter, principally atomic and molecular hydrogen. However the longitudinal distribution of gamma rays is not consistent with a uniform cosmic-ray intensity, using current estimates of the atomic and molecular hydrogen distributions, and this has led various theorists to assume that cosmic rays are galactic and to

propose, for example, that the cosmic ray flux increases in regions of higher gas density. But these assumptions may be premature in the light of the COS-B results. COS-B has detected 25 compact sources at energies above 100 MeV, of which two have been identified with the Crab and Vela radio pulsars. With more new sources predicted when forthcoming data is analysed, these results suggest an important contribution from compact sources to the total Galactic gamma emission. In this context, the possible contribution from radio pulsars is discussed later in the thesis.

1.2 Gamma-Ray Production

The various processes for producing cosmic gamma-radiation have been discussed by many authors, for example, Ginzburg and Syrovatskii (1965), Fazio (1967), Stecker (1971, 1975). This chapter will review those processes, as well as the important processes for the absorption of gamma-radiation.

A gamma-ray production mechanism may be expressed in terms of its source strength $S(E_\gamma,\underline{r})$ which is defined as the number of photons produced at the source, per unit volume, per unit time, per unit solid angle with energy between E_γ and $E_\gamma + dE_\gamma$ $(cm^3\ sec.sr.GeV)^{-1}$, where $\underline{r}$ is the vector from the detector to the source element.

Most of the gamma-radiation production mechanisms involve the reaction between an incident particle (or photon) of total energy E_i and a target particle (or photon). In this case, the function S can be expressed as :

$$S(E_\gamma,\underline{r}) = q(E_\gamma,\underline{r})\ n(\underline{r}) \quad (cm^3\ sec.sr.GeV)^{-1}$$

where $n(\underline{r})$ is the density of target particles and $q(E_\gamma,\underline{r})$ is the rate of production of gamma rays per target particle :

$$q(E_\gamma,\underline{r})dE_\gamma = dE_\gamma \int_{E_i} I_i(E_i,\underline{r})\ \sigma(E_\gamma,E_i)dE_i \quad (sec.sr)^{-1}$$

Here $I_i(E_i,\underline{r})dE_i$ is the differential intensity of incident particles in the energy range E_i and $E_i + dE_i$ in units of $(cm^2\ sec.sr.GeV)^{-1}$ and $\sigma(E_\gamma,E_i)$ is the cross-section for production of a gamma-ray in the range E_γ to $E_\gamma + dE_\gamma$ by an incident particle of energy E_i.

The gamma-ray intensity $I_\gamma(E_\gamma)$ is given by :

$$I_\gamma(E_\gamma) = \int_o^L S(E_\gamma,\underline{r})\ dr$$
$$= \int_o^L n(\underline{r})dr \int_{E_i} I_i(E_i,\underline{r})\sigma(E_\gamma,E_i)\ dE_i$$
$$= N(L) \int_{E_i} \sigma(E_\gamma,E_i) I_i(E_i,\underline{r})\ dE_i, \qquad (cm^2\ sec\ sr\ GeV)^{-1}$$

where $N(L) = \int_o^L n(\underline{r})dr$ is the number of gaseous atoms per unit area along the line of sight.

The intensity given above is usually referred to as the differential gamma-ray spectrum. The integral spectrum is defined by

$$I_\gamma(>E_\gamma) = \int_{E_\gamma}^{\infty} I_\gamma(E_\gamma)\ dE_\gamma$$

1.2.1 Gamma Rays from π°-Meson Decay

Cosmic rays traversing interstellar and intergalactic space will collide with the ambient nuclei. Most of these collisions will be proton-proton (p-p) interactions as protons comprise 90% of cosmic rays and hydrogen nuclei about 90% of the cool interstellar gas.

Various secondary particles of short lifetime are produced by the collisions. The most important of these secondaries for the production of gamma-radiation is the π°-meson which decays almost 100% of the time into two gamma-rays. The threshold kinetic energy T_{min} which a cosmic-ray proton must have to produce a secondary particle of mass m is :

$$T_{min} = (2 + \frac{m}{2M_p})m,$$

where M_p is the mass of a proton. Thus to produce a single π° meson of rest mass 135 MeV/c^2 requires a threshold kinetic energy of 280 MeV/c^2.

When a π° meson decays, because of conservation of momentum, the two gamma-rays are produced with an energy of 67.5 MeV (half the pion rest mass energy) in the rest frame of the pion. However, in the

terrestrial observer's frame these gamma-rays have unequal energies which are given by the relativistic Lorentz transformation :

$$E_{\gamma 1,2} = \upsilon \gamma_\pi (1 \pm \beta_\pi \cos \theta),$$

where γ_π and β_π refer to the energy and velocity of the π° meson in the observer's frame, υ is defined to be $m_\pi c^2/2$ and θ is the angle between the gamma-ray and the axis of transformation in the pion rest system. The $\pm$ sign applies because the γ-rays come off at opposite directions in the pion rest system.

Thus the spread in gamma energy is from $\upsilon \gamma_\pi (1 - \beta_\pi)$ to $\upsilon \gamma_\pi (1 + \beta_\pi)$. It can be seen intuitively that the distribution will be symmetric about 67.5 MeV on a log-log plot.

The rate of production of gamma rays per target proton is given by :

$$q(E_\gamma, \underline{r}) dE_\gamma = dE_\gamma \int_{E_{th}}^{\infty} I_p(E_p, \underline{r}) \, \varepsilon(E_p) \, dE \int_{E_{\pi_{min}}}^{\infty} \sigma(E_\pi, E_p) \times f_\gamma(E_\gamma, E_\pi) \, dE_\pi$$

where $I_p(E_p, \underline{r})$ is the proton differential spectrum, $\sigma(E_\pi, E_p)dE$ is the cross-section for the production of a π° meson with energy E_π in the interval dE_π, $\varepsilon(E_p)$ is the multiplicity of pion production, $f_\gamma(E_\gamma, E_\pi)$ is the gamma-ray energy distribution function from the decay of pions of energy E_π which is given by (Stecker, 1971) :

$$f_\gamma(E_\gamma, E_\pi) = \begin{cases} (E_\pi^2 - m_\pi^2 c^4)^{-\frac{1}{2}} & \text{for } \upsilon \gamma_\pi (1-\beta_\pi) < E_\gamma < \upsilon \gamma_\pi (1+\beta_\pi) \\ 0 & \text{otherwise} \end{cases}$$

Stecker (1975) has calculated the gamma-ray source function, including the contributions from p-α, α-p, α-α interactions as well as p-p interactions. The resulting gamma-ray energy spectrum is shown in Figure 1.1.

Stecker (1971) has also examined the asymptotic form of the gamma-ray spectrum to be expected from the decay of π° mesons produced at energies above a few GeV by cosmic-rays having a power-law spectrum of the form $E_p^{-\Gamma}$. Fazio (1967) showed that at these energies the pion production cross-section was constant ($\sim$ 27 millibarns). Assuming that the pion multiplicity rises as a power of the primary energy $\propto E_p^{a}$ and also that the average pion energy rises as E_p^{b}, then the production rate can be written in the form

$$q(E_\gamma,\underline{r}) = 8\pi\, n\, K_p\, \sigma_o \int_{E_{th}}^{\infty} dE_p E_p^{a-\Gamma} \int_{E_\gamma}^{\infty} dE_\pi\, \delta\left(\frac{E_\pi - X_o E_p^{b}}{E_\pi}\right)$$

where the coefficients σ_o and X_o and the exponents a and b are constants. Thus

$$q(E_\gamma,\underline{r}) = 8\pi\, n\, K_p\, \sigma_o \int_{(E_\gamma/X_o)^{1/b}}^{\infty} dE_p\, \frac{E_p^{-[(\Gamma+b)-a]}}{X_o}$$

$$= \frac{8\pi n}{g} K_p\, \sigma_o\, X_o^{[(g/b)-1]}\, E_\gamma^{-g/b}$$

where $g = [(\Gamma+b)-(a+1)]$.

Thus the high energy gamma-ray spectrum is also a power law but one which is different and in general steeper than the primary spectrum i.e. $g/b > \Gamma$. However, the primary cosmic-ray and gamma-ray spectra have the same index in the important case where a large and constant fraction of

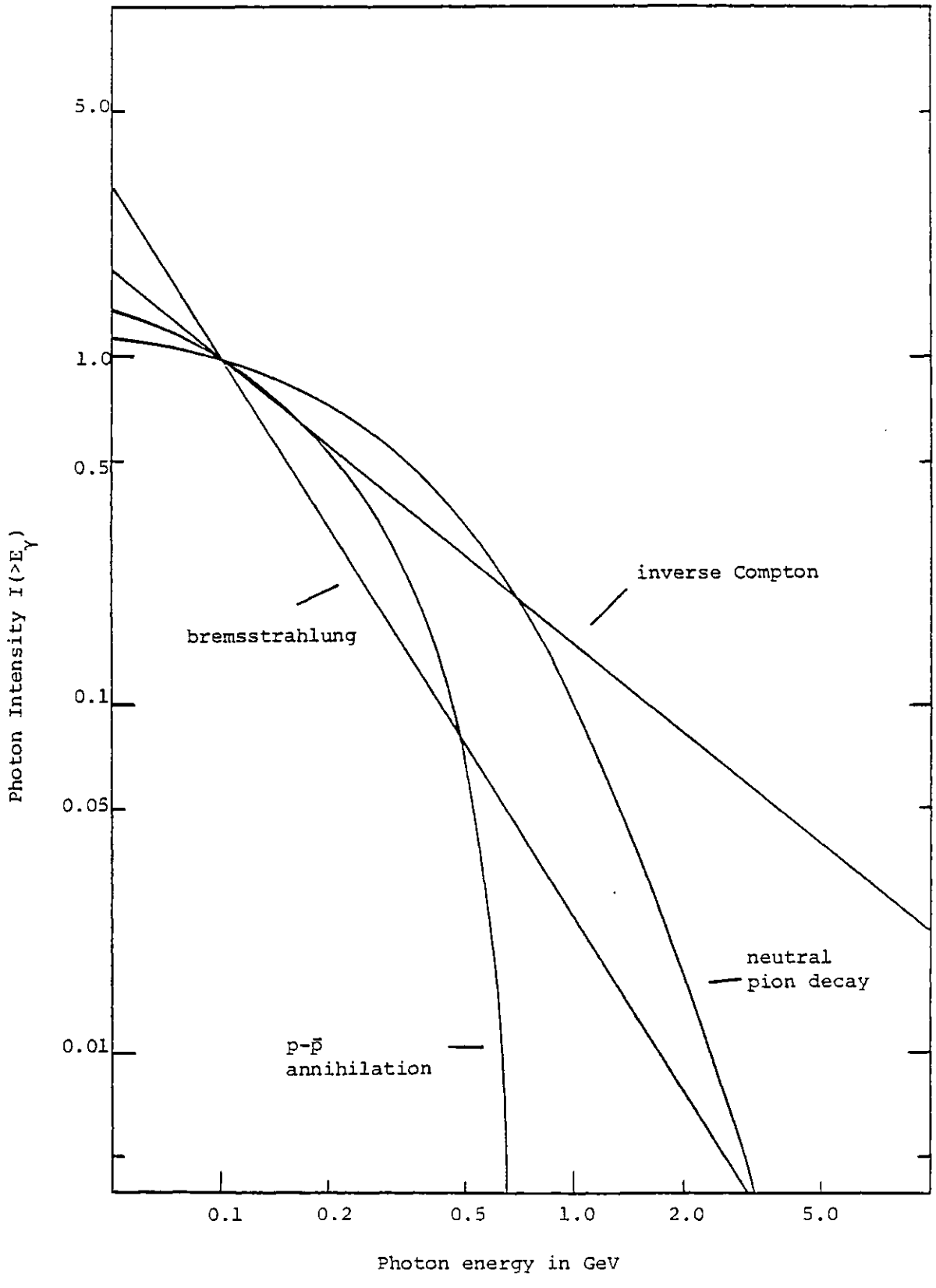

Figure 1.1 Gamma-ray spectra from inverse Compton, bremsstrahlung, neutral pion decay and p-$\bar{p}$ annihilation production mechanisms. All the curves are normalised to 1 at 100 MeV for comparison.

the primary energy of the cosmic ray is carried off by a single π° meson. In this case a = 0, b ≈ 1 and therefore g/b = Γ.

1.2.1.1 Matter-Antimatter Annihilation

Pion-decay gamma-rays may result from the annihilation of protons and antiprotons, according to the reaction :

$$p + \bar{p} \rightarrow a(\pi^+ + \pi^-) + b\pi^\circ \quad (\pi^\circ \rightarrow 2\gamma)$$

Again, one would expect the resultant gamma-ray production spectrum to be symmetric about 67.5 MeV on a logarithmic plot but, in this case, assuming the annihilations occur near rest in the universe, the spectrum will be bounded by the limited rest-mass energy which can be released in the annihilation.

Frye and Smith (1966), using accelerator data, and independently Stecker (1971), using a theoretical model of rest gas interacting with rest gas (since the annihilation cross-section is greatest at low cms velocities) have calculated the gamma-ray spectrum from p-$\bar{p}$ annihilations. There is good agreement between the two calculations and the resultant differential spectrum is shown in Figure 1.2.

1.2.1.2 Photo-pion Production

A process which may be important in producing gamma-rays of energies in the 10^{17} eV range is that of photomeson production. This involves the collision between an ultra-high energy cosmic ray and a starlight or microwave photon i.e.

$$\gamma + p \rightarrow \pi^\circ + p \quad (\pi^\circ \rightarrow 2\gamma)$$

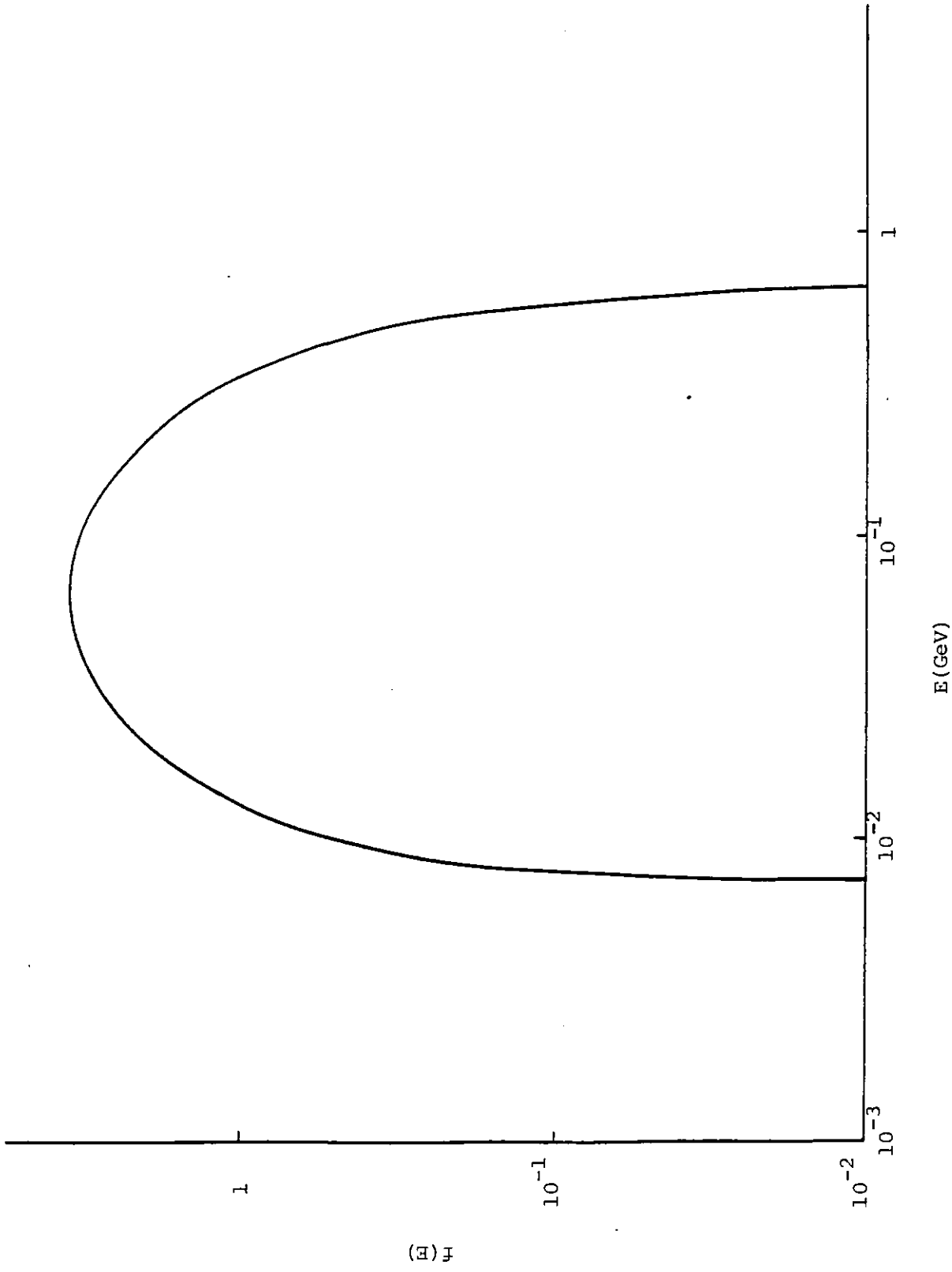

Figure 1.2 Normalised local differential γ-ray spectrum from p-$\bar{p}$ annihilation at rest (Stecker, 1971).

In order to produce a π° meson (rest mass energy = 135 MeV) the energy of the cosmic ray must exceed 10^{17} eV for collision with a starlight photon (typically 1 eV) or 10^{20} eV with a microwave photon (average energy $\sim 6 \times 10^{-4}$ eV). A typical gamma-ray produced by the above reaction carries off about 10% of the primary energy of the cosmic ray (Stecker, 1973).

1.2.2 Gamma-Rays from Electromagnetic Interactions

1.2.2.1 Bremsstrahlung

Bremsstrahlung is the radiation emitted by a charged particle in the field of a target nucleus. The probability of a charged particle emitting radiation is inversely proportional to the square of the mass of the incident particle, thus bremsstrahlung due to relativistic protons may be neglected in comparison with that due to relativistic electrons, even though electrons constitute only 1% of the cosmic radiation.

The cross-section for bremsstrahlung by relativistic electrons of energy E may be written in the form (Stecker, 1975)

$$\sigma_b(E,E_\gamma) = \frac{<M>}{<X>} \left[\frac{E}{E_\gamma}\right],$$

where E_γ is the energy of the gamma-ray, <M> is the average mass of the target atoms in grams and <X> is the radiation length for the gas in grams per cm^2 ($X = 65$ gm cm^{-2} for interstellar gas).

To a good approximation (Heitler, 1954), the normalised distribution of gamma-rays may be taken to be a square distribution :

$$f(E_\gamma/E) = \begin{cases} E^{-1} & \text{for } 0 \leq E_\gamma \leq E \\ 0 & \text{otherwise} \end{cases}$$

Thus the rate of production of gamma-rays per target nucleus is given by :

$$q(E_\gamma,\underline{r})\ dE_\gamma = \frac{<M>}{<X>}\ [\ \int_{E_\gamma}^{\infty} dE\ I_e(E,\underline{r})\ ]\ E_\gamma^{-1}$$

where $I_e(E,\underline{r})$ is the relativistic electron spectrum.

The intensity of gamma-rays due to bremsstrahlung is therefore given by

$$I_\gamma(E_\gamma) = \int_o^L n(\underline{r})dr.\frac{<M>}{<X>}\int_{E_\gamma}^{\infty} dE\ I_e(E,\underline{r})\ E_\gamma^{-1}$$

$$= N(L)\ \frac{<M>}{<X>E_\gamma}\int_{E_\gamma}^{\infty} I_e(E,\underline{r})\ dE$$

$$= \frac{M(L)}{<X>E_\gamma}\int_{E_\gamma}^{\infty} I_e(E,\underline{r})\ dE$$

Here M(L) is the mass of gas per unit area along the integration path.

If the electron spectrum is a power law i.e.

$$I_e(E_e,\underline{r}) = K_e\ E_e^{-\Gamma_e}$$

then $$I_\gamma(E_\gamma) = \frac{M(L)}{<X>}\ \frac{K_e}{(\Gamma_e-1)}\ E_\gamma^{-\Gamma_e}$$

and $$I_\gamma(>E_\gamma) = \frac{M(L)}{<X>}\ \frac{K_e}{(\Gamma_e-1)^2}\ E_\gamma^{-(\Gamma_e-1)}$$

Thus, for the observed value of $\Gamma_e = -2.6$, the differential gamma spectral index is -2.6 and the integral index is -1.6.

1.2.2.2 Inverse Compton Effect

In this process a relativistic electron collides with a low energy photon which, as a result, acquires sufficient energy to become an X-ray or a γ-ray. If the electron is a cosmic ray of energy $E = \gamma mc^2$ and

the photon has an initial energy ε, then on average the final photon energy (in the observer's frame) is

$$\varepsilon' = \frac{4}{3}\gamma^2 \varepsilon \qquad (\text{for } \gamma\varepsilon << mc^2) \qquad 1.1$$

For the astrophysical conditions of interest here, the condition $\gamma\varepsilon << mc^2$ holds and the cross-section for the scattering reduces to the non-relativistic Thomson cross-section :

$$\sigma_c \to \sigma_T = \frac{8\pi}{3}\left(\frac{e^2}{mc^2}\right)^2 = 6.65 \times 10^{-25}\ \text{cm}^2 \quad \text{(Heitler, 1954)}$$

Assuming the electron spectrum is again a power law i.e.

$$I_e(E) = KE^{-\Gamma}$$

then the gamma-ray production rate is given by

$$q(E_\gamma) = 4\pi n_{ph}\, \sigma_T \int dE\, KE^{-\Gamma}\, \delta(E_\gamma - \frac{4}{3}\langle\varepsilon\rangle\gamma^2)$$

$$= \frac{8\pi}{3}\sigma_T\, \rho_{ph}\, (mc^2)^{1-\Gamma}\, [\frac{4}{3}\langle\varepsilon\rangle]^{\frac{\Gamma-3}{2}}\, KE_\gamma^{-(\frac{\Gamma+1}{2})}$$

where n_{ph} is the number density of target photons of low energy in interstellar or intergalactic space (usually in the form of starlight photons or universal microwave photons) and $\rho_{ph} = n_{ph}\langle\varepsilon\rangle$ is the energy density of the radiation.

It follows that :

$$I_\gamma(E_\gamma) \propto E_\gamma^{-(\frac{\Gamma+1}{2})}$$

and $$I_\gamma(>E_\gamma) \propto E_\gamma^{-(\frac{\Gamma-1}{2})}$$

Thus, given the same electron spectrum, the inverse Compton spectral index is one-half that for bremsstrahlung.

1.2.2.3 Synchrotron Radiation

Synchrotron radiation or magnetic bremsstrahlung is the radiation emitted by a relativistic, charged particle spiralling in a magnetic field. Schwinger (1949) gives the rate of energy loss by synchrotron radiation for an electron of energy γmc^2 as

$$\left(\frac{dE}{dt}\right)_{syn} = -\frac{4}{3}\sigma_T c \gamma^2 \rho_H$$

where ρ_H $(= H^2/8\pi)$ is the magnetic energy density. This rate should be compared with the corresponding rate for Compton interactions :

$$\left(\frac{dE}{dt}\right)_{c} = -\frac{4}{3}\sigma_T c \gamma^2 \rho_{ph}$$

where $\sigma_T c \rho_{ph}/\langle\varepsilon\rangle$ is the collision rate between the electron and the photon field and $4/3\ \gamma^2\langle\varepsilon\rangle$ is the energy lost per collision.

The photons emitted as synchrotron radiation have a characteristic frequency given by

$$\omega_{syn} = \frac{3}{2}\gamma^2\left(\frac{eH_\perp}{mc}\right)$$

and a characteristic energy :

$$E_{\gamma,syn} = \frac{3}{2}\gamma^2\left(\frac{\hbar}{mc}\right) eH_\perp \qquad 1.2$$

Because this is the same type of energy dependence as that for Compton radiation, a power-law cosmic ray electron spectrum will generate a synchrotron spectrum of the same form as the Compton spectrum i.e.

$$I_\gamma(>E_\gamma) \propto E_\gamma^{-(\frac{\Gamma-1}{2})}$$

The above equations can be used to determine the relative importance of synchrotron radiation and Compton scattering in producing gamma-radiation in the Galaxy. If one specifies that an electron of energy $\gamma_c mc^2$ will radiate a Compton photon at the same mean energy as an electron of energy $\gamma_s mc^2$ will radiate a synchrotron photon, then it follows from equations 1.1 and 1.2 that the ratio

$$\frac{\gamma_s}{\gamma_c} \approx 10^7 \left(\frac{<\varepsilon>}{H_\perp}\right)^{\frac{1}{2}}$$

The relative production rates from synchrotron and Compton radiation are then related by

$$\frac{Q_s}{Q_c} = \frac{\rho_H}{\rho_{ph}} \frac{I_e(\gamma_s)}{I_e(\gamma_c)}$$

In the Galaxy, $\rho_{ph} \approx \rho_H$, but $\gamma_s >> \gamma_c$ so that $I_e(\gamma_s) << I_e(\gamma_c)$ and synchrotron radiation is negligible compared to Compton scattering as a gamma-ray production mechanism.

1.3 Gamma-Ray Absorption

Gamma-rays produced in the Galaxy and in the Universe are depleted by various processes of astrophysical importance. These processes fall into two basic categories :

1. absorption through interactions with radiation
2. absorption in matter.

The former is of greater importance because of the existence of the 2.7 K universal radiation field.

1.3.1 Absorption through Interactions with Radiation

The attenuation process of importance here is the pair production process :

$$\gamma + \gamma_{rad} \rightarrow e^+ + e^-$$

where γ_{rad} may be in the form of universal microwave photons, starlight photons or radio photons. This process can only take place if the total energy of the photons in the centre of mass system of the interaction is greater than or equal to $2m_e c^2$. The threshold energy for the reaction can be obtained by noting that the relativistic four-momentum invariance condition reduces to

$$(2E_e^*)^2 = 2E_\gamma E_{rad} (1 - \cos\theta)$$

where E_e^* is the energy of the electron (positron) in the c.m.s. At threshold, both the electron and the positron are produced at rest in the c.m.s. of the interaction. The minimum energy required corresponds to a head-on collision ($\cos\theta = -1$) and is therefore given by

$$E_{\gamma,th} = \frac{(m_e c^2)^2}{E_{rad}} = \frac{(0.51 \times 10^6)^2}{E_{rad}} \text{ eV}$$

Gould and Schreder (1967a,b) have calculated the absorption probability for gamma-rays interacting with various photon fields and their results are shown in Figure 1.3. The curve representing the microwave absorption has been corrected by Stecker (1971) since, at the time Gould and Schreder published their results, the temperature of the universal radiation field was thought to be 3K instead of the presently accepted value of 2.7 K.

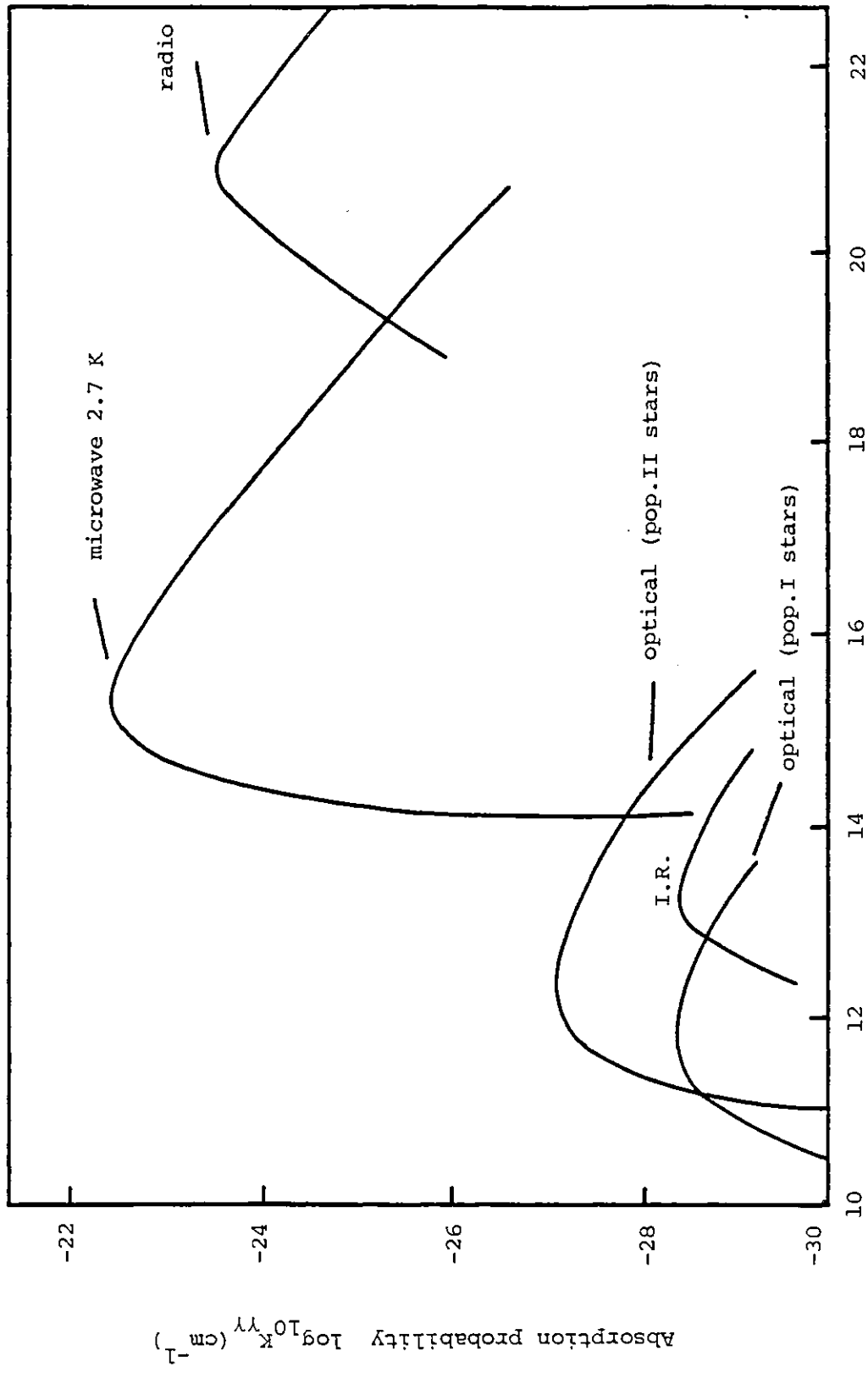

Figure 1.3 Absorption probability per unit distance by the $\gamma+\gamma\rightarrow e^+e^-$ process as a function of photon energy for gamma-rays passing through various universal radiation fields.

1.3.2 Absorption in Matter

The interactions of importance here are Compton scattering of the gamma-ray on an electron resulting in a transfer of energy to the electron and pair production which occurs when a gamma-ray passes through the electrostatic field of a charged particle or nucleus.

The significance, or otherwise, of these processes in absorbing gamma-rays is best illustrated in terms of an absorption length K, which is defined according to

$$I = I_o \, e^{-L/K}$$

where I_o and I are the initial and final gamma-ray intensities and L is the effective path length in the medium. For Compton scattering, $K \gtrsim 1.5 \times 10^{23}$ cm for the Galaxy, which is 5 Galactic radii, and $K \gtrsim 1.5 \times 10^{29}$ cm for the metagalaxy which is 30 times the photometric radius of the Universe. Thus absorption due to Compton scattering can be neglected. For pair production, $K \gtrsim 3 \times 10^{23}$ cm for the Galaxy and $K \gtrsim 3 \times 10^{28}$ cm for the metagalaxy. Thus absorption is again negligible. The cross-sections for these two processes are shown in Figure 1.4, which is taken from Stecker (1971).

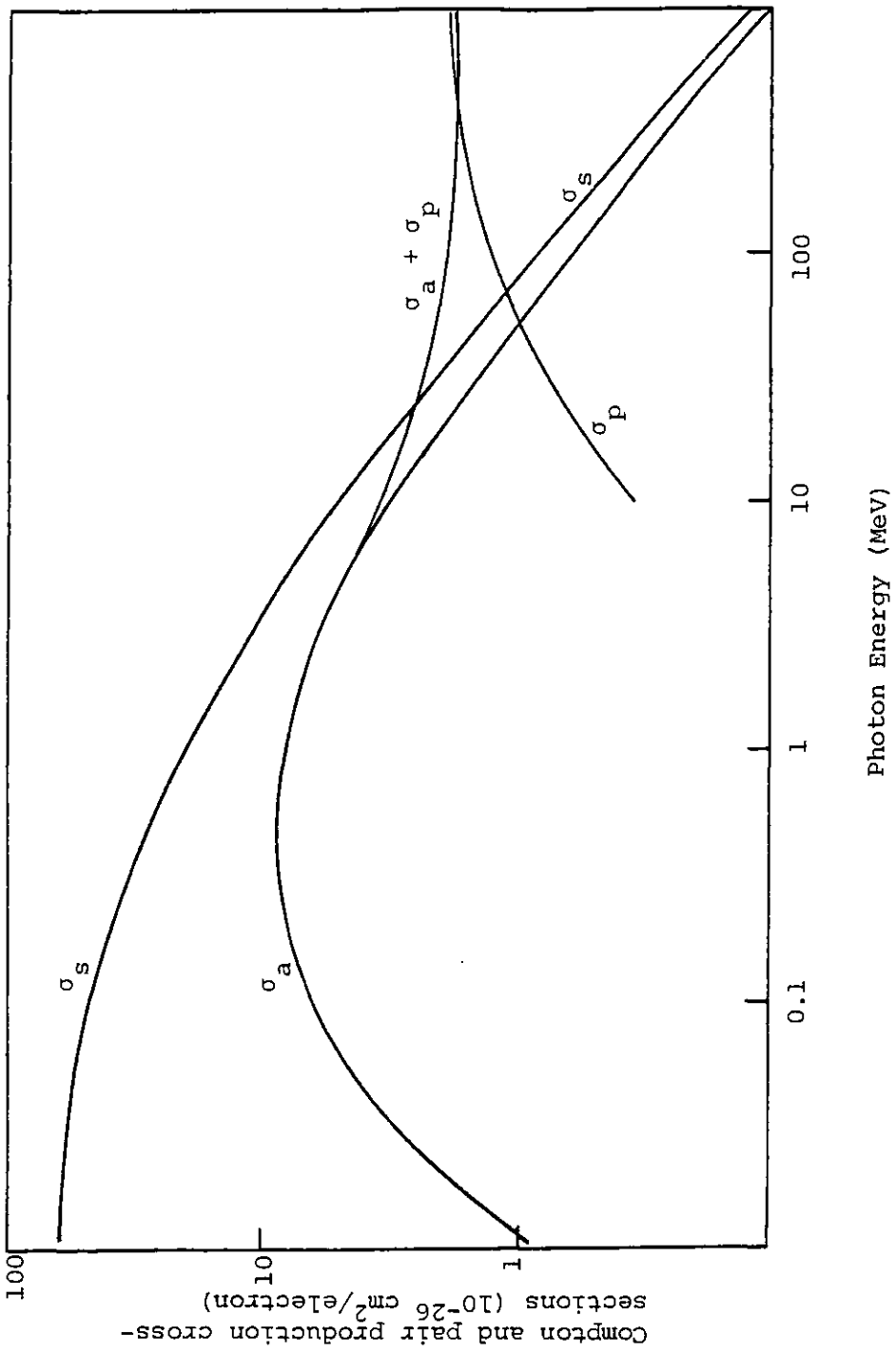

Figure 1.4 Compton scattering (σ_s), Compton absorption (σ_a), pair production (σ_p) and total ($\sigma_a + \sigma_p$) cross-sections as a function of gamma-ray energy for absorption of gamma-rays in hydrogen gas.

CHAPTER II

THE IC GAMMA-RAY DETECTOR

2.1 Introduction

Since 1973, a series of balloon flights has been carried out over Australia with telescopes sensitive to gamma-rays in the energy range $0.2<E<5.0$ GeV (see Table 2.1). The objective was to determine the energy spectrum of the gamma-radiation in the Galactic Centre region ($330<\ell^{II}<30°$, $-10°<b^{II}<10°$) which, in 1973, had not been measured. It was thought that the spectrum would provide information on the gamma-ray emission processes. In the meantime, though, the SAS-2 and COS-B satellites have flown successfully and COS-B in particular has published spectra from different regions of the Galactic plane. However the results from our flights still provide independent confirmation of the energy spectrum in the form of upper limits.

This thesis contains a re-analysis of the 1973 flight previously performed by Clayton (1975) but is concerned principally with results from the two balloon flights in 1975. Two more flights were carried out in 1977 and 1978 using a modified version of the detector, but a detailed account of these flights will be published later. For the flights two essentially identical units were used. The first was flown in 1973, 1975 (and 1977) and the second in 1975 (and 1978).

TABLE 2.1 Balloon Flights over Australia

Site	Date of Launch	Duration (hrs)	Float Depth (mb)
Longreach, Queensland Lat : -23.15°; Long : 144.18°	18 Nov. 1973	12	4.0
Alice Springs, Northern Territory Lat : -23.73°; Long : 133.83°	7 Nov. 1975	11	3.8
	21 Nov. 1975	60	2.8
	16 Nov. 1977	30	2.8
	13 Nov. 1978	58	2.8

2.2 The Gamma-Ray Detector

2.2.1 Design Requirements

The problems associated with the detection of extra-terrestrial gamma-rays from balloons have been outlined previously, namely the low photon fluxes and the high atmospheric background. Thus, in designing the instrument, the principal requirements were considered to be :

a) unambiguous identification of gamma-rays in the presence of background noise

b) efficient rejection of charged particle and noise events

c) useful detection efficiency for gamma-rays down to 200 MeV

d) a large, sensitive detector area and opening angle

e) high angular resolution to distinguish between a truly diffuse emission and a cluster of point sources

f) good energy resolution to discriminate between power law and π° decay spectra, say

g) robust construction to withstand the extremes of pressure and temperature experienced during flight

h) light weight to achieve maximum altitude.

2.2.2 Description of Operation

The Imperial College gamma-ray detector is shown schematically in Fig.2.1. A detailed description of the instrument has appeared elsewhere (Clayton, 1975) so only a brief account is given here. The detector was cylindrically symmetric about its axis. An anticoincidence scintillator A was used to veto charged particle events. Incident gamma-rays passed through the shield and were converted into electron pairs in half a radiation length of lead. If one or more electrons triggered the coincidence telescope, which consisted of scintillators B and C and the lead glass element D, a high voltage pulse was applied to each gap of the spark chamber, and sparks formed along the ionised tracks left by the electrons. From the electron tracks the arrival direction of the gamma-ray could be deduced. The energy of the photon was determined from an analysis of the Cerenkov light emitted by an electromagnetic cascade generated by the electron pair in the lead glass counter D.

2.3 The Coincidence Telescope

2.3.1 Scintillator Elements

The two scintillators B and C were discs of plastic scintillator NE102A of 38 cm diameter and $\frac{1}{4}$", $\frac{1}{2}$" thickness respectively. The scintillators were each viewed with a single 2" photomultiplier tube

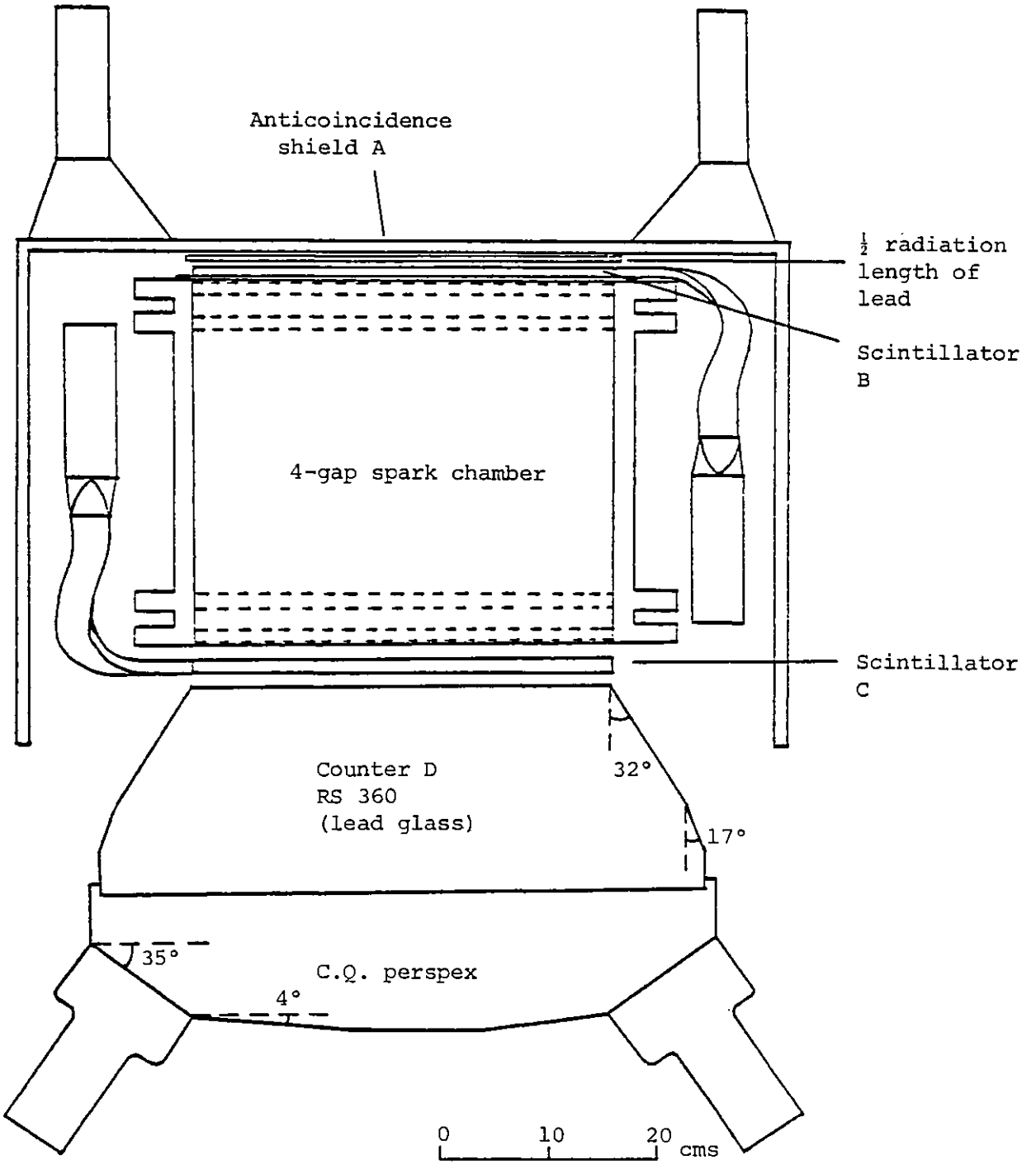

Figure 2.1 The Detector

through a perspex light pipe. The light pipes consisted of sections of polished CQ perspex and were shaped to match the edge of the scintillator to the window of the photo-tube. All elements were sealed in aluminium foil and black adhesive tape to exclude ambient light.

The output from the PM tube viewing the ½" scintillator C was fed through a charge amplifier to a pulse height analyser. The pulse was delayed for 250 nanoseconds in order to check the coincidence logic. If the gamma-ray signature was seen ($\bar{A}BCD$), the pulse was applied to a ringing circuit. Oscillations were induced in the circuit, the actual number being proportional to the amplitude of the pulse. Those oscillations above a discriminator threshold were counted and the number stored in a 9-bit binary store. The pulse height output was used to determine the number of electrons traversing the scintillator.

2.3.2 The Lead Glass Calorimeter

The third element of the coincidence telescope was a 7-radiation length deep (24.5 cm) block of lead glass used as an energy calorimeter. The energy measurement of the electrons and hence the gamma photon was determined by analysing the Cerenkov light emitted by an electromagnetic shower generated by the electrons. Cerenkov light is produced whenever a charged particle passes through a medium with a velocity v greater than the velocity of light in that medium (c/n). The light is radiated in a cone of half opening angle θ, such that

$$\cos\theta = 1/\beta n$$

where $\beta = v/c$ and n is the refractive index of the medium. The threshold velocity for Cerenkov emission is $v = c/n$ when $\theta = 0°$. θ then increases with velocity v until a maximum value of $\theta = \cos^{-1}(1/n) \approx 52°$ is

obtained as $v \rightarrow c$.

Cerenkov radiation peaks towards the blue in the visible spectrum, thus a Cerenkov detector should have high transmission down to 400 nm. Various glasses were tested in the 5 GeV electron beam at Daresbury (Sood et al, 1974). As a result of these tests, Schott RS360 lead glass was chosen. This is a radiation-shielding glass of refractive index 1.62 and density 3.6 gm cm^{-3}.

The shape of the lead glass and the CQ perspex light pipe was chosen to maximise the light collection efficiency. Factors affecting the efficiency included :

i) the large half opening angle of the Cerenkov cone, typically 38°

ii) the reflectivity of the walls of the lead glass and light pipe

iii) the arrangement of the phototubes viewing the lead glass.

The surfaces of the lead glass were polished and covered with aluminium foil and black tape. The top surface of the lead glass was blackened to absorb light from upward moving showers (produced by cosmic ray interactions in the lead glass) which could trigger the telescope. The light pipe was aluminium coated and covered with black tape.

The lead glass and light guide were viewed by six 5" diameter photomultiplier tubes. The gains of the PM tubes were equalised, the outputs were summed and pulse-height analysed (cf with the $\frac{1}{2}$" scintillator) to yield information on the energy of the gamma-ray.

A light-diode was attached to the top of the lead glass to provide on-board calibration of the pulse height channel. The diode was triggered by a solar sensor event (section 2.7.5). By comparing the pulse height output in flight with that obtained on a calibration

run, the behaviour of the detector could be monitored during flight.

The discrimination threshold of the pulse height analyser was set to 200 MeV so that photons below this energy were rejected.

2.3.3 The Anticoincidence Shield

The anticoincidence shield A, which surrounded the spark chamber and scintillators, was used to reject cosmic ray events. It consisted of sections of plastic scintillator type NE102A : a top scintillator viewed directly by two 2" photomultiplier tubes and a cylinder of four sections, each viewed through a perspex light guide by a single 1" phototube. All sections were covered with aluminium foil and black insulation tape.

The efficiency of the shield in removing charged particle events (signature ABCD) from the gamma-ray channel was measured using ground-level cosmic rays (mostly mu-mesons) and was found to exceed 97%.

2.4 The Lead Converter

The gamma photons were converted into electron-positron pairs in a sheet of lead of 38 cm diameter and half a radiation length thickness. The probability of pair production in a medium is proportional to Z^2, where Z is the atomic number of the medium, thus lead (Z = 82) is an efficient and cheap conversion material. The choice of half a radiation length thickness was governed by two requirements : a high probability of pair production, which increases with thickness, and a minimal amount of Coulomb scattering of the electron pair. (Multiple Coulomb scattering was the dominant factor in the loss of angular resolution of the detector.)

2.5 The Spark Chamber

The spark chamber had a geometrical area of 40 x 40 cm^2 and consisted of four spark gaps, arranged in pairs. (The top and bottom pairs were 30 cm apart.) Each gap consisted of two planes of wires, stretched in orthogonal directions. The wire planes were separated by 1 cm. The wires, separated by 0.6 mm, were soldered to bus bars. One bus bar was connected to a high voltage supply and the other was grounded so that, when triggered, the current path was along one of the wires of the 'high' plane, across the ionised track left by the electrons and then to ground along one of the earthed wires. The spark chamber was filled with a mixture of helium and neon gases (31% He, 69% Ne) at atmospheric pressure.

The position of the spark in the gap was found using a magnetostrictive delay technique, originally suggested by Perez-Mendez and Pfab (1965). The magnetostrictive wires (MSW) lay in grooves parallel to the bus bars i.e. across the wire planes. The MSW were electrically insulated from the spark wires by a thin PTFE sleeving.

When a gap was fired, the magnetic field pulse of the spark current produced a local deformation of the magnetostrictive wire, at the point of intersection of the fired wire and the MSW. This deformation then travelled as a stress wave along the MSW. The pulse was sensed by pick-up coils situated at each end of the wire. (One coil in each pair could detect a second pulse.) (see Figure 2.2a,b).

By measuring the transit time of the magnetostrictive pulse, the position of the spark could be found. The timing was performed by gating on a 2.15 MHz crystal-controlled clock 4 μs after the spark chamber was triggered (to reduce spark interference) and gating it off when the pulse arrived. The number of clock pulses before the clock was gated off was counted and stored in twenty-four nine-bit binary stores

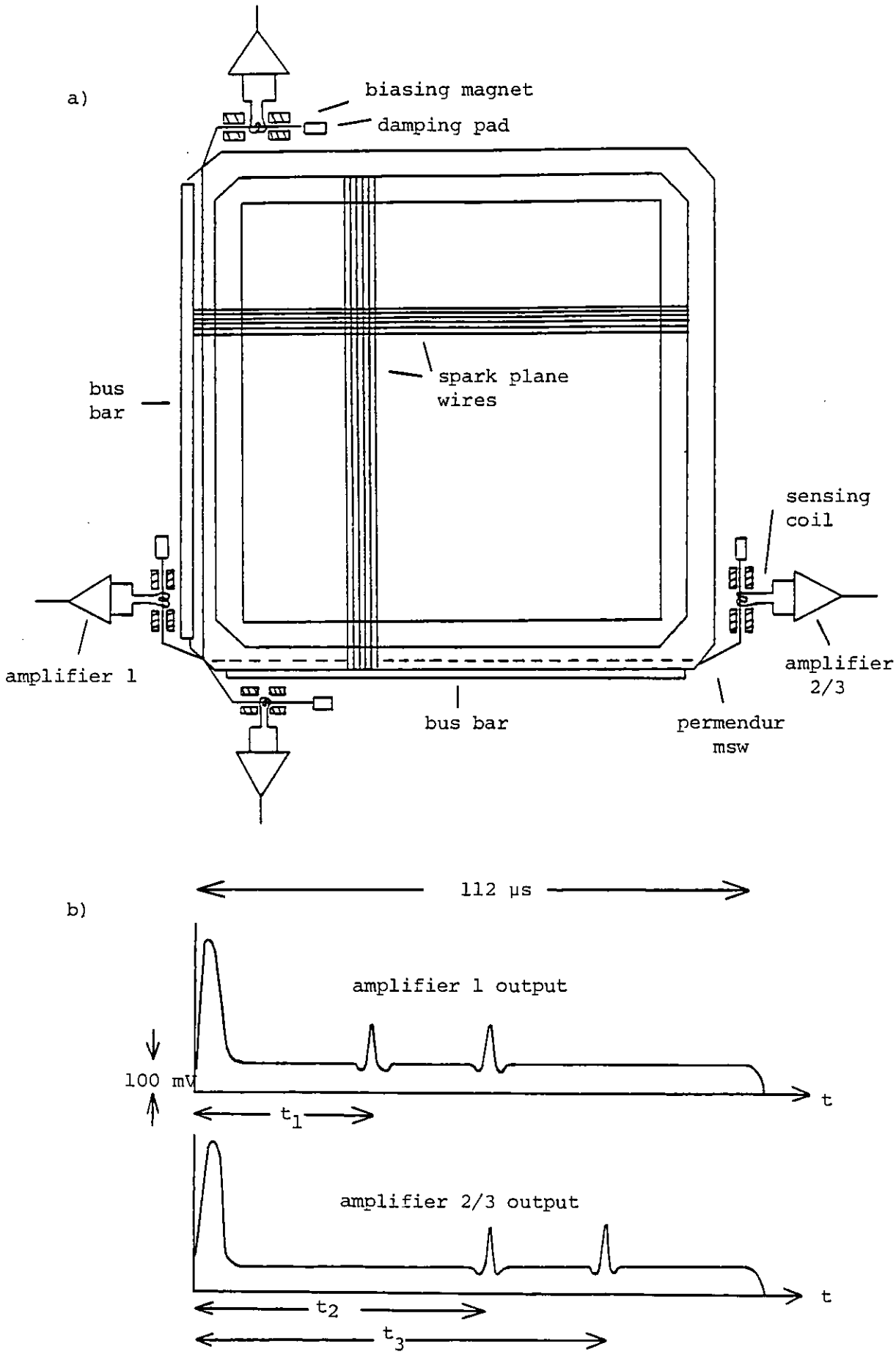

Figure 2.2 a) Schematic diagram of a spark plane.
b) Typical outputs from the complementary amplifiers.

i.e. 3 numbers (since one coil could detect a second spark pulse) for each of the eight MSW. The clock was automatically switched off after 192 clock pulses; this allowed sufficient time for a magnetostrictive pulse to travel to the pick-up coils. A 192 number would thus indicate that a particular gap had not fired or the amplitude of the magnetostrictive pulse was below a threshold level.

2.6 Cosmic Ray Counter

The detector was also capable of counting cosmic rays. Cosmic rays triggered the anticoincidence shield and were therefore identified by the signature ABCD. The number of cosmic ray events was counted using an eight-bit binary counter, which reset to zero when the number exceeded 255.

2.7 Payload Orientation and Tracking

In order to determine the arrival direction of the incident gamma-ray in the celestial or galactic coordinate system from the spark chamber directional information, it was necessary to know :

a) the latitude and longitude of the detector

b) the orientation of the detector (i.e. spark chamber axes) in terrestrial coordinates

c) the arrival time of the gamma-ray.

2.7.1 Tracking of the Payload

Transmitted data from the detector was received using a steerable twin Yagi aerial. An identical aerial was used as the direction finder. In this aerial, the output of one element was passed through a $\lambda/2$ delay line (i.e. a π phase change was introduced) and then combined with the second output, so that a null reading occurred when the aerial was

pointing directly at the detector. With the aerial in the null position, the bearing was measured with a magnetic compass to an accuracy of about one degree.

The line-of-sight distance was determined using an on-board transponder. This received a square wave modulated signal on the 108 MHz waveband which was returned on the data channel (136 MHz). The time delay between the transmitted and received signals (measured on an oscilloscope) was converted into a distance to give the range. The bearing and the line of sight range of the payload were also regularly monitored using the radar facility at the launching station. (Of course, this was only possible as long as the balloon was within radar range.)

2.7.2 Altitude Measurement

The altitude of the detector was measured with two 'Olland cycle' devices attached to the detector frame outside the pressure dome. Both measured atmospheric pressure to an accuracy of ± 0.2 mb at 3 mb depth. The devices also had a temperature measurement scale of +30° to -60°. The information from the two devices was transmitted continuously on two sub-carrier frequencies at 1.3 and 2.3 kHz.

Given the range, bearing and altitude data, the flight path of the detector in geographic coordinates could be determined.

2.7.3 The Magnetometer

The orientation of the detector with respect to magnetic north was measured using a three-axis fluxgate magnetometer, which was mounted on a one-metre boom to reduce the effects of stray fields produced by the detector. The output from each magnetometer element ranged from 0 volts in a field of -50,000γ (-0.5 gauss) to 5 volts in a field of +50,000γ and was digitised so that $10^5\gamma$ = 2000 digits. The magnetometer was

accurate to within 2 digits in 1000, or an angular error of ± 0.3°. The digital outputs from the three magnetometer axes were stored in three eleven-bit binary stores.

2.7.4 Event Timing

The data received from the payload was recorded at 30 ips on an Ampex tape recorder. Event times were obtained by simple interpolation along a magnetic tape record, given the starting and stopping times of each tape. This method was considered sufficiently accurate, because the experiment was not designed to look for fast time-varying phenomena.

2.7.5 Solar Sensors

Two solar sensors were used to check the orientation of the detector, as determined by the magnetometer. They were mounted independently on a boom of length 0.5 m. Each sensor consisted of two semi-circular aluminium sections (of 4 cm diameter and 1.5 cm thickness) separated by 1 mm. The slit was viewed directly by a phototransistor. As the payload rotated, the sun passed across the slits and triggered the phototransistor. This, in turn, triggered the light diode on the lead glass, the magnetometer and the spark chamber, provided a gamma event was not being processed. A solar sensor event was easily identifiable from the spark numbers (all 192) and the lead glass pulse height number, typically $\sim$ 115. This number provided a check on the behaviour of the detector.

2.8 Electronics and Data Handling

2.8.1 Power Supplies

The power requirements of the detector were provided by packs

of Nickel Cadmium rechargeable batteries and in addition for the 60 hour 1975 II flight lead-acid car accumulators. The latter were used after the Nickel Cadmium packs had discharged (typical lifetime of 15 hours). The Nickel Cadmium and lead-acid batteries were arranged to provide supplies of 12 volts, 13 volts and 25 volts. The 12 volt pack supplied the photomultiplier tubes of the telescope through a high tension converter. The 13 volt pack supplied the spark chamber power requirements through two high tension converters. The 25 volt pack provided the low tension supplies for the electronics.

2.8.2 Data Formatting and Transmission

The gamma-ray event word contained 282 bits. Each word consisted of the following information :

Cosmic Rays	1 channel of 8 bits	8 bits
Magnetometer	3 channels each of 11 bits	33 bits
Spark Chamber	24 channels each of 9 bits	216 bits
Lead Glass D	1 channel of 9 bits	9 bits
½" Scintillator C	1 channel of 9 bits	9 bits
Solar Sensor	2 channels each of 1 bit	2 bits

The remaining 5 bits were parity bits, two at the beginning and three at the end of the event word. They should always be in the 'zero' state.

Data from the various channels was stored in binary stores until the whole word had been compiled. Then the stores were clocked out sequentially at a bit rate of 1.8 kHz into the data encoder. Here, the 'one' and 'zero' states were encoded into bursts of 30 and 15 pulses respectively of a 124 kHz oscillator. The train of bursts was then used to modulate a 136 MHz FM transmitter. The event word was read out in

166 milliseconds which was the instrumental dead time, during which the coincidence logic was suppressed.

Other data transmitted was the two Olland signals and the transponder. The 136 MHz transmitter fed a simple dipole aerial.

2.9 Environmental Stability

The payload was enclosed in an aluminium pressure dome of 1.5 mm thickness. This maintained the detector at ground-level atmospheric pressure and thereby removed undue stress on the spark chamber, which contained a He-Ne mixture at atmospheric pressure. The whole detector was enclosed in a box of expanded polystyrene to provide thermal insulation. The outside of the box was partially blackened to absorb heat from the sun.

The detector was tested in a refrigerated trailer to check the performance in conditions expected at altitude. No degradation of performance was seen down to -5°C (minimum temperature encountered in flight was +10°C).

2.10 Contamination of the Gamma Event Channel by Spurious Events

The telescope could be triggered by non-gamma events. Chance coincidences arising from thermal noise pulses in the photomultiplier tubes viewing elements B,C,D and neutron induced events in which a neutron passed undetected through the anticoincidence shield and produced a proton in the lead converter were shown to be negligible (Clayton, 1975). Cosmic ray leakage through the anticoincidence shield was observed (see section 5.1.3), however the major source of contamination was upward moving particles, produced mainly by cosmic ray interactions in the lead glass. These could imitate genuine gamma events if the upward-moving particles were absorbed in the lead converter or the spark chamber walls and did not trigger the anticoincidence shield.

2.11 Modifications to the 1977/78 Detector

a) In order to remove upward moving events, a time-of-flight (TOF) system was developed and added to the triggering telescope for the 1977 and 1978 flights. The TOF system consisted of two discs of plastic scintillator type NE104, each viewed by two photomultiplier tubes. The top disc was placed between the lead converter and scintillator B and the bottom disc between scintillator C and the lead glass. The method used to handle the pulses from the PM tubes is described in Sood et al (1982). When tested with mu-mesons in the laboratory, the TOF system was found to reject 90% of upward moving particles.

b) An added objective of the 1977 and 1978 flights was to study point sources, in particular the Vela pulsar. To point the telescope in a specific direction, an alt-azimuth orientation system was used. An additional magnetometer was used to monitor the pointing direction. If the magnetometer output differed from a reference voltage, a heavy inertia wheel situated below the detector was energised and returned the detector to the desired direction. The pointing direction could be altered by telecommand from the ground station.

c) The angle of tilt of the telescope was measured with a tilt sensor. The sensor consisted of a closed glass tube containing a bubble of gas in a conducting liquid and two electrodes. As the tube was tilted the position of the bubble relative to the electrodes altered. This change was detected electronically and used to produce an output voltage, which varied with the tilt angle.

d) In order to observe pulsed emission from the Vela pulsar, accurate event timing was essential. Thus a rubidium clock, accurate to 1 part in 10" sec, was included in the payload.

e) In the 1977/78 version of the telescope, scintillator B was also of $\frac{1}{2}$" thickness with a pulse height analyser to measure the light output.

CHAPTER III

DETECTOR CALIBRATION

3.1 Introduction

In the previous chapter, the description of the gamma-ray detector was preceded by a brief discussion of the design requirements of the detector. This chapter will show how well the two detectors satisfied those design requirements, by deriving various parameters. The calibration of the instruments was performed using the gamma-ray beam facility of the Deutsches Elektronen Synchrotron (DESY) in Hamburg. A description of the beam facility was published by Christ et al (1974). The relevant beam characteristics are given in the table below.

The responses of the two units were also cross-checked using data from ground-level mu-meson tests and actual flight data.

TABLE 3.1 Characteristics of the Tagged Photon Beam

Nominal Energy E_γ (MeV)	Fractional Energy Spread $\Delta E_\gamma/E$ (%, FWHM)	Tagging Efficiency (%)
200	15 ± 2	90 ± 1
300	19 ± 4	94 ± 1
500	10 ± 2	94 ± 1
1000	10 ± 2	92 ± 1
2000	7 ± 2	90 ± 2
4000	6 ± 1	86 ± 2
5000	5 ± 1	85 ± 2
6000	5 ± 1	90 ± 1

The tagging efficiency is defined as the fraction of beam triggers (beam triggers are signals from the beam electronics indicating the passage of a photon) corresponding to a photon arriving in the experiment area.

3.2 The Spark Chamber

3.2.1 Absolute Sparking Efficiency

The information from each plane of the spark chamber was contained in three numbers t_1, t_2, t_3 say. If a single spark only was detected by a plane, one would expect :

a) $t_3 = 192$

b) $t_1 + t_2 \not< t_{av}-4$, where t_{av} is the average time taken for a pulse to travel from one sensing coil to the other along the MSW

c) $t_1 + t_2$ not greater than a realistic upper limit set empirically for the plane.

However, if two sparks were detected by a plane, then

a) $t_3 \neq 192$

b) $t_1 + t_3 \not< t_{av}-4$

c) $t_1 + t_3$ not greater than the upper limit set for the plane.

If the above criteria were not satisfied, then the particular plane was flagged, but the information content was not totally rejected.

The main inefficiencies of the spark chamber were i) failure to detect the magnetostrictive pulses (signified by a 192 number

in the first or second channel) and ii) the production of meaningless numbers (typically, single digit) in t_1 and t_2 due to noise pulses. Of course, if the three numbers were all 192, then no information could be retrieved.

The gamma events were classified according to their spark patterns, as shown below :

TABLE 3.2

x denotes a satisfactory signal from the plane

(x or y) plane

	4	x	x	x	x	o	x	x	o	o	
z ↑	3	x	x	o	x	x	o	o	x	x	all
	2	x	o	x	x	x	o	x	o	x	others
	1	x	x	x	o	x	x	o	x	o	
	type	1	2	3	4	5	6	7	8	9	10

All type 10 events were automatically rejected. Events of type 6 - 9 with two sparks detected on one plane were also rejected. However, if two sparks were observed on two or more planes, then the event was labelled a double track.

On flights in which the four spark planes were approximately equally efficient, it was possible to calculate the absolute spark chamber efficiency ε by comparing the frequency of occurrence of events in which two, three and four planes had fired : if the efficiency of a plane in detecting a spark is η, then the probability of 4, 3 and 2 planes

firing is as follows :

4 planes firing $P_4 = \eta^4$

3 planes firing $P_3 = 4\eta^3 (1-\eta)$

2 planes firing $P_2 = 4\eta^2 (1-\eta)^2$

$$\therefore \quad \frac{P_3}{P_4} = \frac{4(1-\eta)}{\eta} \quad \text{and} \quad \frac{P_2}{P_4} = \frac{4(1-\eta)^2}{\eta^2}$$

Using these frequency ratios, a value for η and therefore $\varepsilon = \sum_i P_i = \eta^4-4\eta^3+4\eta^2$ could be obtained. It was also possible to cross-check these values with efficiency measurements made on the tagged gamma-ray beam at DESY and from the rate of events recorded by the spark chamber as a fraction of the total number of triggers.

Figure 3.1 shows ε as a function of local time (in minutes) for the 1973 and the two 1975 flights. The efficiency was less during flight II 1975 because of a faulty spark gap. The reduction in efficiency towards the end of the 1973 and 1975 I flights could be due to aging of the spark chamber gas or the batteries becoming flat.

The efficiency also varied with zenith angle θ and gamma energy. The dependence is illustrated in Figure 3.2, which shows ε as a function of θ for two different energy intervals. The efficiency was virtually constant for $\theta \lesssim 32°$, but fell steeply beyond this. The fall-off was due to the electric field along the length of ionised track (the length increases with zenith angle, of course) not being sufficient to cause breakdown of the gas.

ε increased with energy because, at higher energies, the opening angle of the electrons was smaller and therefore the density of ionisation was greater, making spark formation more likely.

Functions representing the dependence of ε on zenith angle, energy and time were included in the computer program that calculated

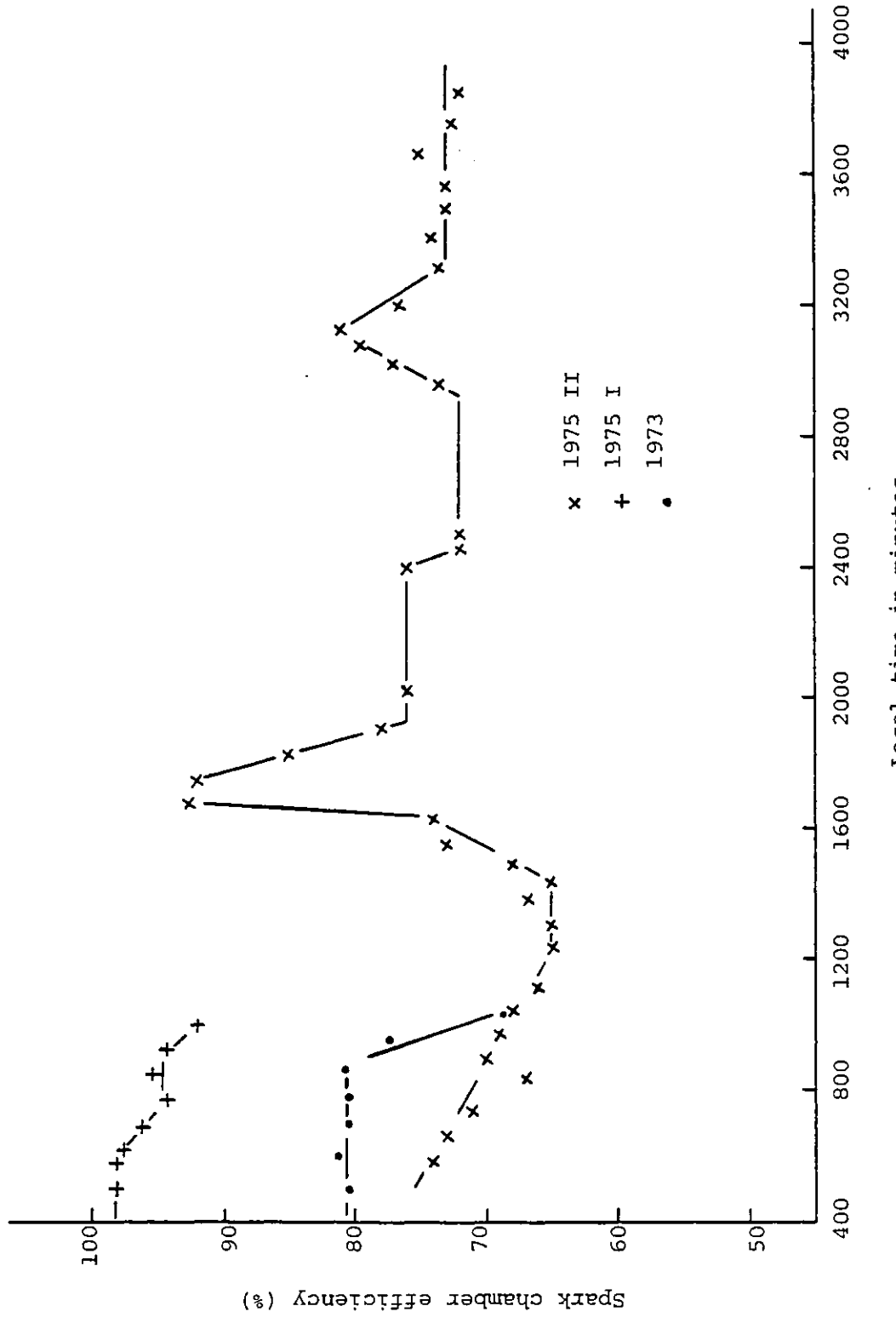

Figure 3.1 Spark chamber efficiency as a function of local time for the 1973, 1975 I and 1975 II flights.

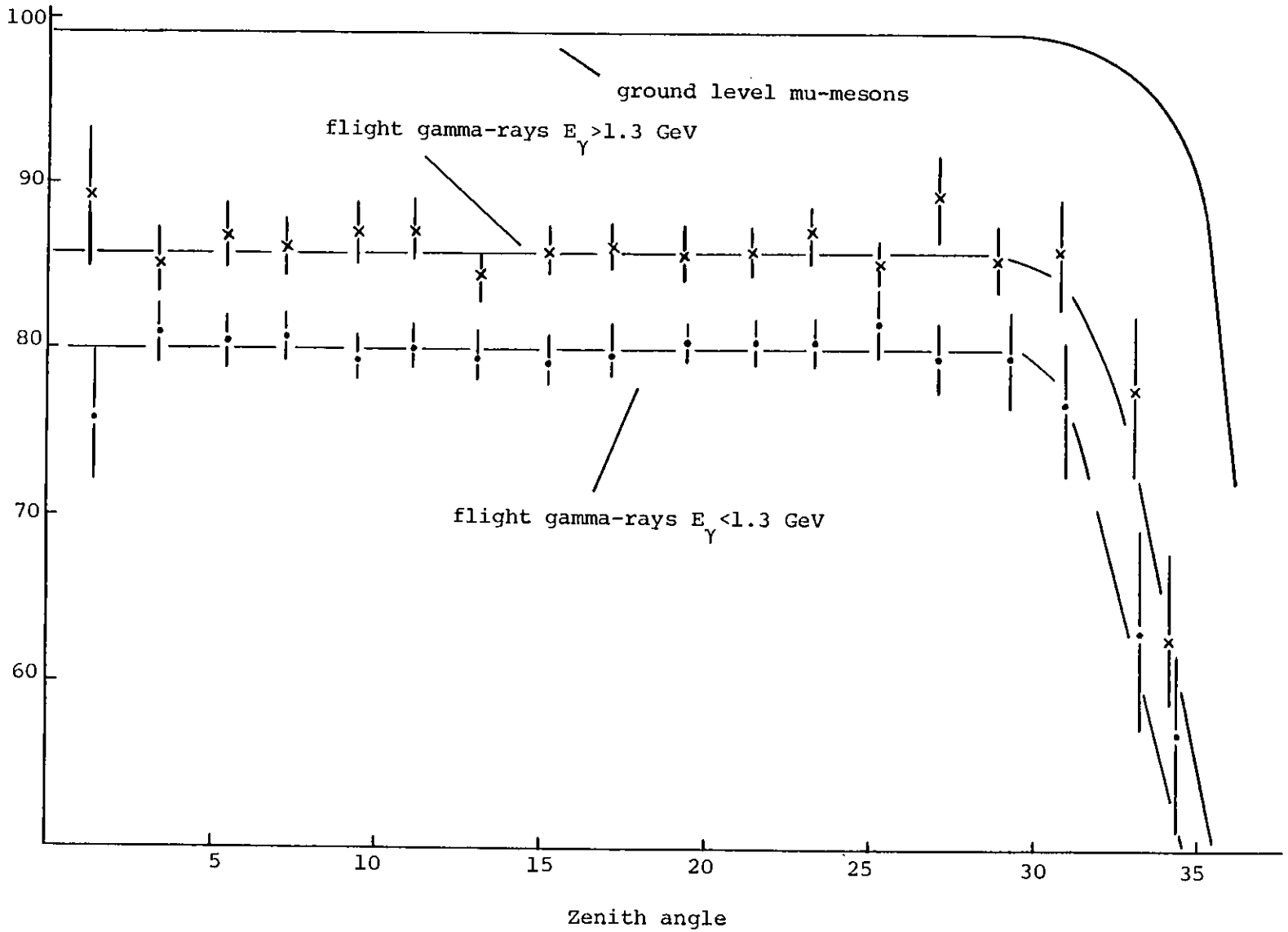

Figure 3.2 Spark chamber efficiency as a function of zenith angle.

the detector exposure (see section 4.3.4).

3.2.2 Spatial and Angular Resolution of the Spark Chamber

The position of the sparks was determined by gating on and off a 2.15 MHz clock (see section 2.5). The times were converted into distances using the following formulae :

Single track events

$$X_i = \{ \frac{(t_{1i} + (t_{av_i} - t_{2i}))}{2} - (OR_i + DOR_i) \} \times Sc$$

where X_i is the spark coordinate in cms (i^{th} plane), t_{1i} and t_{2i} are the spark numbers ($t_{3i} = 192$) and t_{av_i} is the most probable value of $(t_1 + t_2)$ as defined in the previous section, OR_i and DOR_i are the origin and adjustment parameters for the i^{th} plane (see section 4.3.2) and Sc converts from clock cycles (spark numbers) to centimetres.

Double track events

In this case, $t_3 \neq 192$.

$$X_{iI} = \{ \frac{(t_{1i} + (t_{av_i} - t_{3i}))}{2} - (OR_i + DOR_i) \} \times Sc \qquad \text{Track 1}$$

$$X_{iII} = X_{iI} + (t_{3i} - t_{2i}) \times Sc \qquad \text{Track 2}$$

The frequency of the crystal-controlled clock was limited to 2.15 MHz by the speed of the integrated circuits used in the stores, choice of these integrated circuits being determined by power requirements on board the detector. By timing the signal at both ends of each wire it was possible to locate each spark to ± 0.5 digit or ± 1.25 mm in each coordinate, or about ± 1.5 mm for each spark. Making the conservative assumption that there was no gain in angular resolution by making a least squares fit to 3 or 4 sparks as against drawing a line through only two, we have a basic

angular resolution for the spark chamber of ± 1.5 mm/150 mm = ± 0.6°, where the distance between corresponding spark planes was 300 mm.

3.2.3 Line Fitting Criterion

A least squares fit was performed on the tracks in the spark chamber. A tolerance ± S was placed on the deviation of the spark coordinates from the best-fit line and events having coordinates outside this tolerance were rejected. Tests using cosmic ray mu-mesons showed that 68% of events were accepted when the tolerance for each plane was ± 0.8 mm. The corresponding value of S for gamma-rays was similar. In flight the tolerance was set to 0.5 cm on all planes in order to accept 98% of gamma events.

3.3 The Lead Converter

3.3.1 Converter Efficiency

The efficiency of the half a radiation length of lead in converting gamma photons into electron-positron pairs was measured using the tagged gamma beam at DESY and was found to agree closely with theoretical predictions (see Figure 3.3 which shows the conversion efficiency for axial photons as a function of photon energy, with and without the anticoincidence shield). Theoretically, the conversion efficiency ε is given by

$$\varepsilon = [1 - \exp(-1/2.7/9)] = 0.325$$

given that a radiation length is 7/9 of an interaction length for pair conversion. The effect of the anticoincidence shield was to reduce the efficiency by 2% to 30%.

The effective thickness of the converter as presented to the

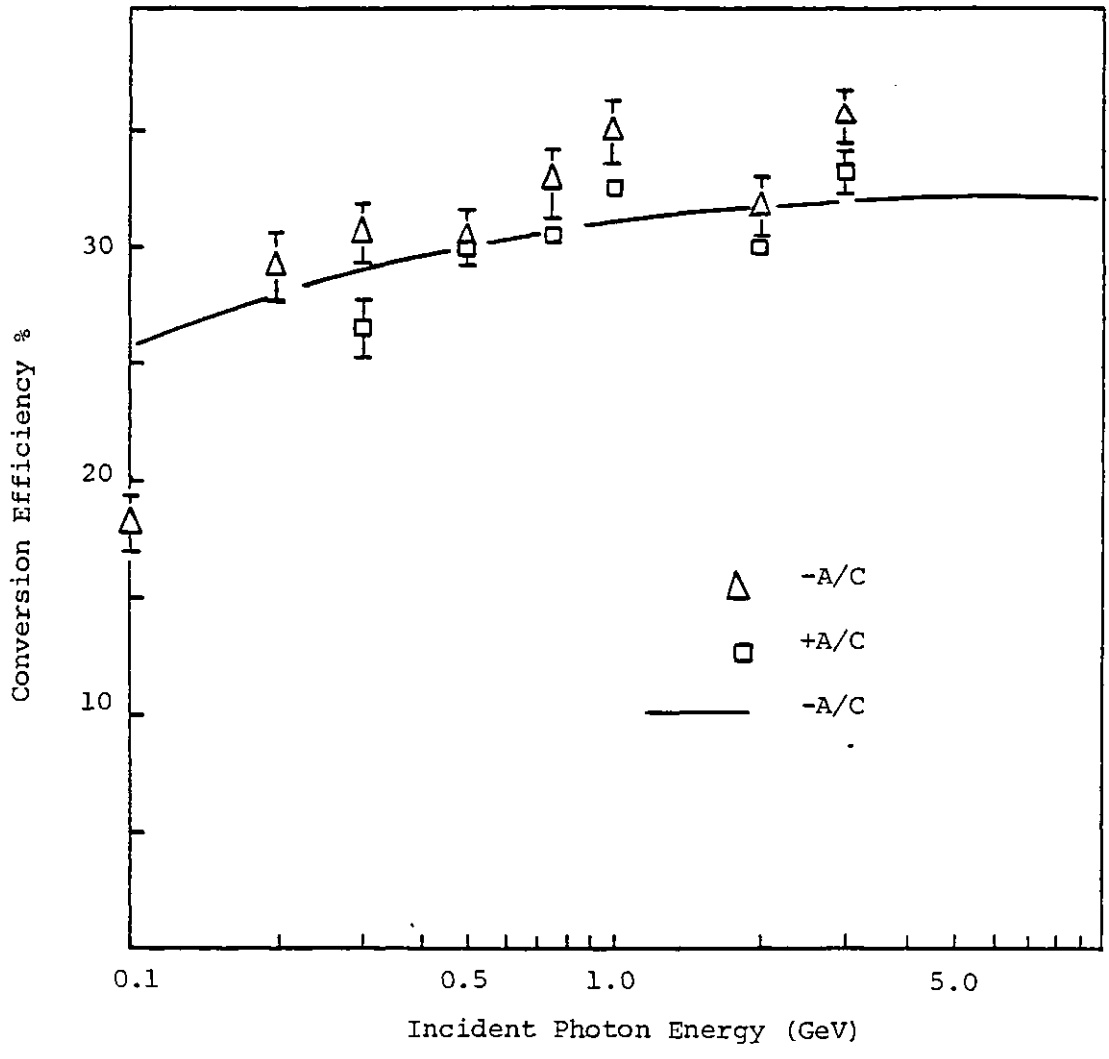

Figure 3.3 Experimental and theoretical conversion efficiencies as a function of photon energy for axial photons with and without the anticoincidence (A/C) shield.

incident photon was of course a function of the angle of incidence and the efficiency varied accordingly. The radial dependence of the conversion efficiency revealed a fall-off at distances of $\sim$ 10 cm due to increased scattering of slow electrons into the anticoincidence shield. Further discussion of the radial dependence will be postponed until section 3.8.

3.3.2 Scattering in the Lead Converter

The theory of electron scattering in lead was reviewed by Clayton (1975) so only a brief summary is given here. The divergence of the trajectories of the electron and positron from the photon's incident direction was initiated during the process of pair production itself but arose mainly from multiple Coulomb scattering in the lead traversed after materialisation. This effect was examined by Olsen (1963) who obtained an expression for the opening angle θ after scattering :

$$\theta = \frac{2a\ [1 + \frac{\ell n\ 2a^2 + 1.29}{4a^2}]}{E_\gamma} \quad \text{radians}$$

and $$a^2 = \frac{0.21\ Z(Z+1)L}{A} \cdot \ell n\ (\frac{196}{(ZA)^{1/6}})$$

where E_γ is the energy of the parent photon in MeV; Z,A are the atomic and mass numbers of the scattering medium (for lead, Z = 82 and A = 217.2) and L is the thickness of material traversed after materialisation. L (in gm/cm^2) was investigated by Bennett (1973), who derived a distribution of scattering angles for 100 MeV electrons produced at various depths in 1/2 r.l. of lead and compared this with the corresponding distribution for 1/4 r.l. of lead. Because the peaks of the distributions occurred at approximately the same angle, Bennett concluded that, on average, electrons produced in the lead were scattered by 1/4 radiation length. With L =

1/4 r.l. in the formula above, the opening angle of the electron and positron is $\sim 7°$ for a 200 MeV photon and the error in the bisector of the tracks, which defines the photon arrival direction, is $\sim 2°$. However the above formula assumes equipartition of energy between the electron pair.

The physical model was improved when a partition of energy between the electron and positron was taken into account, as described by Rossi and Greisen (1941). They presented their results in the form of normalised curves, showing the probability per r.l. of lead of an electron carrying an energy E' from a photon of energy E for different photon energies (see Figure 3.4). The curves were used by Clayton (1975) to deduce average energies for the low and high energy members of the pair (see Table 3.3).

TABLE 3.3

photon energy (MeV)	average energy of low energy electron (MeV)	scattering angle for 1/4 r.l. Pb (degrees)		average error in photon direction estimation (degrees)
		Low energy	High energy	
200	50	7.35	2.36	5.13
300	72	5.0	1.57	3.48
500	120	3.0	1.0	2.1
1000	235	1.5	0.5	1.05
3000	700	0.5	0.2	0.35
5000	1160	0.3	0.1	0.2

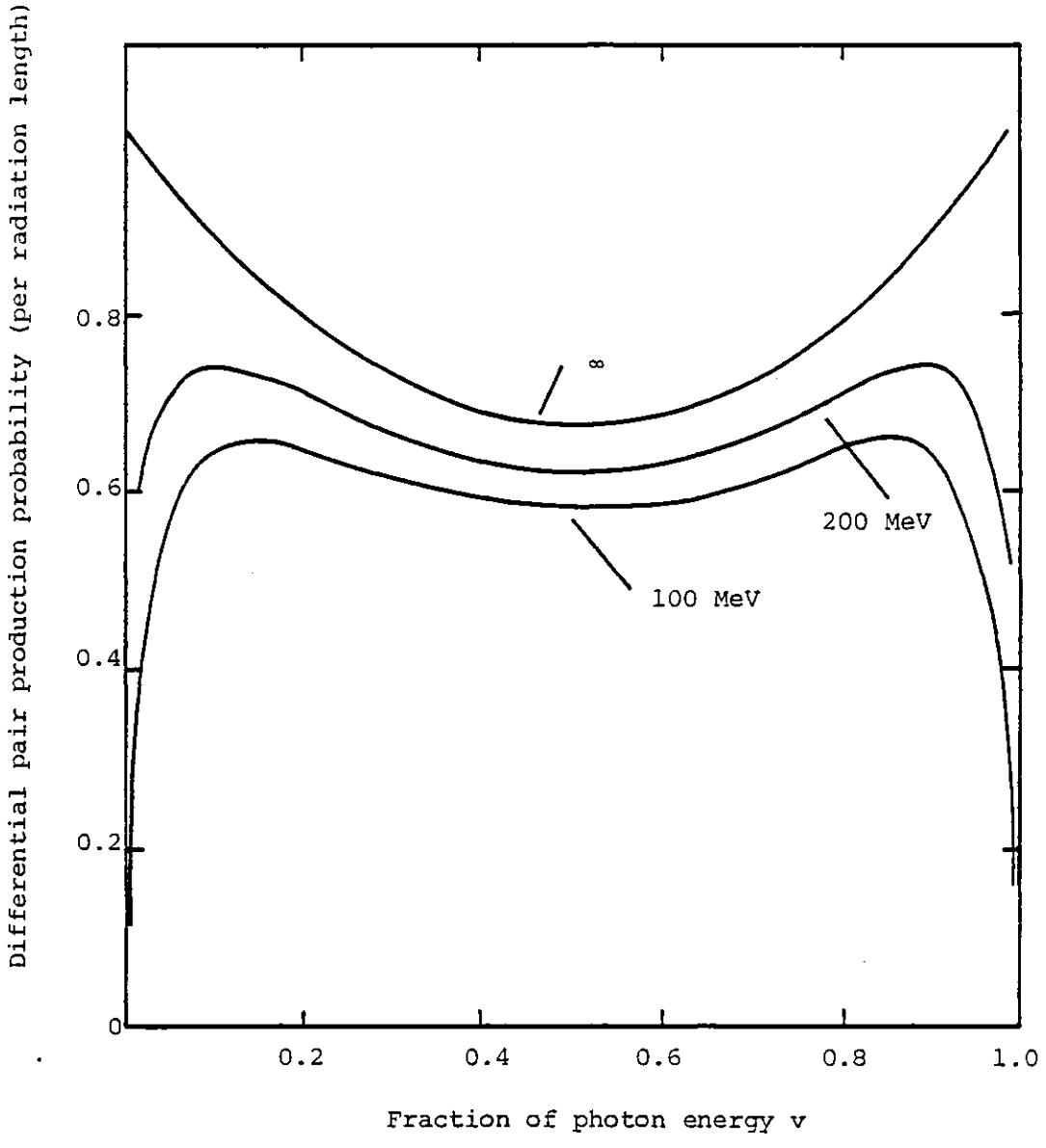

Figure 3.4 Differential probability of pair production per radiation length of lead for photons of various energies. Abscissa $v = (E' + m_e c^2)/E$, ordinate = $E\phi_{pair}(E,E')$ (after Rossi and Greisen, 1941).

The indication was that, on average, one electron carried off only 25% of the photon's energy at 200 MeV, reducing to 20% at 5 GeV. This meant that one electron was scattered very little compared with its lower energy partner, to which the loss in angular information was mainly due.

In some cases, the low energy electron would have been absorbed by the lead or spark chamber walls. However, the other electron having undergone only a small amount of scattering, would have represented the photon's incident direction with high precision. Also its energy would be $\sim$ 75% of that of the photon, the loss of energy being comparable with the energy resolution of the detector. But, if the low energy electron was scattered into the anticoincidence shield, then the gamma event would have been lost.

3.4 Orientation of the Payload

The orientation of the detector with respect to magnetic north was measured using a three-axis fluxgate magnetometer. This was accurate to within 2 digits in 1000, corresponding to an average error of about $\pm$ 0.3°. The axes of the magnetometer were aligned with those of the spark chamber to within $\pm$ 0.2°, which also contributed to the orientation error. The magnetometer values were checked with those of a solar sensor to confirm, ideally, that the alignment of the magnetometer had not been disturbed during the balloon launch. However, a meaningful comparison was not possible in 1975 because the window of the solar sensor was too large and consequently the solar bearing angle measured by the instrument was only accurate to $\pm$ 5°.

The field measurements obtained from the magnetometer readings were compared with those of the International Geomagnetic Reference Field (IGRF) (IAGA, 1975). The accuracy of the IGRF, which could be in error

due to local topographical features, was itself checked by comparing the magnetic declination computed using the IGRF model with that published on an aerial survey of the magnetic field over Australia. The difference between the two values was $< \pm 0.1°$ throughout the flights.

The difference in the field components measured by the magnetometer and the IGRF values was plotted as a function of time on the computer. The observed modulation of the vertical and horizontal field components (B_Z, B_H respectively), as the payload rotated, revealed two separate effects. A sinusoidal variation in B_Z was due to a small angle of tilt of the detector from the vertical, which was caused by slight inequalities in the tension of the suspension. For flight I, 1975, the mean difference in the two values of B_Z was about 200γ, which corresponded to an angle of tilt of 0.4°. For flight II, 1975, the angle of tilt was 0.3°, since the average difference was 150γ. The angles of tilt remained constant throughout the respective flights.

The second effect was due to the residual magnetisation of the metallic detector. This effectively introduced a field vector fixed to the detector which modified the true horizontal field component as the payload rotated. For flight I, 1975, the residual magnetisation was about 500γ, reducing to 200γ for the second flight.

Corrections for the angle of tilt and the magnetisation resulted in agreement between the field measured by the magnetometer and the IGRF value to within ± 30γ for both flights. This compared favourably with the digitisation error of the magnetometer (100γ).

3.5 Experimental Measurement of Angular Resolution

Contributions due to the limited spatial resolution of the spark chamber, the Coulomb scattering of the electrons in the converter and the orientation error of the instrument when on the balloon were summed to

give the overall angular resolution. This is plotted as a function of gamma energy in Figure 3.5 using ± 0.8 cms for the spatial resolution of the spark chamber (68% of events accepted). Also shown in Figure 3.5 are values obtained by Clayton (1975) for the experimentally measured angular resolution. These results were determined using the tagged gamma beam at DESY, Hamburg by measuring the spread away from the known beam direction as a function of gamma energy. (The angular resolution was defined as the cone angle containing 68% of events when a parallel beam of gamma rays was incident.) It can be seen that the experimental points are a good fit to the theoretical curve. Figure 3.5 also shows that the angular resolution was virtually independent of angle of incidence, as would be expected from section 3.2.1, since the spark chamber efficiency was constant out to a zenith angle of 32°.

3.6 Energy Resolution

3.6.1 Calorimeter Design

The optics of the lead glass calorimeter were designed so that, as far as was possible, the pulse heights produced when isoenergetic electrons were absorbed were independent of position and angle of incidence. The configuration chosen was tested after assembly, using large numbers of minimum ionising particles (cosmic ray mu-mesons) which passed right through the calorimeter. A special version of the calibration computer program (see section 4.3.2) was used to analyse the mu-meson data. The events were binned according to their angle of incidence and point of impact on the face of the lead glass and histograms of the lead glass pulse height were produced for the different bins. The number of photons produced by a mu-meson should depend only on its path length in the lead glass. However, even with a correction for path

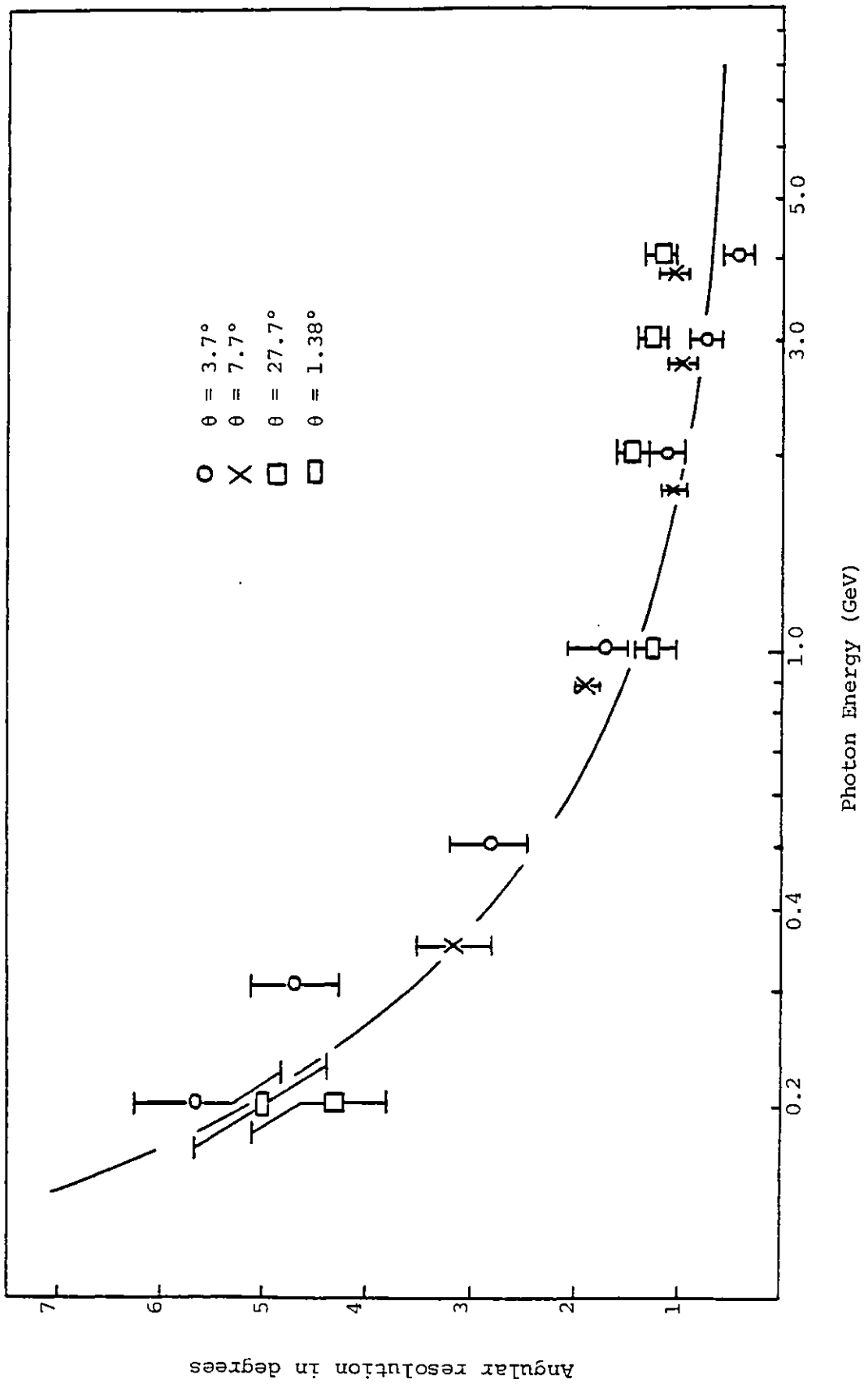

Figure 3.5 Measured angular resolution of the detector as a function of energy and angle of incidence compared with theoretical prediction.

length, the pulse heights were found to vary with azimuth, zenith and radial distance from the centre of the lead glass. This variation was due to the non-uniformity of the photon collection efficiency, which was seen to vary by up to a factor of 2.

To compensate for this, an average pulse height was first determined for each bin. The correction factor required to normalise the pulse height to the value for an axial particle was then stored. In this manner, a map of pulse height corrections was built up which, when applied to the raw pulse heights, produced a uniform response for particles incident at all angles and positions. The correction factors were found to be unchanged even after each detector had been dismantled and reassembled, including removal and remounting the photomultiplier tubes viewing the lead glass element. The corrections to the pulse heights were therefore considered to be a function of design rather than of chance fluctuations in the optical coupling, say. There was very little difference in response between the two units (see Figure 3.7).

Figures 3.6a,b show the mu-meson pulse height distribution before and after the application of this correction. It can be seen that the width of the mu-peak has been much reduced. A similar effect was observed when the correction was applied to the gamma data obtained at DESY. Thus the correction derived from the mu-data was also valid for the gamma-ray data, in spite of the lateral spread of the showers produced in the lead glass by the secondary electrons from a gamma event. This suggests that the shower cores did not have much lateral spread.

3.6.2 Energy Calibration for Gamma-Rays

The response of the two identical calorimeters was examined in the DESY tagged gamma beam at different photon energies and directions of incidence. Three positions of the detector with respect to the beam

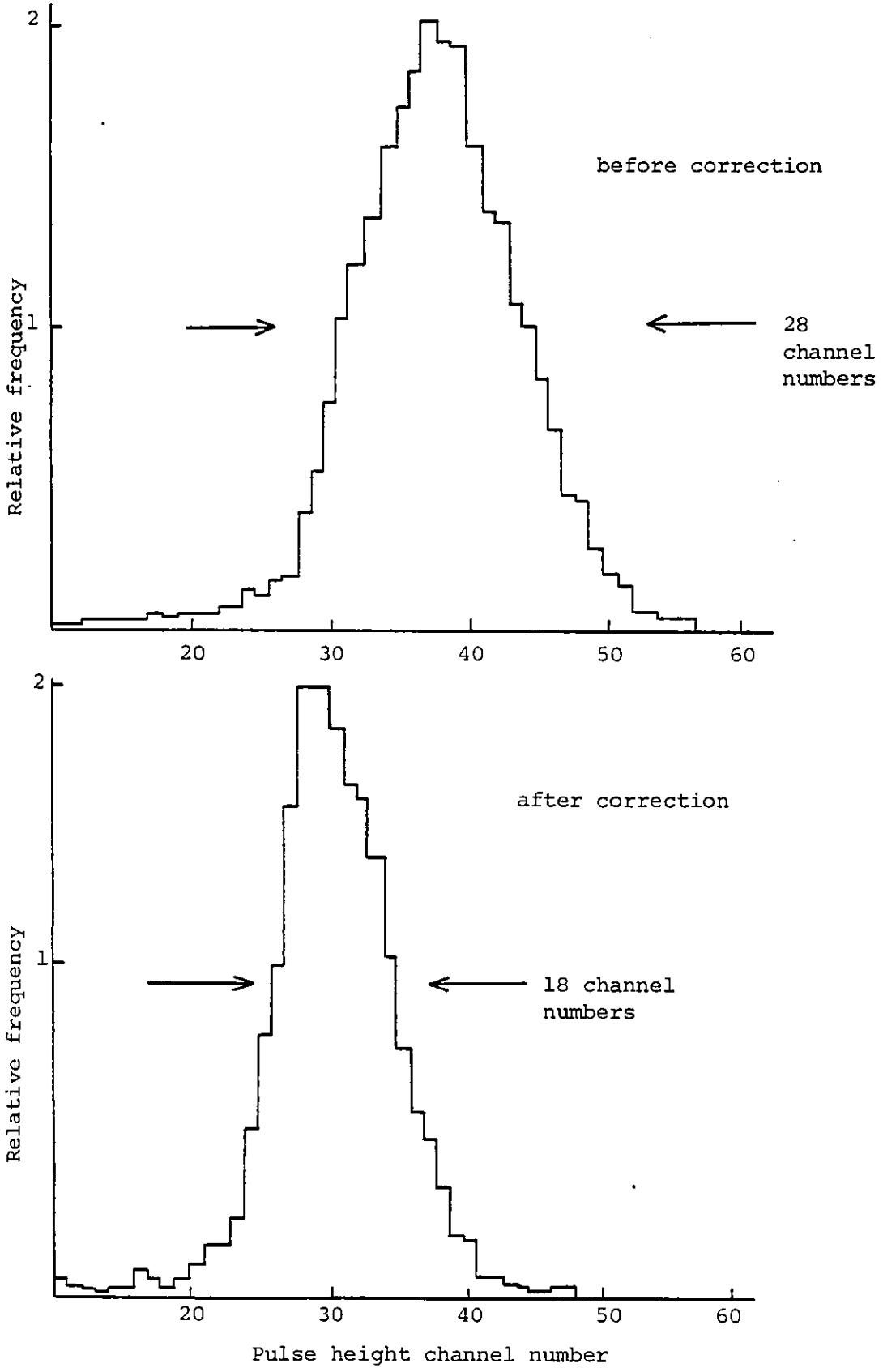

Figure 3.6 Mu-meson peak in the Cerenkov element (a) before (b) after correction for the photon collection efficiency.

direction were selected :

a) the gamma beam was incident along the axis of the telescope

b) the beam axis was again parallel to the telescope axis, but the point of intersection was 13 cm from the centre of the converter

c) the point of intersection was the same as b), but the beam was incident at an angle of 15°.

At each position, data was taken at four different photon energies - 0.3, 0.5, 1.0, 2.0 GeV. The gamma-ray data was later analysed by the main calibration computer program (see section 4.3.2) which included corrections for the variation in light collection efficiency mentioned in the previous section. Histograms of the lead glass pulse height distribution were produced for the different energies and positions, and from these distributions the positions of the pulse height peaks were determined. The response of the calorimeters at a given photon energy was the same for the three positions, which confirmed that the pulse height corrections derived above were still applicable. Furthermore, the calibration of each calorimeter was sufficiently similar for the results of both to be combined, and this has been done in Figure 3.7. The vertical bars in this Figure include the error in the mean energy of the DESY gammas (see Table 3.1). A least squares fit to the experimental points is shown in Figure 3.7. The error in fitting this line represents the error in calibrating the calorimeter.

3.6.3 Energy Resolution for Gamma-Rays

In addition to the calibration error, the error in making an

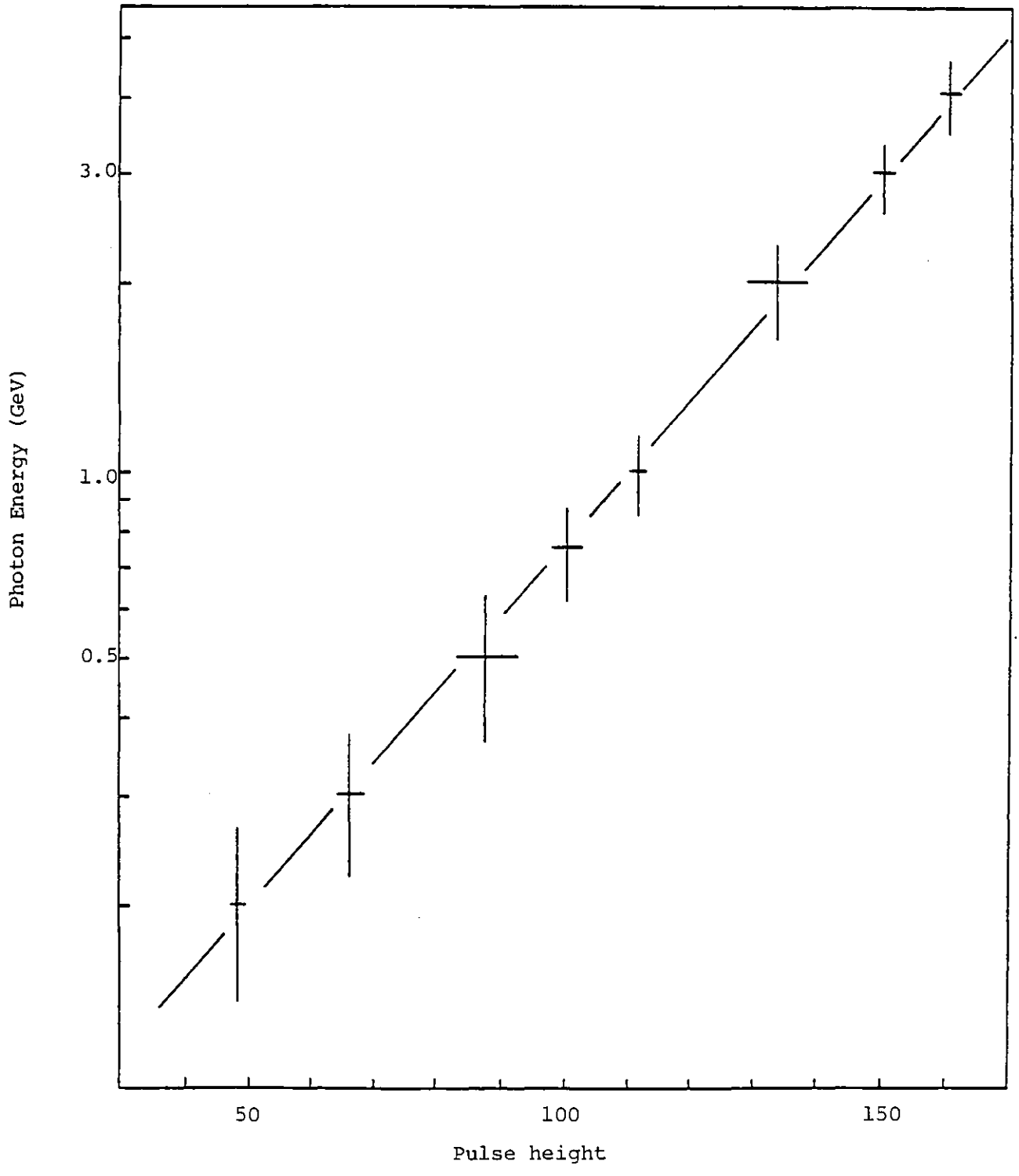

Figure 3.7 Energy calibration of the two calorimeters. The horizontal bars represent mapping and reproducibility errors only; the vertical bars include, in addition, errors due to beam calibration and photon statistics.

individual measurement, which depended on the statistics of shower development, and errors in the correction for variations in optical coupling efficiency also contributed to the overall energy resolution. The total energy resolution was obtained from DESY beam tests, as reported by Clayton (1975). It is shown as a function of energy in Figure 3.8, where the energy resolution was defined by saying that the probability was 68% that the true energy differed from the measured value by less than the resolution. In Figure 3.8, $\Delta E/E$, where ΔE is the error in the energy measurement E, is quoted as a percentage error and $2\Delta E$ includes 68% (by definition) of the events.

3.7 Scintillator C

The ½" scintillator C was used to determine the number of electrons which passed from the spark chamber to the lead glass calorimeter D. A gamma ray was nominally converted into a pair of electrons, however if the gamma ray had sufficiently high energy, shower formation could commence in the lead converter and several electrons might pass through C. A knowledge of the number of electrons which passed through C could be used to discriminate against noise events in the flight data, which were usually single tracks.

The pulse height obtained when a charged particle traversed the scintillator was a function of path length and also path location. The dependence on path location was due to a non-uniformity in the photon collection efficiency across the scintillator (cf. lead glass counter). An empirical correction for this variation was made using ground-level cosmic rays (mu-mesons and fast electrons). The data was analysed by a modified version of the calibration program, which binned the events according to their point of impact and produced scintillator pulse height distributions of the different bins. A map of the

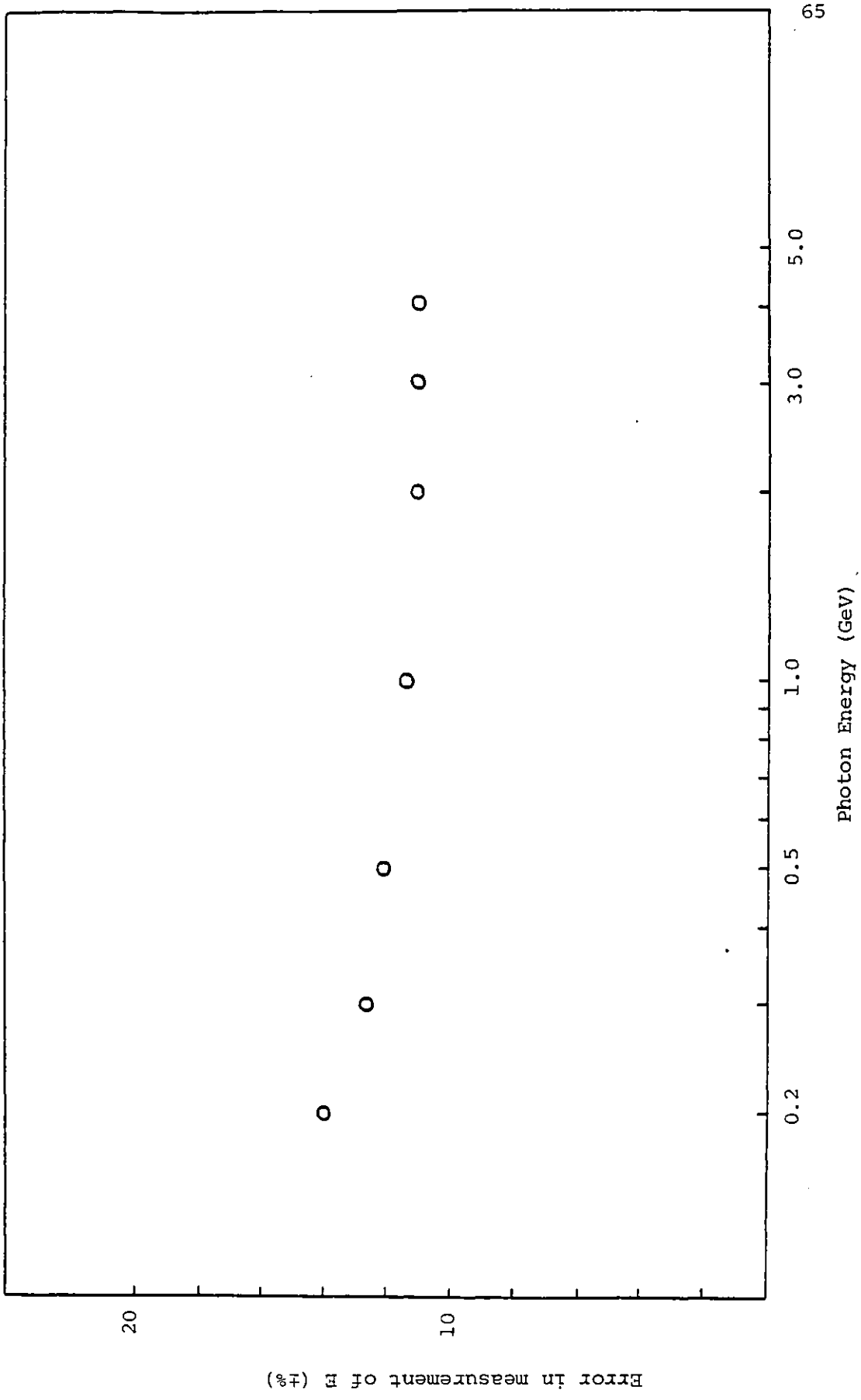

Figure 3.8 Energy resolution as a function of energy E, derived from DESY beam tests.

scintillator was then constructed, containing the correction factors required to normalise the pulse heights across the face of the scintillator to the value for an axial particle. Figure 3.9 shows the pulse height distribution a) before and b) after the correction. It can be seen that the width of the peak has been reduced after applying the correction, although the peak is still wider than it would be for a pure mu-meson flux because of the presence of fast electrons (in the cosmic ray hard component) with a different Lorentz factor causing a slightly higher pulse height.

Figure 3.10 shows a corrected scintillator pulse height distribution for gamma rays of energy about 1 GeV obtained in a DESY beam test and also from the flight data. The excess in the single electron channel of the flight distribution was due to leakage of charged particles through the anticoincidence shield and back-scattered products caused by cosmic ray interactions in the lead glass calorimeter. In order to remove these noise events, a cut-off was imposed on the scintillator pulse height somewhat above the single electron peak. Those single tracks arising from true gamma events (in which one electron had been scattered out of the telescope or been absorbed, leaving only the other electron to pass through C) would also be rejected, but their proportion as a function of energy was known from DESY beam tests.

Figure 3.11 shows the single track fraction as a function of photon energy for R = 0&13 cm, where R is the distance of the point of intersection of the DESY gamma beam from the telescope axis (see section 3.6.2). The single track fractions were calculated from the scintillator pulse height distributions produced for the various combinations of energy and position examined at DESY. (The gamma-ray data was analysed by the calibration computer program, which included

corrections for path length in the scintillator and photon collection efficiency across the scintillator.) The pulse heights corresponding to the one-electron and two-electron peaks were noted and the mid-value, corresponding to 1.3 electrons because of the logarithmic scale, was obtained. The proportion of events with scintillator pulse height less than this value was the single track fraction. Figure 3.11 shows that the single track fraction increased as the distance R increased beyond 10 cm. This was due to losses out of the system by scattering. Table 3.4 compares the single track fraction measured at DESY with that obtained during the flights, for different energy ranges.

Correction factors for the loss in efficiency were introduced in the flux calculations (see section 5.1.3).

TABLE 3.4 SINGLE TRACKS AS % OF TOTAL EVENTS
($R \lesssim 10$ cm)

E(GeV)	DESY	FLIGHT 1973	FLIGHT I 1975	FLIGHT II 1975
0.3	26.1±3.1			
0.5	16.6±0.1			
0.3<E<0.6		62.3±6.0	69.7±4.9	67.0±3.6
1.0	12.7±0.2			
0.6<E<1.4		43.7±3.4	58.5±3.5	51.9±3.2
2.0	11.1±0.3			
1.4<E<2.5		44.3±4.4	55.3±3.2	
1.4<E<5.0				51.5±4.8

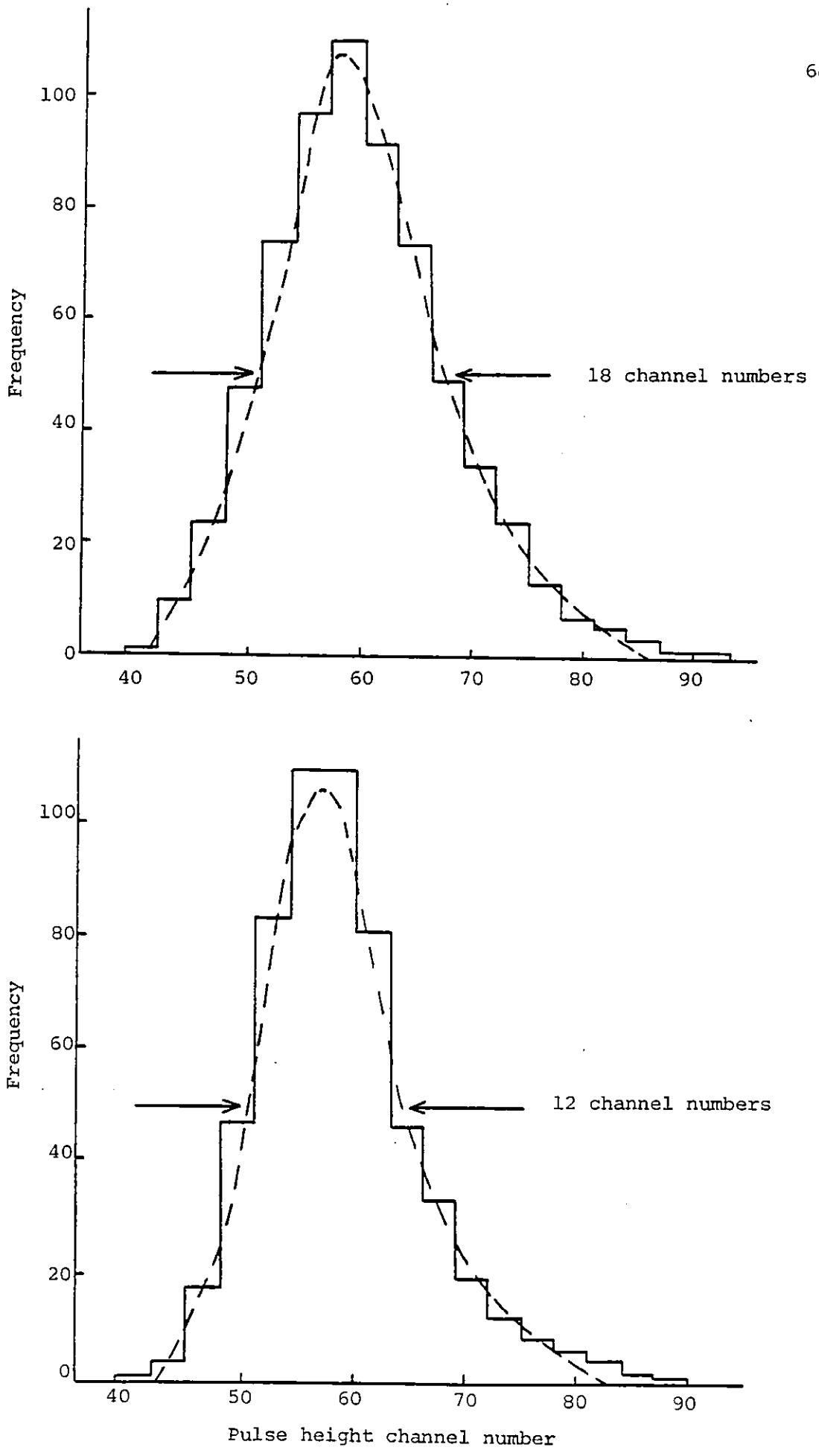

Figure 3.9 Pulse height distributions from scintillator C for mu-mesons (a) before and (b) after correction for photon collection efficiency.

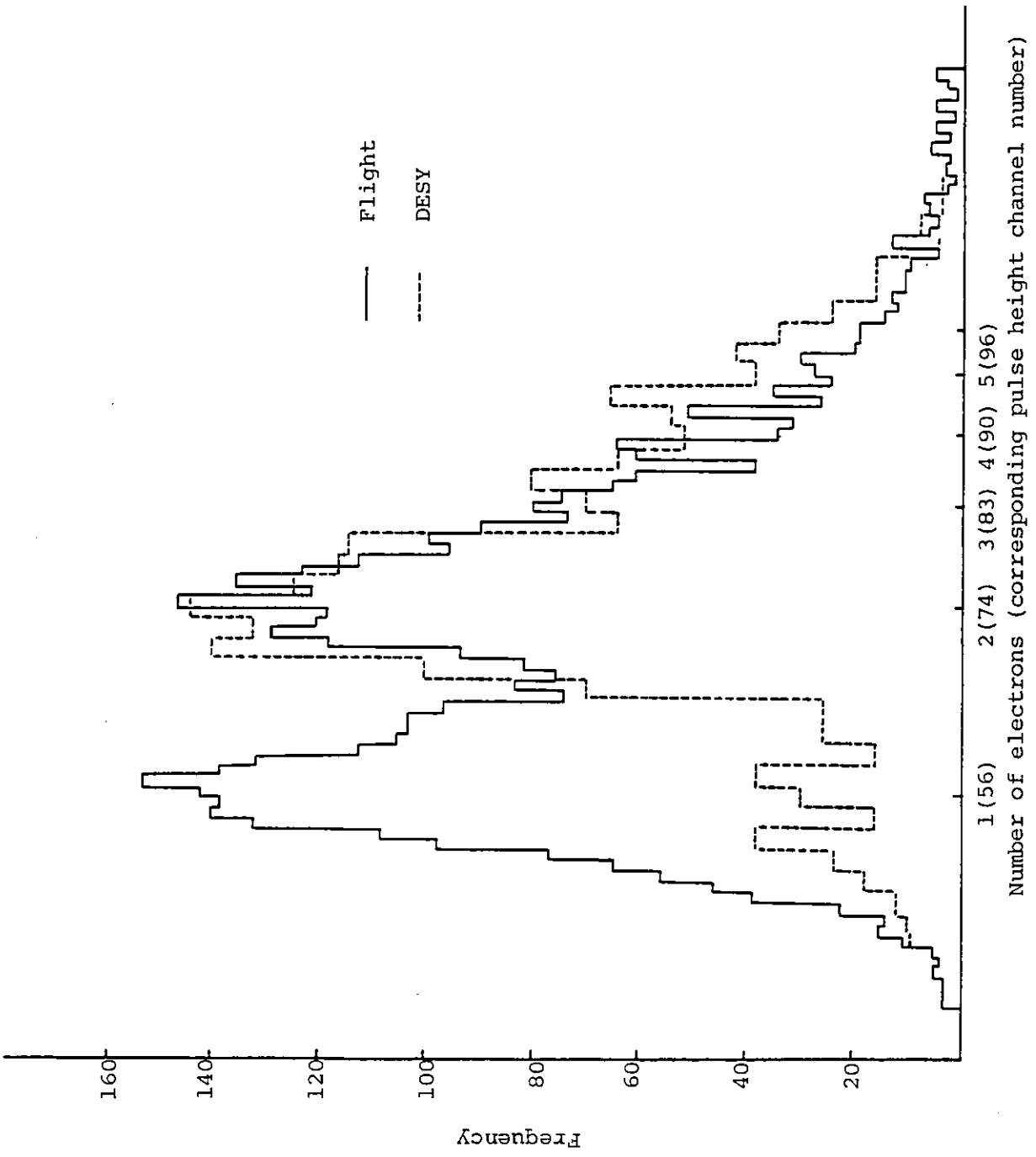

Figure 3.10 Pulse height distribution from scintillator C for gamma rays of energy 1 GeV, at altitude and in the DESY beam test.

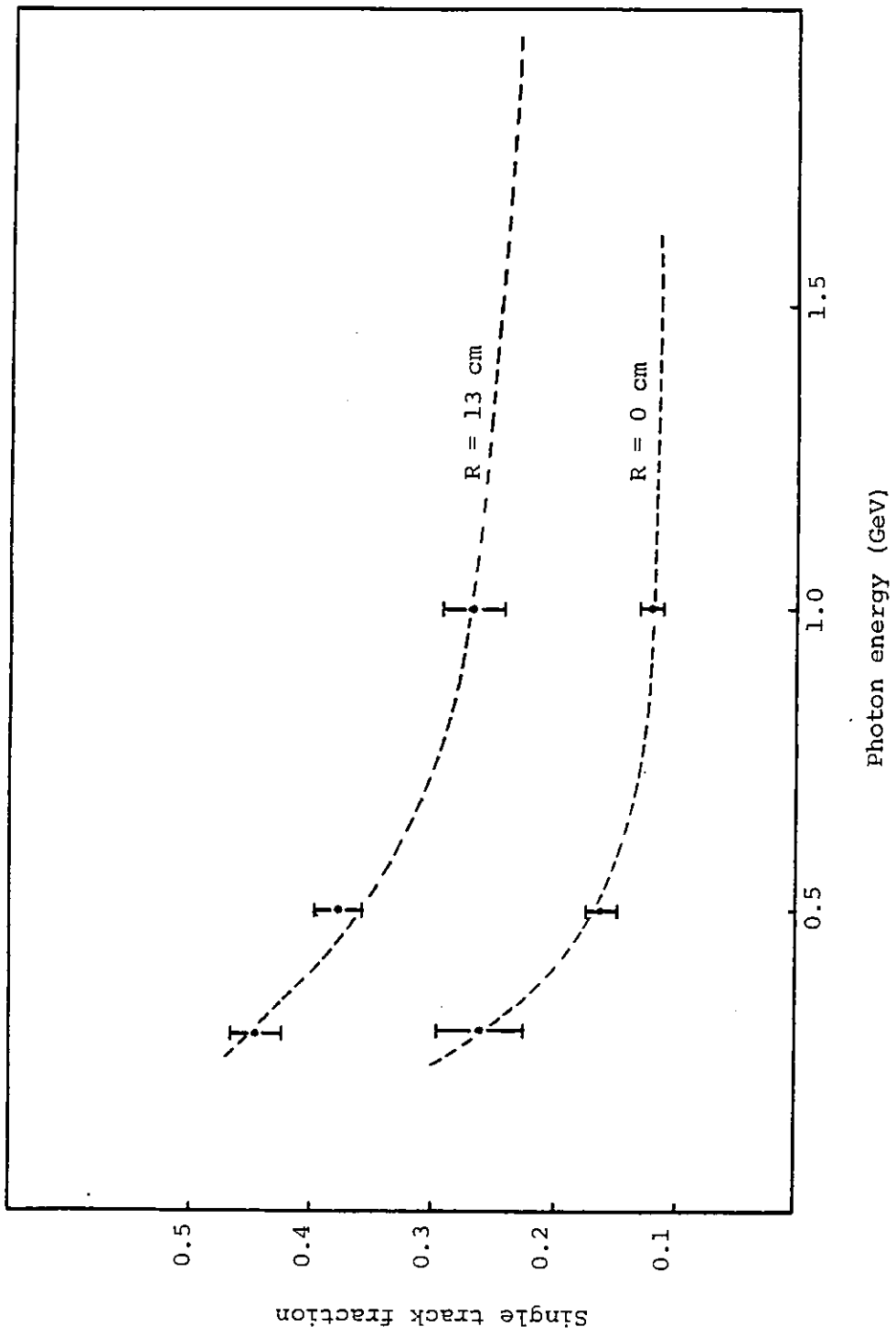

Figure 3.11 Proportion of single track events as a function of energy for R = 0, 13 cm, derived from DESY beam tests.

3.8 Radial Dependence and Geometry

As only gamma events having two or more charged particle tracks were accepted, and as the proportion of single track events was a function of the radial impact point R (see Figure 3.11), the efficiency of the telescope therefore depended upon R. The existence of a radial efficiency of the telescope was also apparent in section 3.3.1, where a fall-off in the conversion efficiency at distances of about 10 cm from the axis of the telescope was described. This was explained by anticipating, at large radial distances, a greater probability of one of the electrons being scattered out of the telescope geometry and triggering the anticoincidence shield.

The radial efficiency of the telescope could not be calculated theoretically but was determined empirically from the data obtained at altitude by examining the zenith dependence of the atmospheric gammas. The dependence on zenith angle was studied because this would be affected by the radial efficiency of the telescope, since photons incident at large zenith angles could only trigger the telescope if they impinged at the edge of the converter. It was assumed that the atmospheric flux varied as sec θ (where θ is the zenith angle) and that deviations from this were instrumental in origin.

A computer program was written to fit the observed zenith distribution and this is reproduced in Figure 3.12. In order to produce a theoretical distribution, the area presented by the detector (the 'overlap area') was calculated as a function of zenith angle. The overlap area function, which is derived in section 4.3.4, involved another unknown instrumental parameter - the effective length of the telescope. This was the distance between the lead converter and the plane in the lead glass where sufficient energy (a minimum of 200 MeV) was deposited to trigger the system. Since this plane was an unknown

distance below the upper surface of the glass and this distance was difficult to calculate theoretically, the effective length was used as a free parameter.

The overlap area was compounded with the angular dependences of the lead converter and the spark chamber respectively, and a simple analytic function representing the radial efficiency. In order to simulate the angular resolution of the detector, Gaussian scatter was introduced into the distribution. After suitable normalisation, a chi-squared (χ^2) test was performed in the program to find the best fit.

To summarise, the observed zenith distribution of the atmospheric flux was fitted with two parameters; the effective length of the telescope and a function defining the radial efficiency. Both parameters were found to be slightly dependent on energy. They were subsequently used to calculate the effective exposure of the detector in the atmospheric and galactic flux calculations.

A sample output of the computer program used to fit the observed distribution is shown in Figure 3.13. The predicted and the observed number of photons in each 1° zenith bin are tabulated and displayed graphically (X ≡ theoretical value). Also shown is the χ^2 value for the given number of bins.

```
      PROGRAM PROFILE(INPUT,OUTPUT,TAPE6=OUTPUT)
      DIMENSION ARR(45),ARRAY(45),IARRAY(100)
      DIMENSION COUNTS(45),FRAC(45)
      DATA (COUNTS(I),I=1,45)/119.,282.,348.,502.,597.,668.,837.,916.,10
     +11.,1070.,1201.,1205.,1239.,1261.,1302.,1328.,1379.,1315.,1289.,12
     +35.,1242.,1253.,1119.,1052.,969.,919.,829.,788.,652.,604.,498.,457
     +.,363.,284.,253.,169.,122.,113.,79.,47.,31.,20.,15.,13.,6./
      DATA IBLANK,IX,IY/1H ,1HX,1HO/
      SUMC=0.
      CMAX=0.
      DO 1 I=1,45
      SUMC=SUMC+COUNTS(I)
1     IF(COUNTS(I).GT.CMAX)CMAX=COUNTS(I)
      WRITE(6,2)SUMC,CMAX
2     FORMAT(1H0,*SUM OF COUNTS =*,F6.0,/,* MAX OF COUNTS =*,F6.0)
      R=19.
      D=2.*R
      DO 6 N=1,6
      AL=45.0+FLOAT(N)
      DO 7 K=1,45
      ANG=FLOAT(K)-0.5
      RATE=0.
      EG=AL*TAN(ANG/57.296)
      IF(EG.GT.D)GO TO 8
      S1=EG*SQRT(R*R-EG*EG/4.)
      S2=2.*R*R*ASIN(EG/D)
      SU=(3.14159*R*R-S1-S2)*COS(ANG/57.296)
      SPEFF=.86
      IF(ANG.GT.32.5)SPEFF=(50.+9.*(36.5-ANG))/100.
      RATE=2.*3.14159*SU*SIN(ANG/57.296)*(1.-EXP(-.416/COS(ANG/57.296)))
      REFF=COS(ANG/57.296)*COS(ANG/57.296)
      RATE=RATE*SPEFF*REFF
8     ARR(K)=RATE
7     CONTINUE
      DO 11 NN=1,4
      S=NN-1
      DO 12 J=1,45
      ARRAY(J)=0
      IF(S.EQ.0.)ARRAY(J)=ARR(J)
      IF(S.EQ.0.)GO TO 12
      DO 15 M=1,45
      XX=(J-M)**2
      X=SQRT(XX)
      IF(X.GT.4.0*S)GO TO 15
      IF(X.LT.0.1)X=0.25
      ARRAY(J)=ARRAY(J)+ARR(M)*EXP(-X*X/(2.*S*S))/(S*SQRT(3.14159*2.))
      X2=(J-1)+M
      ARRAY(J)=ARRAY(J)+ARR(M)*EXP(-X2*X2/(2.*S*S))/(S*SQRT(2.*3.14159))
15    CONTINUE
12    CONTINUE
      WRITE(6,499)AL,S
499   FORMAT(1H1,*LEN=*,F5.1,*SCATT=*,F5.2/*   ANG      RATE       FRAC *)
      AMAX=0.
      SUMF=0.
      SUMRATE=0.
      DO 9 KK=1,45
      SUMRATE=SUMRATE+ARRAY(KK)
9     IF(ARRAY(KK).GT.AMAX)AMAX=ARRAY(KK)
      SUMF=SUMRATE/AMAX
      SCALE=SUMC/SUMF
      IF(SCALE.GT.CMAX)CMAX=SCALE
      DO 10 KK=1,45
      FRAC(KK)=ARRAY(KK)/AMAX
      FRAC(KK)=FRAC(KK)*SCALE
-----------------------------------------FRAC APPEARED TO LEFT OF PREVIOUS =
      DO 5 I=1,100
5     IARRAY(I)=IBLANK
      IXX=FRAC(KK)/CMAX*100
      IYY=COUNTS(KK)/CMAX*100
      IF(IXX.EQ.0)GO TO 497
      IARRAY(IXX)=IX
497   IF(IYY.EQ.0)GO TO 498
      IARRAY(IYY)=IY
498   WRITE(6,500)KK,ARRAY(KK),FRAC(KK),(IARRAY(I),I=1,100)
500   FORMAT(1H ,I5,2F10.3,5(,1H,,100A1)
10    CONTINUE
      NBIN=0
      CHI=0.
      DO 13 JJ=1,45
      IF(FRAC(JJ).LT.200.)GO TO 13
      CHI=CHI+((COUNTS(JJ)-FRAC(JJ))**2/FRAC(JJ))
      NBIN=NBIN+1
```

Figure 3.12 Computer program used to fit the observed zenith distribution of the atmospheric gamma flux.

```
 79.   0033458    13    CONTINUE
 80.   0033518          CHIBIN=CHI/NBIN
 81.   0033538          WRITE(6,501)NBIN,CHI
 82.   0033648    501   FORMAT(1H0,*NO. OF BINS=*,I3,* CHI SQUARED=*,F6.2)
 83.   0033648          WRITE(6,502)CHIBIN,SUMRATE
 84.   0033748    502   FORMAT(1H ,*CHI PER BIN=*,F8.4,*SUMRATE =*,F8.2)
 85.   0033748    11    CONTINUE
 86.   0033778    6     CONTINUE
 87.   0034038          STOP
 88.   0034048          END
```

LIST OF VARIABLE AND ARRAY NAMES IN ADDRESS ORDER IN EACH BLOCK

BLOCK	LENGTH							
.LOCAL	317	002131B	IARRAY	0022758	IBLANK	0022768	IX
		0024318	ARRAY	0025068	ARR	0025638	IY
		0035738	I	0035748	K	0035758	M
		0036008	X	0036018	X2	0036028	CHI
		0036058	REFF	0036068	JJ	0036078	CMAX
		0036128	AL	0036138	ANG	0036148	RATE
		0036178	SPEFF	0036208	S	0036218	J
		0036248	SUMRATE	0036258	KK	0036268	SCALE
		0036318	NBIN	0036328	CHIBIN		

SUM OF COUNTS =31009.
MAX OF COUNTS = 1379.

Figure 3.12 continued

Figure 3.13 Sample output from computer program used to fit the zenith distribution.

CHAPTER IV

GROUND EQUIPMENT AND DATA ANALYSIS

4.1 Introduction

The ground station consisted of two steerable twin 7-element Yagi aerials with gains of $\sim$ 18 db and a single 3-element Yagi. One of the twin Yagi aerials was the main data receiving aerial and the other was used as a direction finder. In this aerial, a π phase difference was introduced between the elements so that a null resultant occurred whenever the aerial was pointing directly at the detector. The whole aerial system could be steered in zenith and azimuth to track the payload.

The single Yagi was used to transmit the transponder signal on the 108 MHz band. As described in section 2.7.1, this signal was received by an on-board transponder and retransmitted on the data channel (136 MHz). The time delay between the transmitted and received signals, which was observed on an oscilloscope, was measured to give the range.

The raw data from the main receiving aerial was preamplified, monitored on a GPR 20 FM receiver and then recorded on one track of a 7-track Ampex PR500 instrumentation tape recorder at 30 ips. The raw data was passed through a 124 kHz filter to extract the gamma-ray event information, which was recorded on two tracks on the Ampex. The house-keeping data from the Olland devices, which was transmitted on two subcarrier frequencies of 1.3 and 2.3 kHz, was monitored continuously

throughout the flights and decoded to provide temperature and pressure information. Figures 4.1a,b show the frame temperature as a function of local time for the 1975 flights.

Real-time monitoring of the gamma data was not possible, however tapes (which lasted ½ hour) were immediately played back, the data was punched on to paper tape and the paper tapes were analysed to check the in-flight performance of the detector. The playback speed of the tape recorder was set to 15/16 ips in order to drive the 'Facit' punch used in the transcription.

4.2 The Balloon Flights

As shown in Table 2.1, the two 1975 flights took place on November 7th and November 21st from Alice Springs in the Northern Territory (NT) of Australia. The flights lasted 11 hours and 60 hours respectively. The detectors were flown on large capacity balloons, which were manufactured by Winzen Research Inc., USA. Balloons of 6×10^6 cu.ft. and, for the second flight, 20×10^6 cu.ft. were used.

The launch site and the times of launch were chosen to provide optimum viewing of the Galactic Plane. The flights took place within an approximate three-week period in November, when the condition known as 'turnaround' exists in the upper atmosphere. Turnaround refers to a change in direction of the stratospheric winds, from a westerly to an easterly direction. During this transition the winds are relatively calm, which increases the likelihood of obtaining a long flight. Indeed, after the 60 hour flight, the detector landed only 180 miles north-west of Alice Springs. (Figure 4.2a,b shows the balloon tracks in geographic coordinates for the two 1975 flights.)

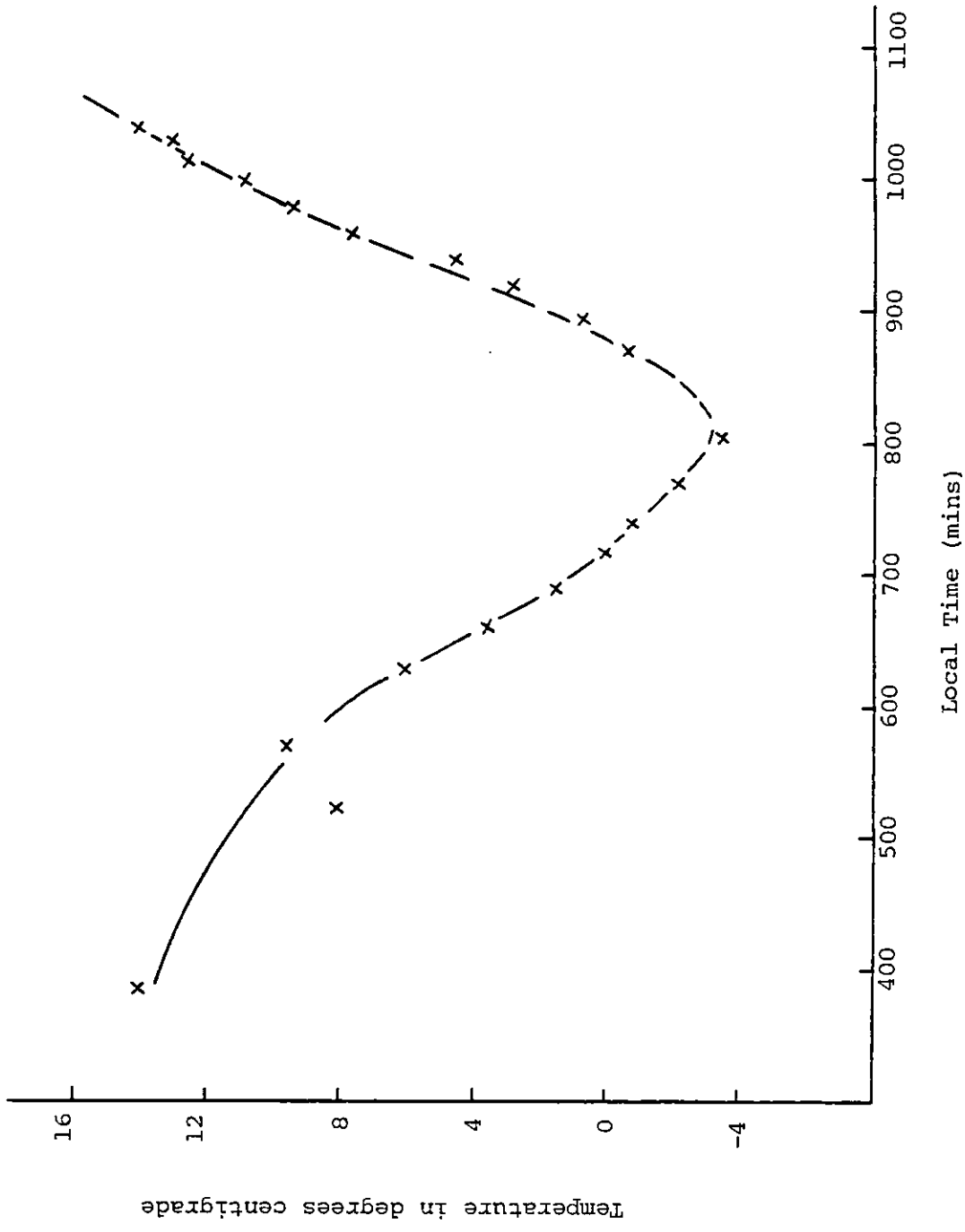

Figure 4.1a Temperature record for flight I 1975.

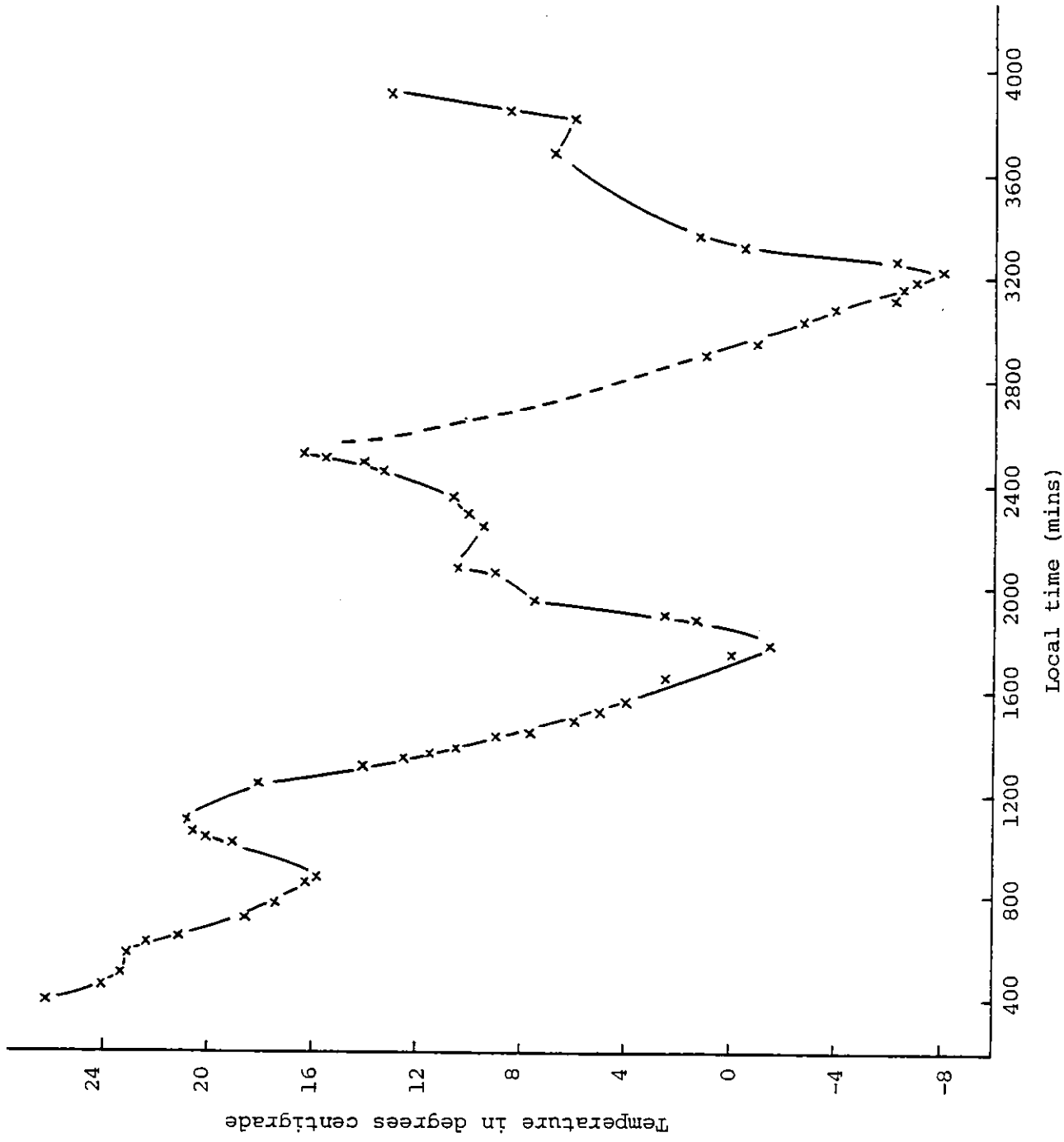

Figure 4.1b Temperature record for flight II 1975.

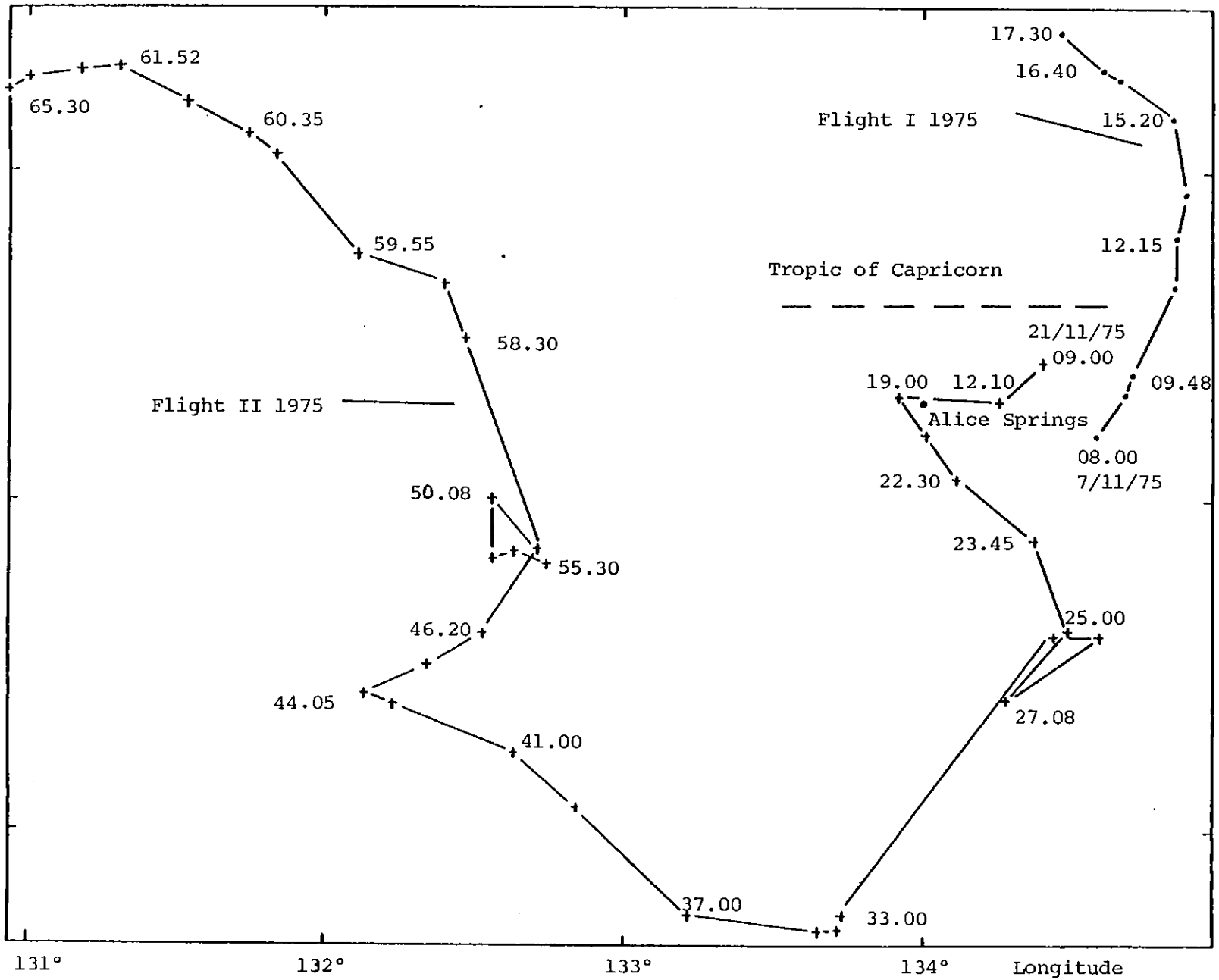

Figure 4.2 Balloon trajectory for (a) flight I and (b) flight II, 1975.

4.3 Data Analysis

4.3.1 Preliminary Analysis

The preliminary reduction of the data was performed on a PDP 11/40 minicomputer. The data was read off the magnetic tapes at 30 ips, was passed through a Schmitt trigger, which eliminated noise pulses and spikes, and was then buffered on to a storage disk. When the transfer of data had finished, a summary was printed, showing the number of accepted and rejected events. Events were rejected if they contained fewer than 282 bits. They were listed as 'very short' and 'short' events, depending on the number of missing bits. The summary also included the length of time required to read successive blocks of 500 events. Interpolation of this record was performed later to determine the times of individual events.

In the second stage of the transcription, the events written to disk were decoded and, if they satisfied various conditions, were written to magnetic tape. In this analysis, each event was initially checked for parity errors. The binary numbers of the various component parts of the event word (e.g. spark chamber, magnetometer, etc.) were then decoded, assuming, of course, that the two binary states could be distinguished (nominally, '1' corresponded to 32 pulses and '0' to 16 pulses). If the decoding produced impossible numbers, then the event was rejected. The accepted events were written to 7-track magnetic tape via an output buffer. Again a record of the accepted and rejected events was produced, together with a running cosmic ray total and examples of events written to tape.

Subsequent data analysis was performed on a CDC 6500 computer. Because of the different word structures of the PDP and CDC machines, data generated by the PDP 11/40 was converted into a format suitable for the CDC computer, and then re-written on to 7-track tape.

The programs used in the analysis of flight (or calibration) data are described below.

4.3.2 The Calibration Program

This was the main analysis program, which was used on calibration data obtained at DESY and in the laboratory, as well as flight data. The events were read from magnetic tape and then examined in considerable detail. In the program, the spark numbers (3 for each x- and y- plane) of each event were tested first of all. If the numbers did not satisfy the criteria for one or two sparks described in section 3.2.1, then the particular plane was flagged. Depending on the spark pattern, the gamma events were labelled as single or double track and were assigned a 'type number'. For example, an event was classified as type 1 if a satisfactory signal was picked up on all 4 x- (or y-) planes. All type 10 events and events of type 6-9 with two sparks detected on one plane were rejected, as explained in section 3.2.1. However, if two sparks were detected on two or more planes, then the event was labelled a double track.

The spark numbers were converted into spark coordinates in centimetres, using the formulae given in section 3.2.2. A least-squares routine was used to find a best fit to the coordinates, with a tolerance of 0.5 cm imposed on the deviations of the sparks. From the best fit line, the direction cosines of the incident gamma photon were calculated - in the double track case, the bisector of the tracks was assumed to represent the arrival direction. All tracks were extrapolated back to the lead converter to ensure they intersected there. In addition, for a double track event, the apex of the tracks had to lie within the converter plane.

The program also corrected the pulse heights obtained from the

½" scintillator C and the lead glass calorimeter. Both pulse heights were a function of path length and also path location, the dependence on path location being due to a variation in photon collection efficiency between different regions of the elements. To compensate for this variation, a table of corrections was included in the program. The corrections, which were determined empirically from mu-meson tests (see sections 3.6.1, 3.7) modified the raw pulse heights, to give a uniform response for isoenergetic particles irrespective of position and angle of incidence.

The lead glass pulse height was converted into a photon energy in MeV by a function representing the combined energy response of the two detectors (see Figure 3.7).

Events rejected in the spark pattern recognition routine or the line-fitting procedure were not discarded but were re-directed to a subroutine which attempted to reconstruct the event if sufficient information was available. The first half of the subroutine reconsidered the spark numbers (t_1, t_2, t_3 say) of the events. Previously, if one of the sensors on the magnetostrictive wire had failed to detect a spark (i.e. t_1 or t_2 was 192) then it was automatically assumed that no information could be retrieved and the plane was flagged. However, this might not be necessarily correct, because a missing number could still be deduced from the spark number of the complementary sensor (together with t_3, in the case of two sparks). Thus, the subroutine was adapted to generate missing spark numbers if the other numbers were sensible and satisfied the conditions described in section 3.2.1 for one or two sparks.

After converting the spark numbers into coordinates, the subroutine looked for suitable tracks to fit the coordinates. Events with two sparks only detected in the 4 x- (or y-) planes were now

accepted if one of the sparks occurred in the top pair of gaps and the other in the bottom pair. Events with three sparks could only be interpreted as single tracks. Thus, if two of the three sparks were observed on one plane, the event was rejected as before.

Single tracks were accepted as possible gamma-ray events because there were several instances in which a gamma-ray could give rise to a single track only. For example, one of the secondary electrons from a gamma event could be absorbed in the lead converter or spark chamber walls, leaving only one electron to pass through the spark chamber (see section 3.3.2). Or, the electrons could be sufficiently close together that the spark chamber was not capable of resolving the two tracks. (Of course, all single track events had to satisfy the scintillator cut-off criterion.)

In the subroutine, an event having four sparks was considered initially as a possible single track but if two of the four sparks were observed on the same plane, then the event was transferred to that section of the subroutine which looked for possible double tracks. Of course, events with more than four sparks were automatically directed to the double track section.

The search for possible double tracks began by choosing points in random pairs and constructing lines through the pairs. As in the single track analysis, the lines had to pass through the plane of the lead converter and the distances of the other points from the nearest line had to be less than a suitable tolerance. In the double track case, the apex of the tracks had to lie within the converter.

If single or double tracks were found which satisfied all the conditions, then missing spark numbers were filled in, the type number of the event was re-classified as 1 and the event itself was returned to the main program. It transpired that the 'reconstruction'

subroutine saved typically 15% of the events previously rejected.

The main calibration program could produce histograms of various parameters. These included

i) the sum of the primary delays (i.e. $t_1 + t_2$ or $t_1 + t_3$, for one or two sparks) used to set the average and maximum allowable values for each spark plane (see section 3.2.1). From the average values, t_{av}, the origins of the planes or the 'OR' parameters (see section 3.2.2) were computed, using the formula :

$$OR_i = \tfrac{1}{2} t_{av_i} - 20.0/Sc$$

where t_{av_i} is the average sum of the primary delays for the ith plane, 20.0 is half the length of the magnetostrictive wire in centimetres and Sc converts from centimetres to spark numbers.

ii) the distribution of spark coordinates across the planes which could reveal possible 'dead spots' on the planes.

iii) pulse height distributions from the lead glass and the ½" scintillator, before and after correction for photon collection efficiency

iv) the zenith distribution of the data, used to determine the effective length and the radial efficiency of the detector

v) the deviations of spark coordinates from the best fit line, which could indicate possible misalignment of a spark plane. The average value of the deviations was used to derive the 'DOR' parameters for the spark planes (see section 3.2.2).

Several versions of the calibration program existed. One version produced pulse height distributions of the lead glass element

split up into zenith, azimuth and radial bins. From the distributions, a catalogue of corrections was constructed and added to the calibration program, as mentioned earlier in this section and also described in section 3.6.1. The corrections compensated for the variation in photon collection efficiency. Another version of the calibration program produced similar distributions for the ½" scintillator. A third version produced histograms showing the frequency of events in which 2, 3 or 4 spark planes had fired, as a function of energy and zenith angle. These histograms were used to determine the absolute efficiency of the spark chamber (see section 3.2.1).

All versions of the calibration program could be used over any given time interval by defining a 'first' and 'last' event number in the program. Scintillator and energy cut-offs could be imposed so that only events within the ranges specified would be accepted. The program provided regular information summaries, showing the number of accepted and rejected events at different points in the program. An example of this summary is shown in Figure 4.3. It can be seen that the accepted and rejected events were also classified according to type number (from 1 to 10).

For the flight analysis, the event number, the direction cosines with respect to the detector axes (CX, CY, CZ), the scintillator pulse height, the energy in MeV and the magnetometer values of each acceptable event (including solar sensor events - see section 2.7.5) were written to magnetic tape.

4.3.3 The Flight Program

The flight program took its input data from the output of the calibration program. The main function of the flight program was to transform the direction cosines (CX, CY, CZ) of the events into the

TOTAL NO OF EVENTS ANALYSED = 10000 SOLAR SENSOR EVENTS = 35

NO OF EVENTS ACCEPTED FOR FURTHER ANALYSIS BY SIGNAL = 6471
NO OF SINGLE TRACK EVENTS = 6289
NO OF DOUBLE TRACK EVENTS = 182

EVENTS REJECTED IN COORDS = 0 EVENTS REJECTED IN LINEFT = 927
EVENTS OUT OF ENERGY RANGE = 111 EVENTS OUT OF SCINT RANGE = 2
EVENTS FROM BOSS = 55 EVENTS OUT OF GEOMETRY = 610

EVENTS WRITTEN ON OUTPUT TAPE = 4766

ACCEPTED EVENTS ARE CLASSIFIED AS FOLLOWS

TYPE =	1	2	3	4	5	6	7	8	9	10
X- PLANES	305	722	282	17	12	3265	74	81	8	0
Y- PLANES	379	933	322	28	19	2945	60	73	7	0

REJECTED EVENTS ARE CLASSIFIED AS FOLLOWS

TYPE =	1	2	3	4	5	6	7	8	9	10
X- PLANES	110	389	173	12	26	1590	52	127	10	2745
Y- PLANES	337	1029	376	33	43	2566	38	142	15	605

NUMBER OF EVENTS IN ENERGY INTERVALS

LESS THAN 200MEV = 1325 200MEV TO 700MEV = 2206
700MEV TO 1GEV = 297 1GEV TO 2GEV = 473
2GEV TO 3GEV = 237 3GEV TO 6GEV = 199
GREATER THAN 6GEV = 48

Figure 4.3 An example of the event summaries produced by the calibration program.

geomagnetic, geodetic, celestial or galactic frames of reference. Prior to the transformation, the three magnetometer numbers were converted into field values in gamma (1 gamma = 10^{-5} gauss) using functions representing the calibration of each of the three magnetometer heads. In the 1975 flights, in particular, the magnetometer encoding suffered from spark noise pick-up, thus the field values of each event were checked for possible errors. First of all, the field values of each event were compared with those of the previous event. If the horizontal or vertical field components differed by more than 1500γ, then the current field values were ignored and those of the previous event were used (up to a maximum of 10 events). The total field measured by the magnetometer was then compared with the value calculated from the IGRF model. If the total fields differed by more than 1500 gamma, then that event's magnetometer field values were replaced with those of the previous event which had satisfied this condition. The substitution of field values introduced a negligible error into the photon's position of origin because the rate of rotation of the detector was slow compared with the high event rate (> 2/sec for the 1975 flights).

The first transformation was into geomagnetic coordinates :

$$\begin{pmatrix} CX1 \\ CY1 \\ CZ1 \end{pmatrix} = \begin{pmatrix} \cos\delta & \sin\delta & 0 \\ -\sin\delta & \cos\delta & 0 \\ 0 & 0 & 1 \end{pmatrix} \begin{pmatrix} CX \\ CY \\ CZ \end{pmatrix}$$

where δ is the angle between the x-axis of the spark chamber and the horizontal field vector (magnetic north), which was determined from the magnetic field values measured by the magnetometer and the known orientation of the spark chamber relative to the magnetometer axes.

The second transformation was into geodetic coordinates, using the magnetic declination ψ which was computed from the IGRF (of course, the field values calculated from the IGRF model depended on the geographic coordinates of the detector) :

$$\begin{pmatrix} CX2 \\ CY2 \\ CZ2 \end{pmatrix} = \begin{pmatrix} \cos\psi & \sin\psi & 0 \\ -\sin\psi & \cos\psi & 0 \\ 0 & 0 & 1 \end{pmatrix} \begin{pmatrix} CX1 \\ CY1 \\ CZ1 \end{pmatrix}$$

To transform into siderial coordinates the latitude and longitude of the detector were needed together with the local time of the event :

λ = the co-latitude (i.e. measured from the north pole) of the detector

ℓ = the longitude of the detector

T_l = the local time of the event

T_d = the time difference between the local time zone and GMT (= $9\frac{1}{2}$ hours or 570 mins for Alice Springs)

$T_u = T_l - T_d$ = the universal time of the event

T_σ = the time in minutes from the true (or autumnal) equinox

σ = the angle in radians to the true equinox

T_σ was calculated from the relation :

$$T_\sigma = T_u + (N \times 24 + T_u/60) \times 9.8296/60 \text{ minutes}$$

where N is the number of days from the true equinox and 9.8296 is the

difference in seconds between a solar and sidereal hour. The time in minutes, T_σ, was converted into an angle in radians, σ, by the following expression :

$$\sigma = (\frac{T_\sigma \times 15}{60} + \ell)/57.296$$

where 57.296 is the conversion factor for degrees to radians. The direction cosines of the event in sidereal coordinates are then given by :

$$\begin{pmatrix} CX3 \\ CY3 \\ CZ3 \end{pmatrix} = \begin{pmatrix} 1 & 0 & 0 \\ 0 & \cos\sigma & \sin\sigma \\ 0 & -\sin\sigma & \cos\sigma \end{pmatrix} \begin{pmatrix} \cos\lambda & 0 & \sin\lambda \\ 0 & 1 & 0 \\ -\sin\lambda & 0 & \cos\lambda \end{pmatrix} \begin{pmatrix} CX2 \\ CY2 \\ CZ2 \end{pmatrix}$$

The transformation into the galactic frame was performed by a two-fold rotation in which α_N and δ_N defined the position of the galactic north pole on the celestial sphere and a further rotation through γ degrees about the x-axis pointed the z-axis towards the galactic centre (see Figure 4.4).

According to the IAU system of galactic coordinates (1959),

$$\alpha_N = 192.25°$$
$$\delta_N = 27.4°$$
$$\gamma = 57.0°$$

and therefore

$$\begin{pmatrix} CX4 \\ CY4 \\ CZ4 \end{pmatrix} = \begin{pmatrix} 1 & 0 & 0 \\ 0 & \cos\gamma & \sin\gamma \\ 0 & -\sin\gamma & \cos\gamma \end{pmatrix} \begin{pmatrix} \sin\delta_N & 0 & \cos\delta_N \\ 0 & 1 & 0 \\ -\cos\delta_N & 0 & \sin\delta_N \end{pmatrix} \begin{pmatrix} 1 & 0 & 0 \\ 0 & \cos\alpha_N & \sin\alpha_N \\ 0 & -\sin\alpha_N & \cos\alpha_N \end{pmatrix} \begin{pmatrix} CX3 \\ CY3 \\ CZ3 \end{pmatrix}$$

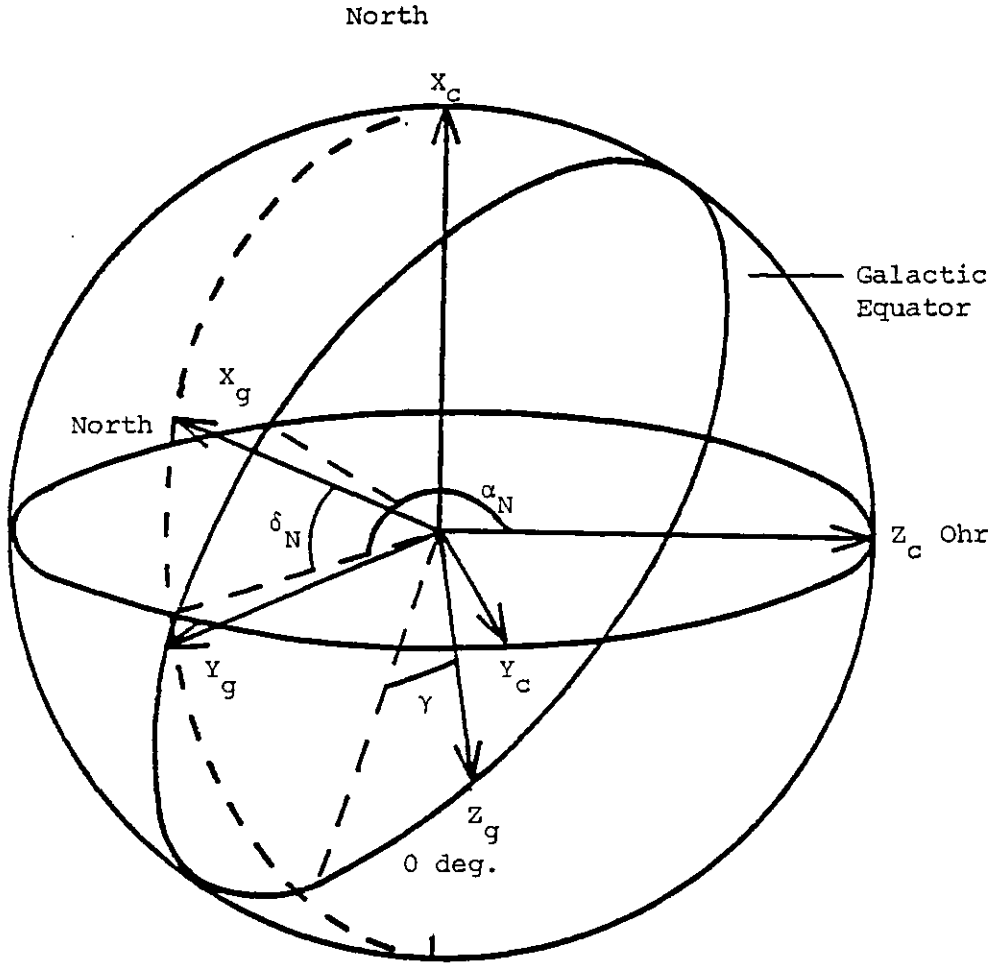

Figure 4.4 Projection of Galactic coordinate system on the celestial sphere, showing transformation angles.

(The transformations were checked by inserting values of CX, CY, CZ for the Sun derived from magnetometer readings when the solar sensor was triggered.)

From the direction cosines, the galactic coordinates of the event were found. The event was then placed in the appropriate bin on the galactic sphere, the galactic sphere having been split up into bins 2° wide in longitude and of such a width in latitude as to give bins of the same solid angle as a 2° x 2° bin on the galactic equator. For the flight analysis, the event was then written to magnetic tape in the format : event number, bin coordinates, scintillator pulse height and energy in MeV.

In a similar fashion to the calibration program, the flight program could be used to analyse any stretch of data. Scintillator pulse height and energy cut-offs could also be introduced. The program produced a skymap showing the distribution of events across the galactic sphere. Sample events were also outputted, together with a summary showing the number of accepted and rejected events. In addition, the bins were combined into latitude and then longitude strips and the number of events in each strip was shown.

4.3.4 The Exposure Program

The exposure to each of the 2° x 2° bins was calculated in this program. During the course of a flight, the vertical axis (pointing direction) of the detector traced a path across the sky. This path was known in geographic coordinates from the flight record (see section 2.7.2). The trajectory of the detector across the galactic (or celestial) sphere was found by transforming the pointing direction into the galactic (celestial) frame of reference. The transformation was performed as described in the previous section, with the pointing direction

initially defined by the direction cosines CX = 0, CY = 0, CZ = 1 for a vertically pointing detector.

Each bin of the galactic sphere was scanned every $2\frac{1}{2}$ minutes to see whether it was within the field of view of the detector. This was done by calculating the angle between the pointing direction of the detector and the bin, from the product of the respective direction cosines. If the angle was less than the opening angle of the telescope, then this meant that the bin was visible to the telescope. The area of detector presented to the bin was evaluated using the expression below :

$$\text{Area} = A(\theta) \cos\theta,$$

where $$A(\theta) = \{ 2R^2 \cos^{-1}\left(\frac{L \tan\theta}{2R}\right) - L \tan\theta \left(R^2 - \frac{L^2 \tan^2\theta}{4}\right)^{\frac{1}{2}} \}$$

and L = effective length of the telescope (cm)

R = radius of the converter (scintillator)

θ = angle between detector pointing direction and bin

The expression for the overlap area $A(\theta)$ comes from simple geometry (see Figure 4.5 which represents the telescope elements as seen by a photon incident at an angle θ. The overlap area is the shaded region).

To digress, the geometric factor (or area-solid angle factor) of the detector was also derived using the overlap area function $A(\theta)$ since

$$\text{Area-solid angle} = 2\pi \int_0^{35} A(\theta) \cos\theta \sin\theta \, d\theta = 2\pi \int_0^{35} A(\theta) \frac{\sin 2\theta}{2} d\theta,$$

where the integration is over the opening angle of the detector. The geometric factor for the two units in 1975 was $\sim$ 400 cm^2 ster., which was

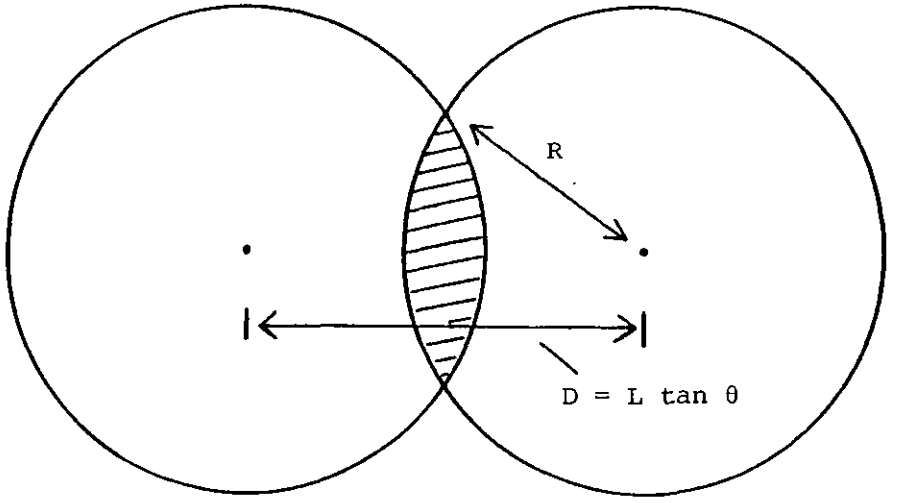

Figure 4.5 Overlap area.

Telescope elements as seen by a photon incident at an angle θ. The shaded region is the overlap area.

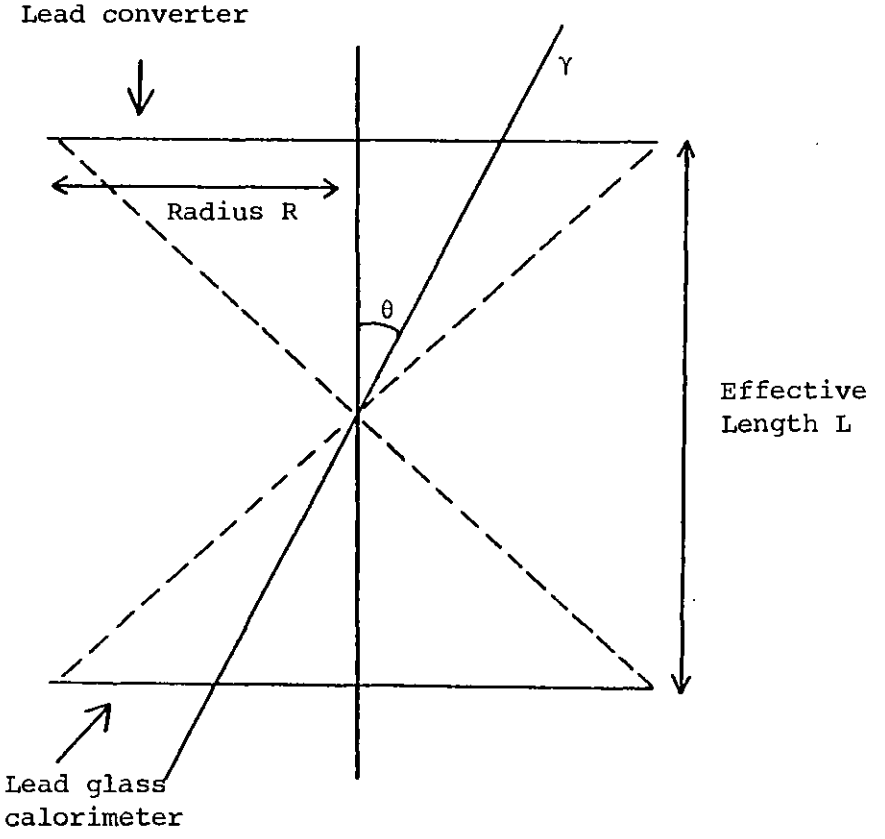

calculated using numerical integration.

The product of the overlap area and the time interval ($2\frac{1}{2}$ minutes) gives the exposure. However, the exposure value was reduced in practice by various efficiency factors, which were described in Chapter 3. These were the converter efficiency as a function of zenith angle (see section 3.3.1), the spark chamber efficiency as a function of angle (see section 3.2.1), the radial efficiency of the instrument (see section 3.8), the spark chamber efficiency as a function of energy (see section 3.2.1) and the spark chamber efficiency as a function of local time (see section 3.2.1). There were two additional time-dependent efficiencies, which were incorporated in the computer program as data arrays. These were the transcription efficiency and the dead time correction.

The transcription efficiency accounted for data lost due to telemetry noise, time spent changing magnetic tapes during the recording and tape noise (or drop out). Data was also lost whilst reading into the computer (see section 4.3.1). The transcription efficiency factor was typically 0.97.

The time required to clock out and transmit each event (which consisted of 282 bits) was 206 ms. This was also the instrumental dead time because the coincidence telescope was disabled whilst data was transmitted over the telemetry. If the events were transmitted at a rate of y_o per second, the telescope was therefore dead for y_o x 0.206 sec. Hence y_o events were really observed in (1.0-y_o x 0.206) sec. i.e. the true rate of events was

$$y_T = \frac{y_o}{1.0-0.206\ y_o} \text{ / sec.}$$

The dead time correction was y_o/y_T; it averaged about 0.5 for both 1975 flights.

Using these efficiency factors, the exposure for each 2° x 2° bin

was evaluated for the whole flight (or for any time interval specified in the computer program). The exposure values were stored in an array, which was subsequently written to magnetic tape. The program produced a table of values, showing the trajectory of the balloon in galactic coordinates. It also printed an exposure map and a smoothed exposure contour map for a convenient display (see Figure 4.6). In addition, the exposure could be summed along latitude and longitude strips.

4.3.5 The Flux Program

In this program, the division of the counts by the exposure was performed for each bin to give a flux in units of counts/2° x 2° bin/cm^2/min. (The program took its input data from the output tapes of the flight and exposure programs.) The results were presented in the form of flux maps and histograms. Also, the bins were summed into latitude and then longitude strips of 2° width and, from the number of counts and the total exposure, the average flux of each strip was determined. The strips were then combined into bands, whose width depended on the angular resolution in the energy range under consideration. The average flux of each band was outputted, so that any anisotropy along the galactic plane would be immediately apparent (see section 5.2).

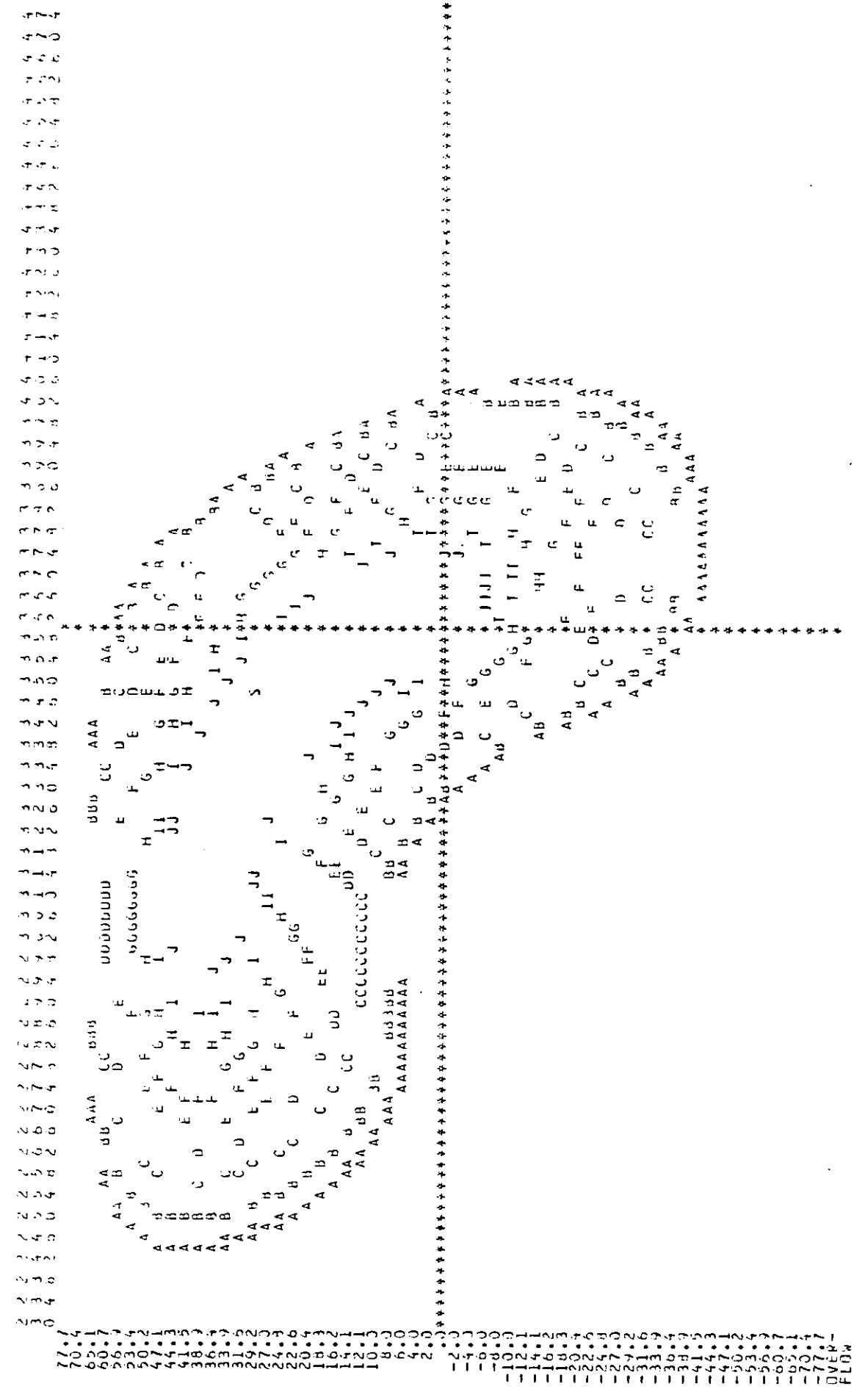

Figure 4.6 Smoothed exposure contour map for flight I 1975.

CHAPTER V

RESULTS

5.1 Atmospheric Flux Measurements

Gamma rays coming from the Galaxy had to be observed against a background of atmospheric gammas produced by cosmic-ray interactions in the atmosphere. If gamma-rays of galactic origin are to stand out, then the background should be isotropic. It is therefore necessary to examine possible causes of non-uniformity in the background flux which could simulate flux variations across the Galaxy after transformation into Galactic coordinates.

5.1.1 East-West Effect

Cosmic rays must have a minimum energy in order to overcome the Earth's magnetic field and enter the atmosphere. This minimum energy, or cut-off rigidity, is a function of azimuth for a given point on the Earth. The rigidity is a minimum in the western sky and a maximum in the east for positively charged particles (vice versa for negatively charged particles). Thus cosmic rays, which are predominantly protons, will arrive in greater abundance from the west, giving rise to an asymmetric intensity distribution relative to the magnetic north-south plane. Because atmospheric gamma-rays are the secondary products of cosmic rays, a similar asymmetry should appear in the gamma distribution.

The east-west effect was studied experimentally by stopping the transformations in the 'flight' and 'exposure' computer programs (see

sections 4.3.3 and 4.3.4) after the arrival directions had been transformed into geomagnetic coordinates. Data from the various flights was combined and is shown in Table 5.1 for two energy bands : $0.5 < E_\gamma < 1.0$ GeV, which may be compared directly with a theoretical estimate made by Byerley (private communication), and $1.0 < E_\gamma < 2.5$ GeV. The difference between theory and observation in Table 5.1 is assumed to be due to scattering in the atmosphere, which is not accounted for in the theory.

The east-west bias was removed in galactic coordinates, by introducing simple numerical factors in the flight program that weighted the counts according to their arrival direction in the geomagnetic frame.

TABLE 5.1 EAST-WEST BIAS OF THE ATMOSPHERIC GAMMA RAY FLUX

	Geomagnetic WEST, ± 15° NS			Geomagnetic EAST, ± 15° NS		
	-25°	-15°	-5°	5°	15°	25°
Theoretical $0.5<E_\gamma<1.0$ GeV	1.22	1.09	1.00	0.93	0.89	
Experimental $0.5<E_\gamma<1.0$ GeV	1.12 ± .04	1.06 ± .03	1.00	0.94 ± .03	0.88 ± .04	
Experimental $1.0<E_\gamma<2.5$ GeV	1.10 ± .07	1.05 ± .04	1.00	0.95 ± .04	0.90 ± .07	

5.1.2 Latitude Effect

The cut-off rigidity is also a function of geomagnetic latitude. The rigidity increases with decreasing latitude. Thus, the primary cosmic ray flux, incident at the top of the atmosphere, will decrease as one proceeds from the poles to the equator. It follows that the intensities

of the various secondary components will also decrease with decreasing latitude. In particular, as the detector drifts in latitude, the atmospheric gamma flux will vary.

The latitude drift during the two 1975 flights is shown in Figure 5.1. Figure 5.2 shows the corresponding change in cosmic ray rate for the 1975 flights, normalised to a cosmic ray rate of unity at the latitude of Alice Springs Airport (-23°40', 8.8 GeV cut-off). The cosmic ray rates were calculated from the cut-off rigidities given by Quenby and Wenk (1962), which are shown in Table 5.2.

TABLE 5.2

Cut-off Rigidities

	130°	135°	140°	145°
-20°	10.6	10.9	11.1	11.1
-22½°	9.0	9.3	9.5	9.3
-25°	7.5	7.7	7.8	8.0
-27½°	6.0	6.2	6.4	6.7

Cosmic Ray Fluxes / cm^2 sec.ster (protons)

	130°	135°	140°	145°
-20°	.0170	.0163	.0158	.0158
-22½°	.0220	.0210	.0203	.0210
-25°	.0300	.0290	.0285	.0280
-27½°	.0400	.0385	.0370	.0350

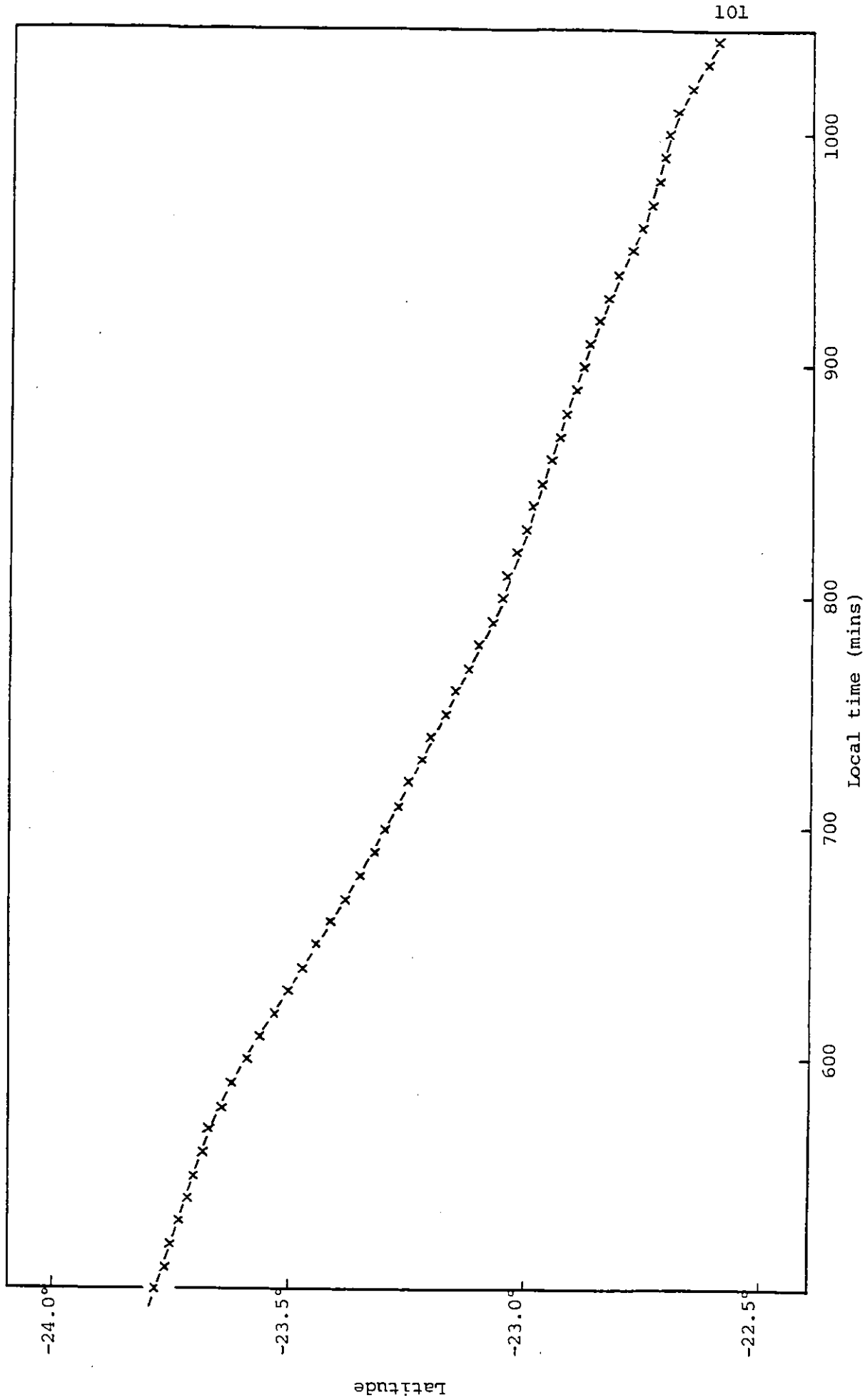

Figure 5.1a Latitude drift during flight I 1975.

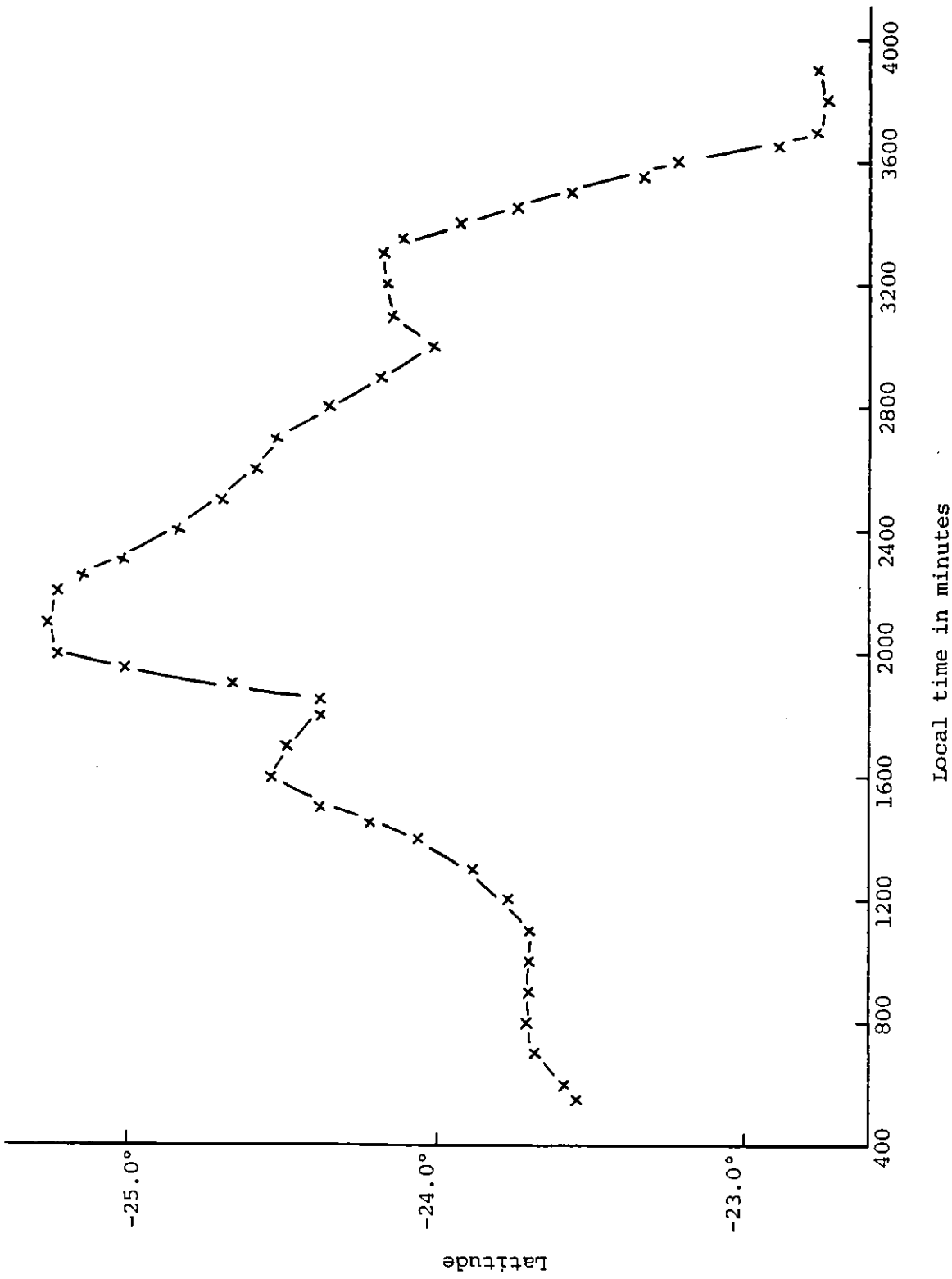

Figure 5.1b Latitude as a function of local time (Alice Springs) for the 1975 II flight.

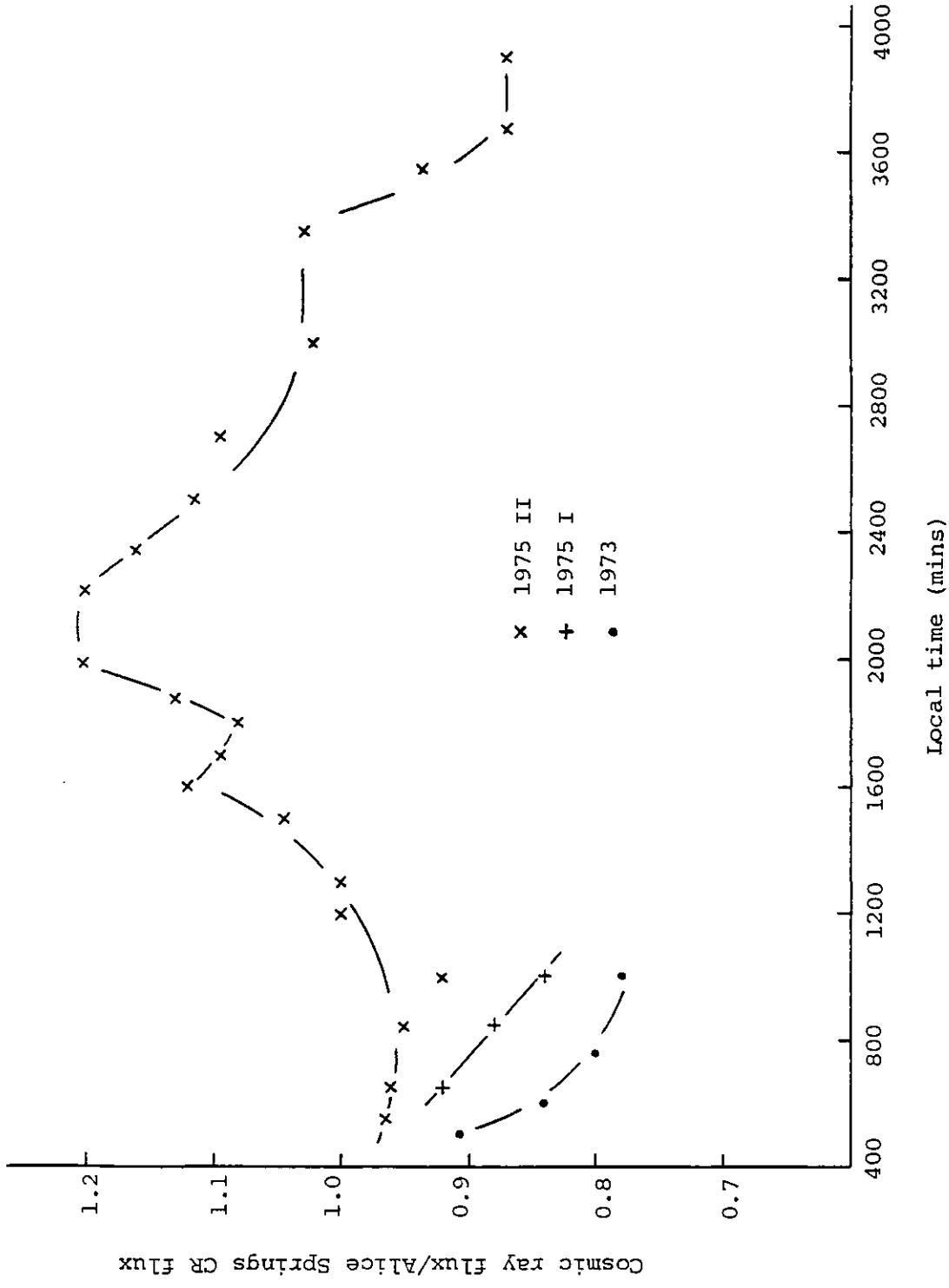

Figure 5.2 Predicted cosmic ray flux, normalised to a value of unity over Alice Springs, as a function of local time for the three flights.

5.1.3 Atmospheric Gamma-Ray Production

Atmospheric gamma rays are produced by the interaction of cosmic rays with air molecules at the top of the atmosphere, and one would expect the gamma flux in the downward vertical direction to increase almost linearly with depth in the upper atmosphere. To check this, measurements on atmospheric gammas were performed.

The calibration and exposure computer programs (see sections 4.3.2 and 4.3.4) were used to analyse sections of ascent and float data obtained in 1973 and 1975 at various altitudes. (The variation in altitude as a function of local time for the three flights - 1973, 1975I, 1975II - is shown in Figure 5.3.) The calibration program produced histograms of pulse height distributions from scintillator C for different energy intervals. Using these distributions, single track events which represented, in general, non-gamma-ray background were removed by imposing a cut-off at a pulse height corresponding to 1.3 electrons (pulse height number 57 for flt '73, 64.5 for flt I '75, 73.5 for flt II '75). However, the separation of single from multiple tracks in scintillator C was not perfect i.e. spillage of single track events into the multiple track channels occurred. It turned out that 15% of the single track counts below 1.3 electrons had to be subtracted from the number of counts above 1.3 electrons to obtain the true number of multiple track counts.

The exposure program computed the corresponding exposure values using the area-solid angle factor of the telescope determined from the two parameters (effective length and radial efficiency) obtained by fitting the observed zenith distribution as described in section 3.8; and various efficiency factors. These factors, which were detailed in section 4.3.4, were : transcription efficiency; spark chamber efficiency as a function of time; spark chamber efficiency as a function of zenith

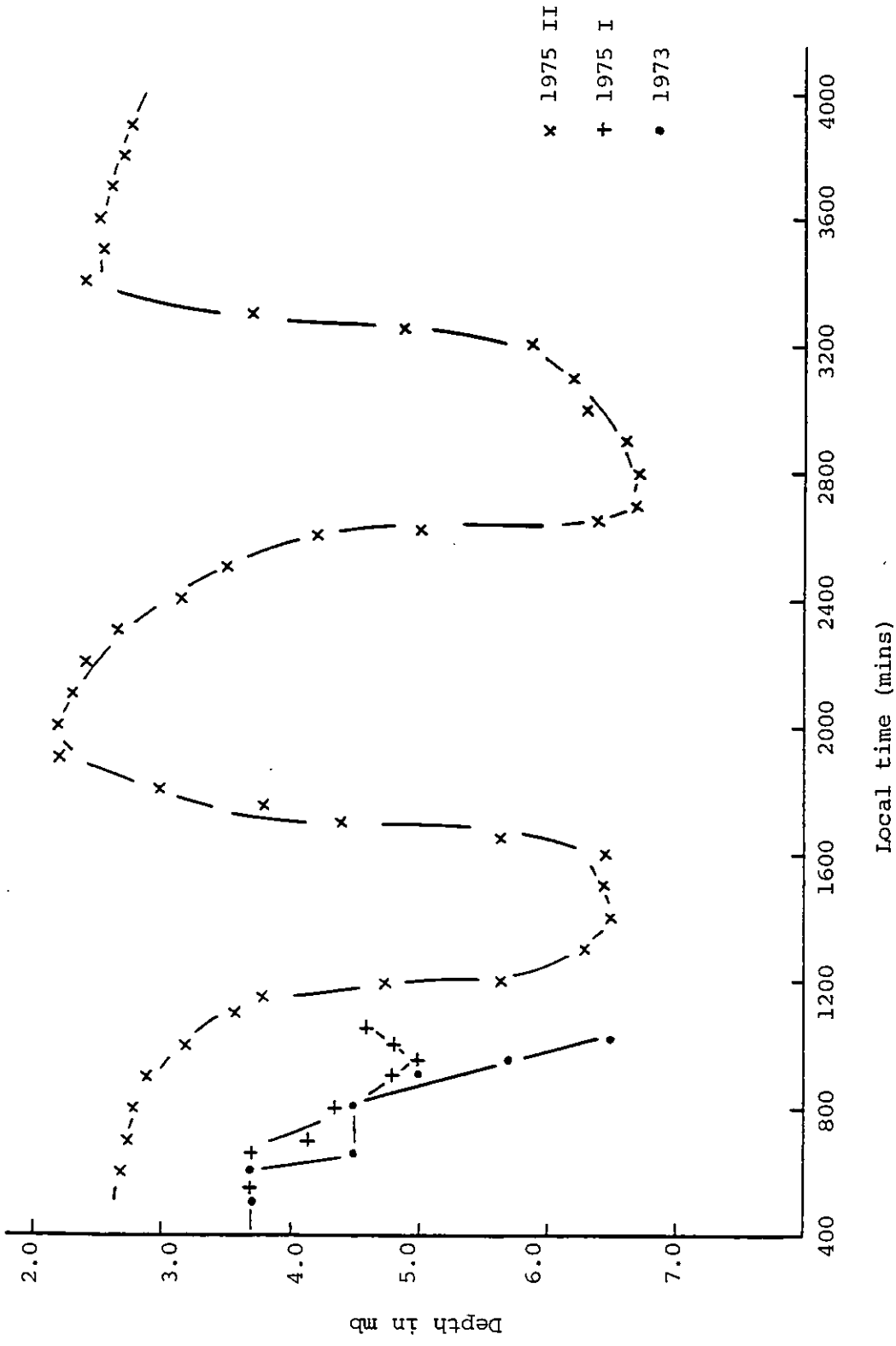

Figure 5.3 Altitude as a function of local time for the three flights.

angle and energy; dead time correction and converter efficiency as a function of angle.

The raw count rates, which were calculated for five different energy intervals, were converted into fluxes using the following formula :

$$I(E,t) = \frac{N_t \times g(E) \times 0.932 \times j(E)}{AT_t \times A \times 60 \times \left(\frac{2}{57.3}\right)^2 \times \varepsilon(E)} \text{ photons } (cm^2 \text{ sec.ster})^{-1} \quad (5.1)$$

where N_t is the number of counts at depth t gm/cm^2 within a particular energy band E and AT_t is the corresponding exposure in units of (cm^2 min. per cm^2 of the detector per 2° x 2° bin). $\varepsilon(E)$ is the conversion efficiency (see section 3.3.1), $(2/57.3)^2$ converts 2° x 2° into steradians and A is the detector area ($\approx$ 1140 cm^2). g(E) is a correction factor for the energy resolution of the lead glass calorimeter (see section 3.6.3). Due to the finite energy resolution and the form of the gamma spectrum (monotonically decreasing) there was a net transfer of counts from the lower to the higher energy bins. This produced an over-estimate in the count-rate of typically 7% in the 300-600 MeV range and 6% at higher energies.

A factor of 0.932 was required to obtain the vertical flux from that actually measured by the detector, which amounted to a flux integrated over $\theta = \pm 30°$, the opening angle of the telescope. The correction assumes a sec θ dependence for the atmospheric gamma flux.

A scintillator cut-off, equivalent to 1.3 electrons, was introduced to remove noise events, as mentioned previously. However the improvement in the signal-to-noise ratio was at the expense of a slight drop in efficiency, because those single tracks arising from genuine gamma events would also be rejected. The term j(E) in the above formula represents this loss in efficiency, which was known from

DESY beam tests (see section 3.7 and Table 3.4).

The primary cosmic ray flux, and therefore the gamma flux, is a function of the solar cycle. Since both the 1973 and 1975 flights occurred near solar minimum, no correction has been applied for this variation.

Results from the three flights are shown in Figures 5.4a) - e) for five different energy ranges. The fluxes have been plotted against the product of depth (mb) and the predicted cosmic ray rate (CR), to allow for variations in geomagnetic cut-off with altitude and latitude (see section 5.1.2). The fluxes have been corrected for atmospheric attenuation of the primary cosmic ray flux and the secondary gamma flux, since attenuation would otherwise result in a non-linear increase of gamma flux with depth. (To illustrate the effect of attenuation, the flux at 10 mb is about 10% less than 10 times the flux at 1 mb.) The horizontal axis has been extended to -0.5 mb x CR, because the material above the detector, namely the wall of the pressure vessel and the thermal insulation, was a source of secondary gamma radiation and was equivalent to about 0.5 gm/cm^2 of atmosphere.

If the detector was responding only to downward moving gamma rays which are predominantly cosmic ray secondaries, then an extrapolation to the top of the atmosphere of flux measurements taken at various depths should converge to zero.

Between 0.7 and 2 GeV (Figures 5.4b,c) the flux does indeed extrapolate to zero at zero depth, the residual flux being negligible in comparison with errors in the extrapolation. There is good agreement between results obtained in 1973 and 1975 with unit I and also between results obtained with unit I and unit II. The scatter on the points, which exceeds that predicted by statistics by a small amount, is probably due to uncertainties in altitude (particularly in 1973, when

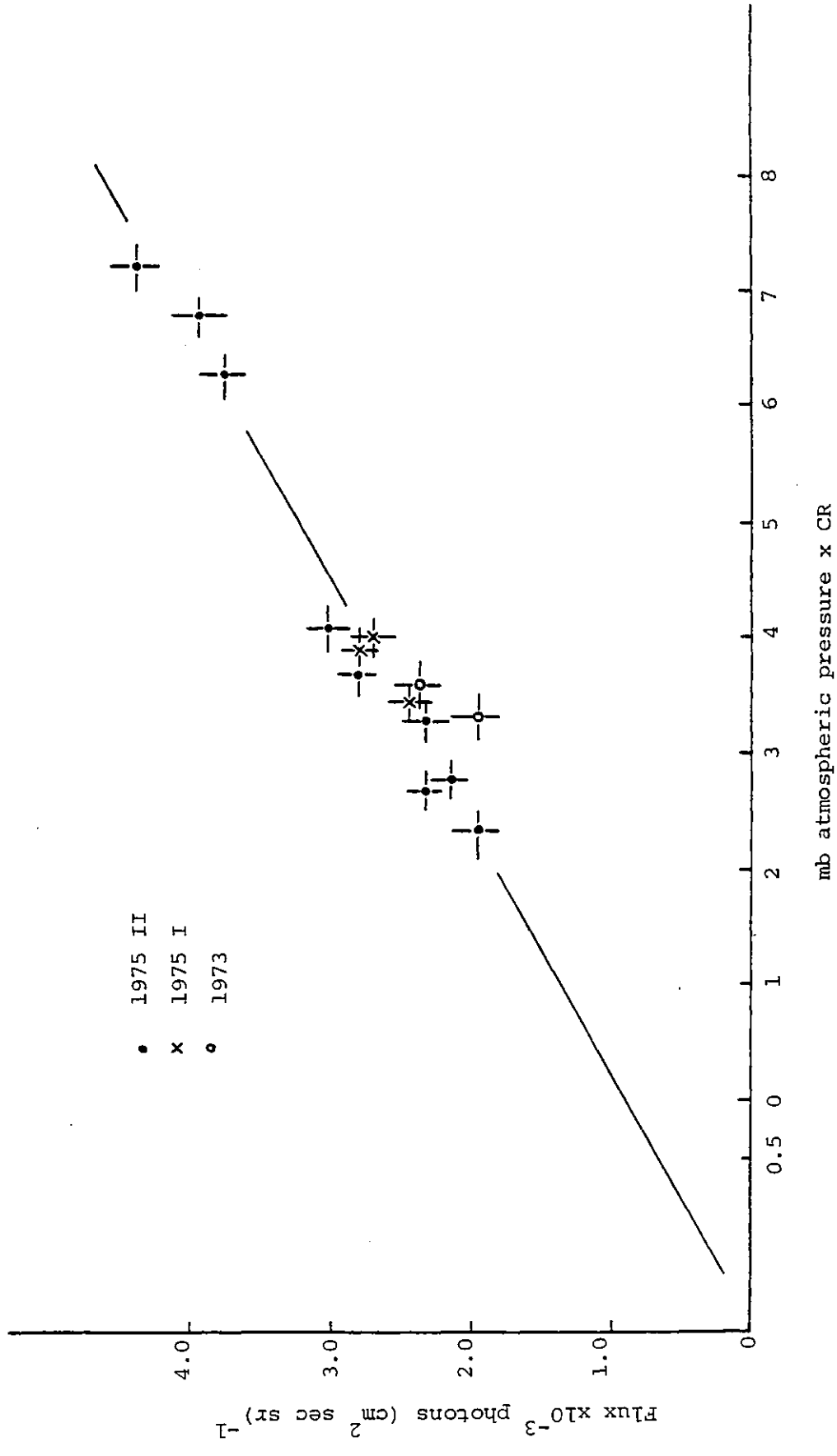

Figure 5.4a Gamma-ray production/gm atmospheric depth in the energy range $0.2 < E < 0.7$ GeV.

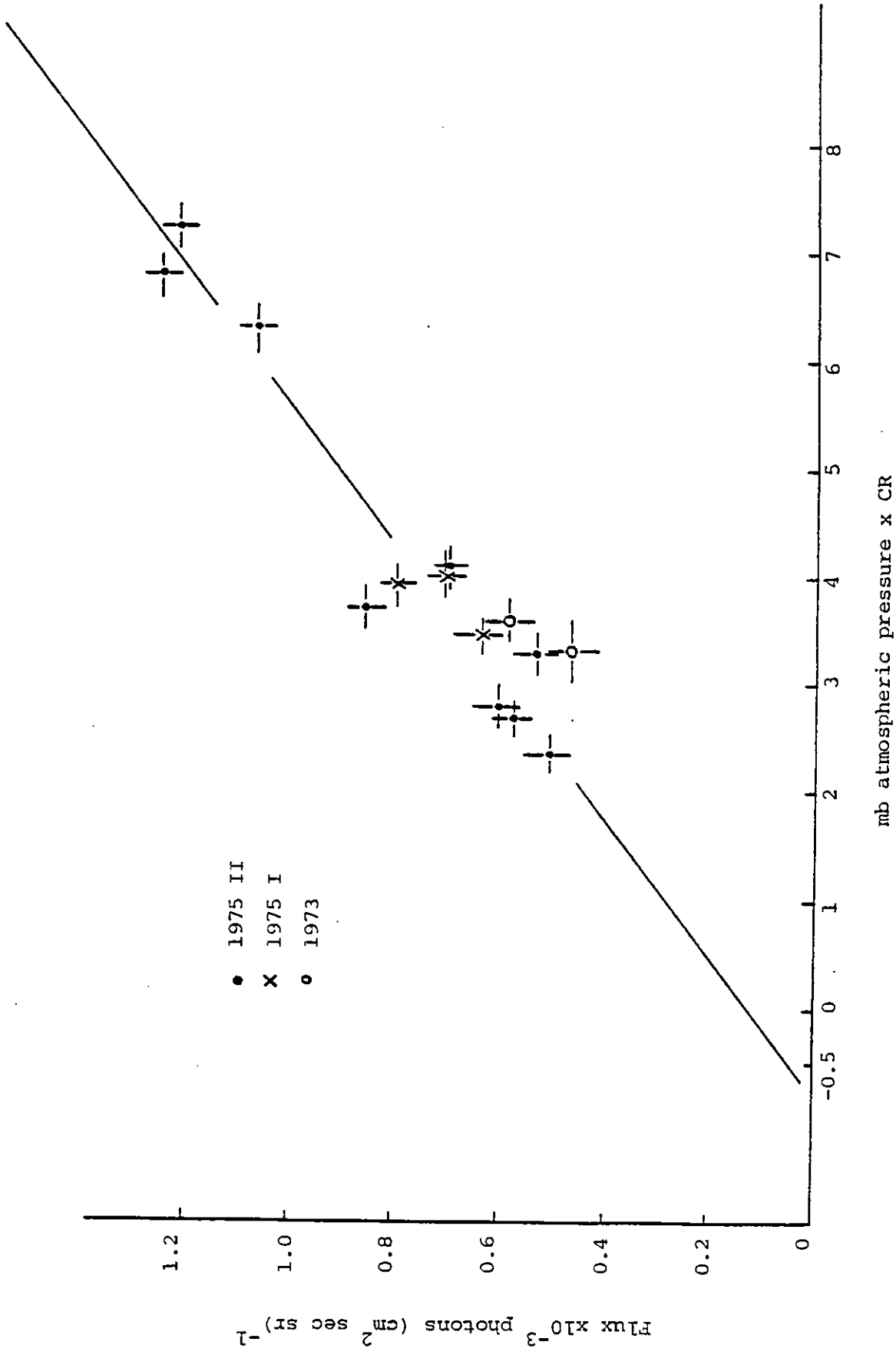

Figure 5.4b Gamma-ray production/gm atmospheric depth in the energy range 0.7 < E < 1.0 GeV.

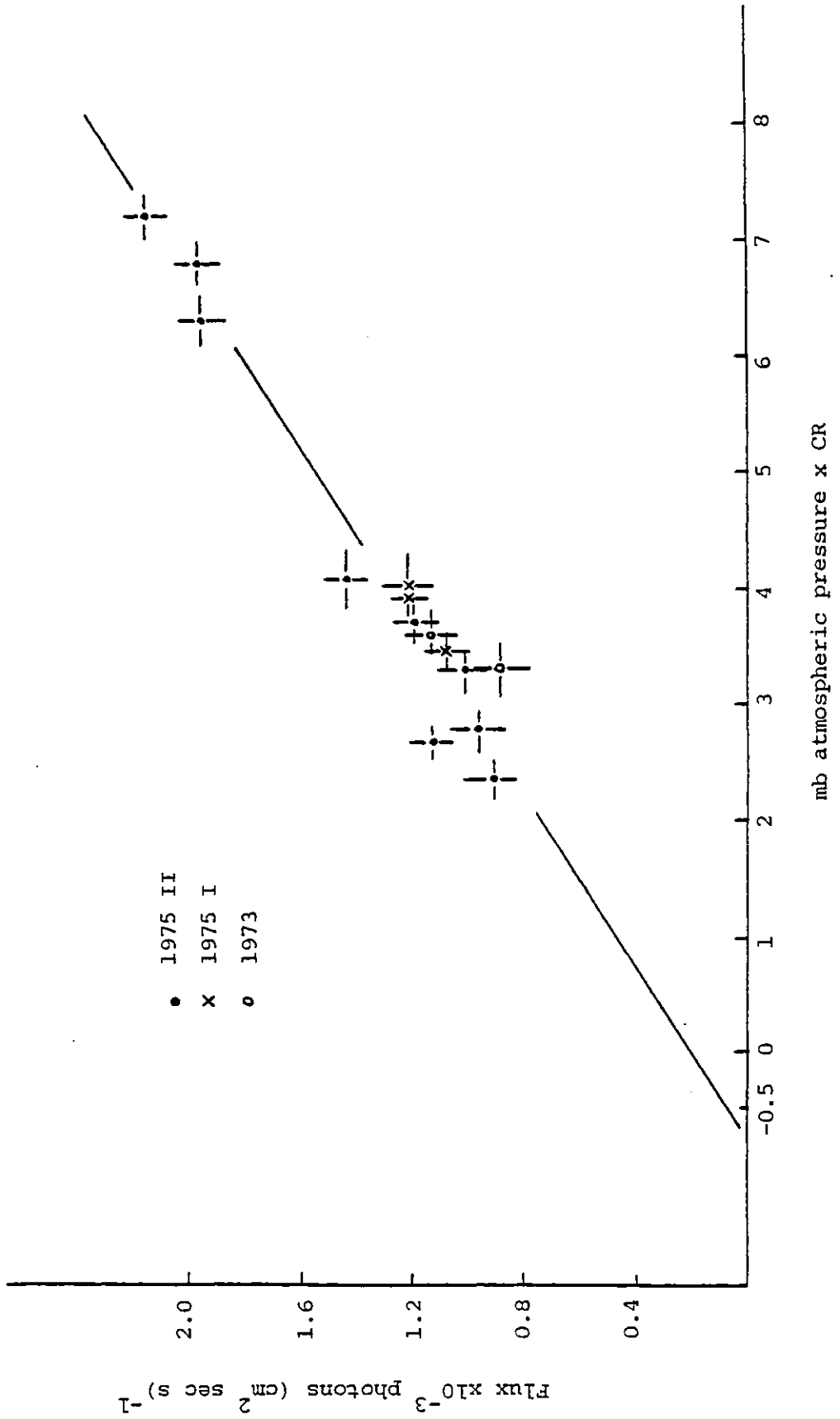

Figure 5.4c Gamma-ray production/gm atmospheric depth in the energy range 1.0 < E < 2.0 GeV.

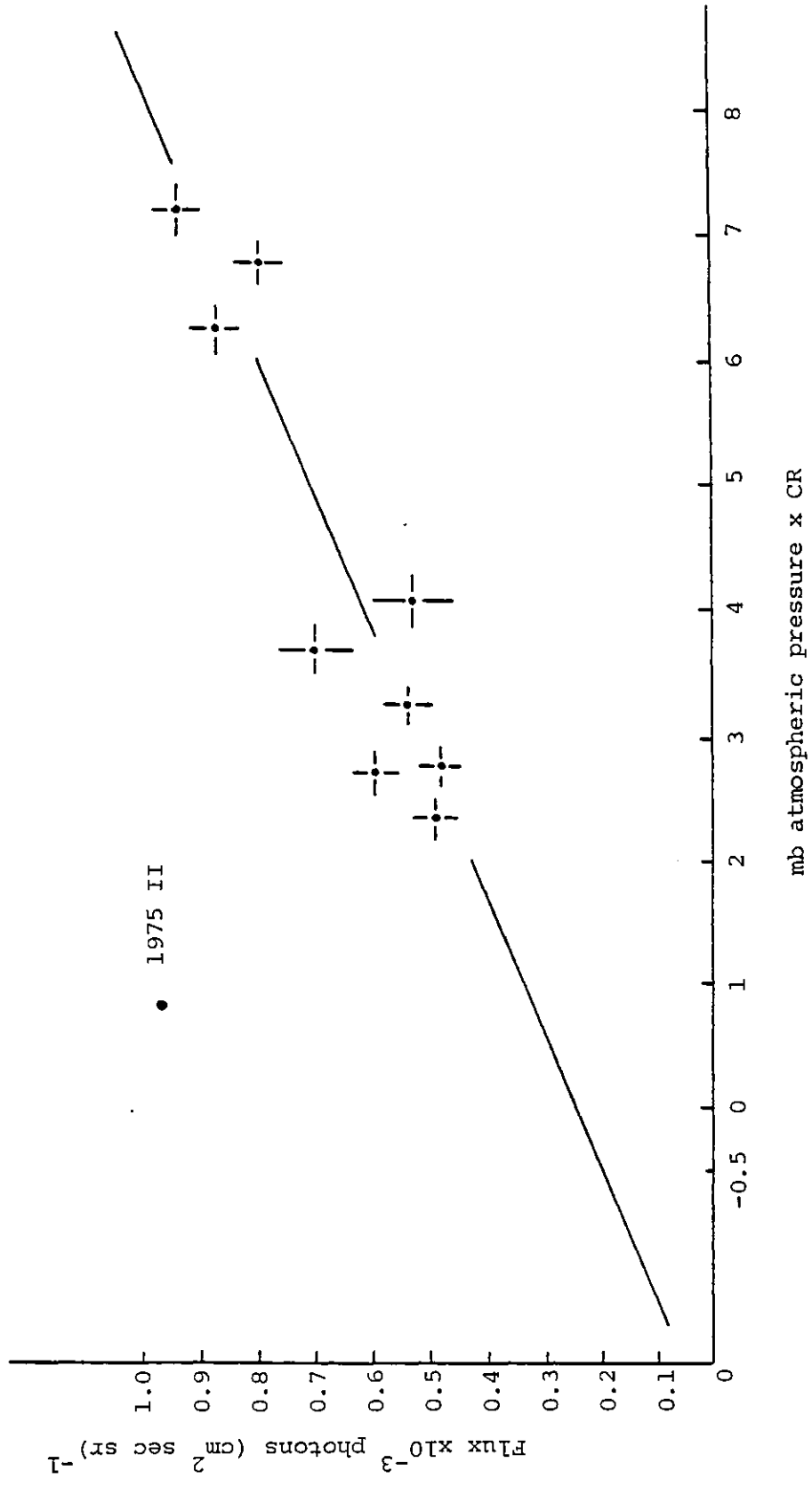

Figure 5.4d Gamma-ray production/gm atmospheric depth in the energy range 2.0 < E < 3.0 GeV.

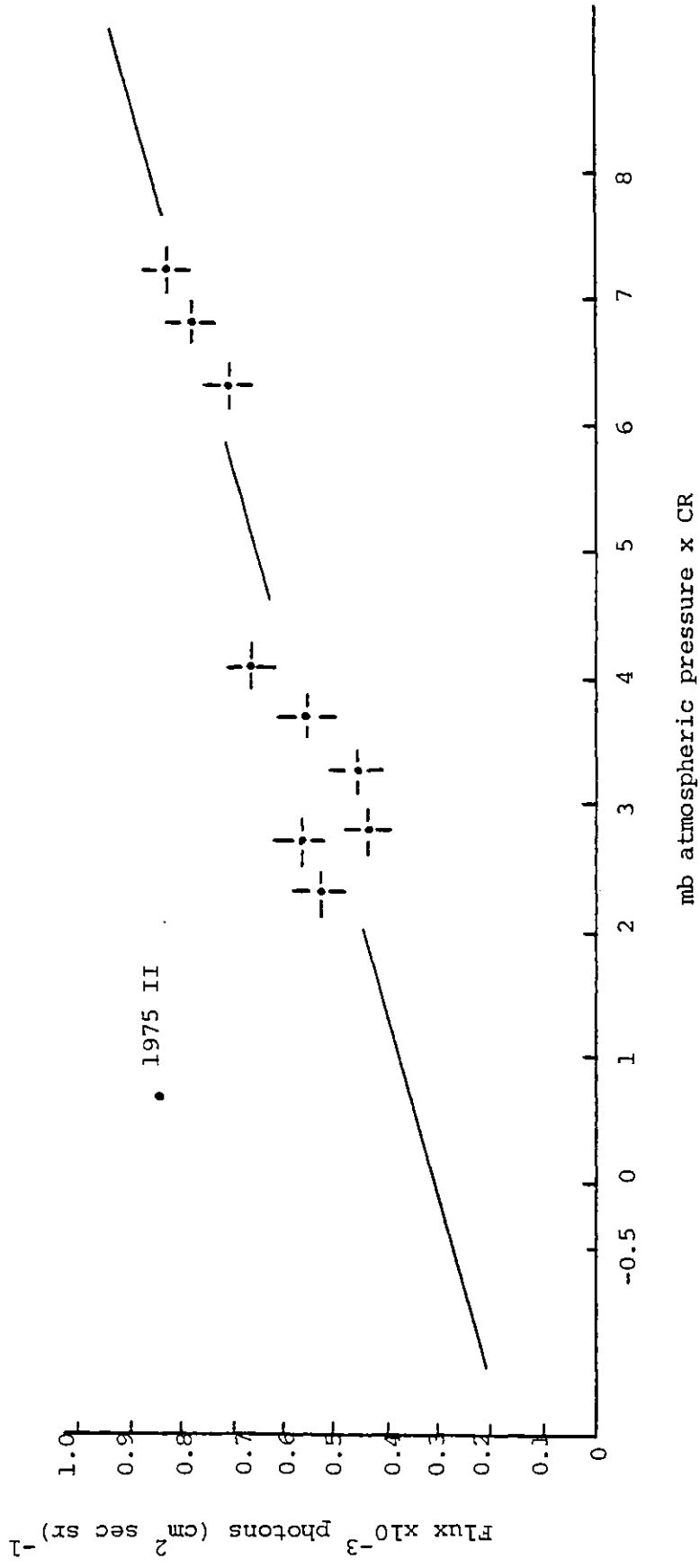

Figure 5.4e · Gamma-ray production/gm atmospheric depth in the energy range 3.0 < E < 5.0 GeV.

there was no independent radar check) or local deviations of the cut-off rigidity from the Quenby-Wenk value.

In the energy range 0.2-0.7 GeV, Figure 5.4a, the flux does not extrapolate to zero at zero depth. Results from the Time of Flight system installed for the 1977 and 1978 flights suggest that some of this excess is due to upward moving particles produced by low energy secondaries which have entered the calorimeter from the side and interacted there. This type of event would be, of course, removed by the TOF discriminator. The remaining excess could be due to side showers which leak through the anticoincidence shield, and to gamma rays incident at angles larger than the geometrical opening angle of the telescope. These could trigger the telescope if the electron pair were scattered downward into the spark chamber and entered scintillator C and the calorimeter. The flux of gamma rays at large zenith angles can be very high, because the effective atmospheric depth at these angles is large (the well-known sec θ dependence).

As the energy increases above 2 GeV, the residual flux at zero depth becomes progressively greater (see Figures 5.4d,e). Again, TOF results indicate that about half this excess is due to upward moving tracks. The remainder is thought to be due to cosmic rays leaking through the anti-coincidence shield and multiplying by interacting in the lead converter or the calorimeter in such a way as to make them acceptable to the scintillator C cut-off criterion. Such particles would deposit a lot of energy in the calorimeter as the geomagnetic cut-off at Alice Springs is 8.8 GeV, and would therefore be expected to contribute more to the upper than the lower energy channels. This hypothesis that part of the excess is due to cosmic ray leakage is supported by the observation that above 1 GeV the single track/multiple track ratio in scintillator C decreases as the depth increases, showing

that at least some single tracks are the result of cosmic ray primary leakage. This conclusion is further reinforced by the TOF results, which show that virtually all the single track events are produced by downward moving particles. (For a fuller description of the TOF results, which were used to support various arguments above, see Sood et al, 1982.)

In conclusion, it appears that the excess at zero depth in Figures 5.4a,d,e is due to a mixture of scattered gamma ray products, leaking cosmic ray primaries, and upward moving particles from primary interactions in the calorimeter. The slopes of the graphs give the gamma ray production rates/gm cm^{-2} as a function of energy. These have been plotted in Figure 5.5 where they are compared with a theoretical spectrum derived by Perola and Scarsi (1966) for π° decay photons, to which a contribution from bremsstrahlung (Beuermann, 1971) has been added. The agreement between the experimental results and the theoretical prediction is very good.

Figure 5.6 shows the same results normalised to 4.5 GeV cut-off and compared with the measurements of other experiments and the theory of Beuermann. The agreement here is less good but the difficulty of normalising fluxes between different rigidities and solar conditions may be the reason for this.

5.1.3.1 Anticoincidence Efficiency

It was argued in section 5.1.3 that part of the excess flux observed at zero depth in the high energy channels was due to cosmic ray leakage through the anticoincidence shield. This argument assumes that some of the leaking cosmic rays were subsequently misinterpreted as gamma-rays. A misinterpretation could have arisen if the cosmic rays interacted in the lead converter and produced downward moving

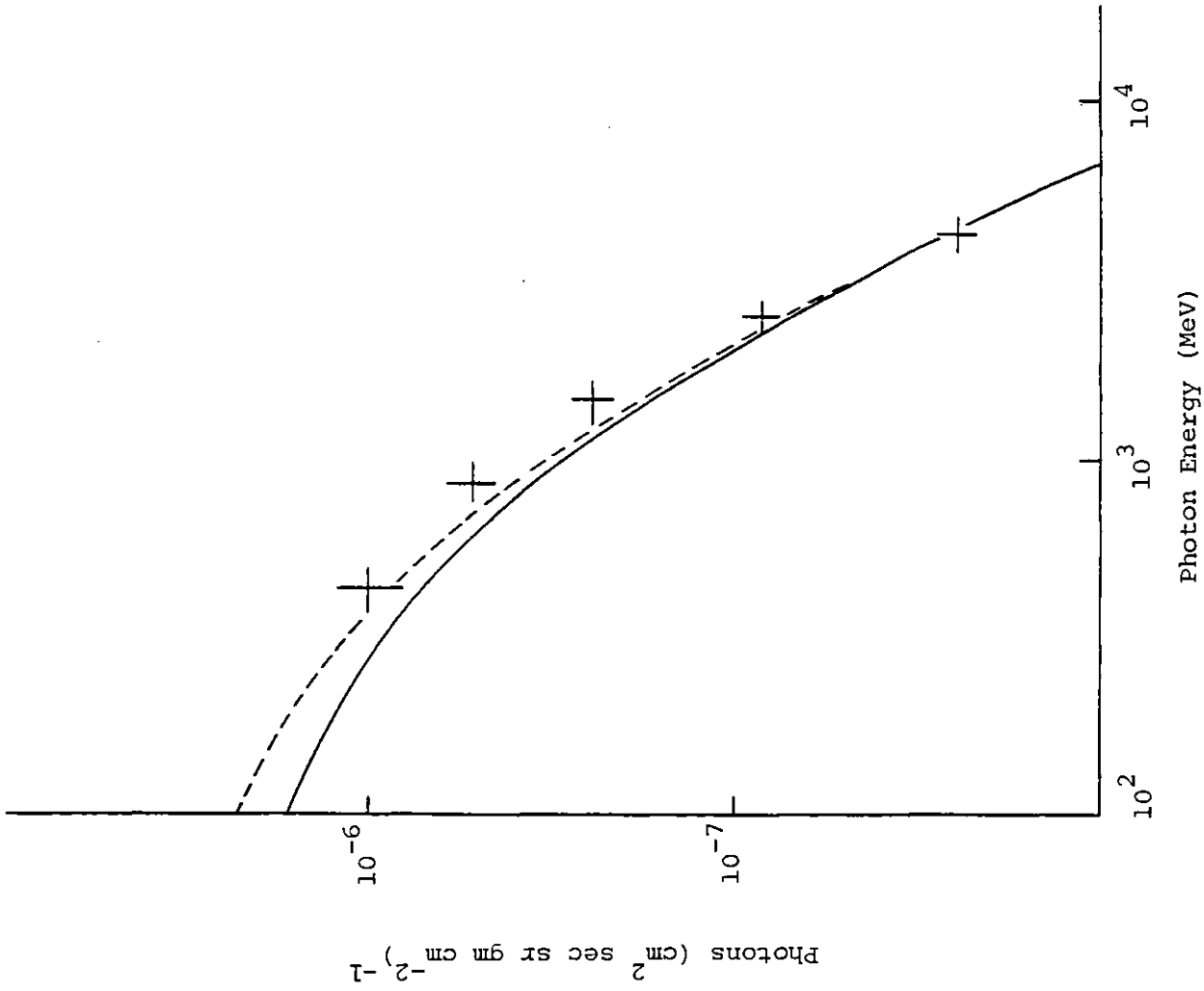

Figure 5.5 Atmospheric gamma-ray spectrum at 8.8 GeV cut-off rigidity compared with the π° decay theory of Perola and Scarsi together with a contribution from bremsstrahlung.

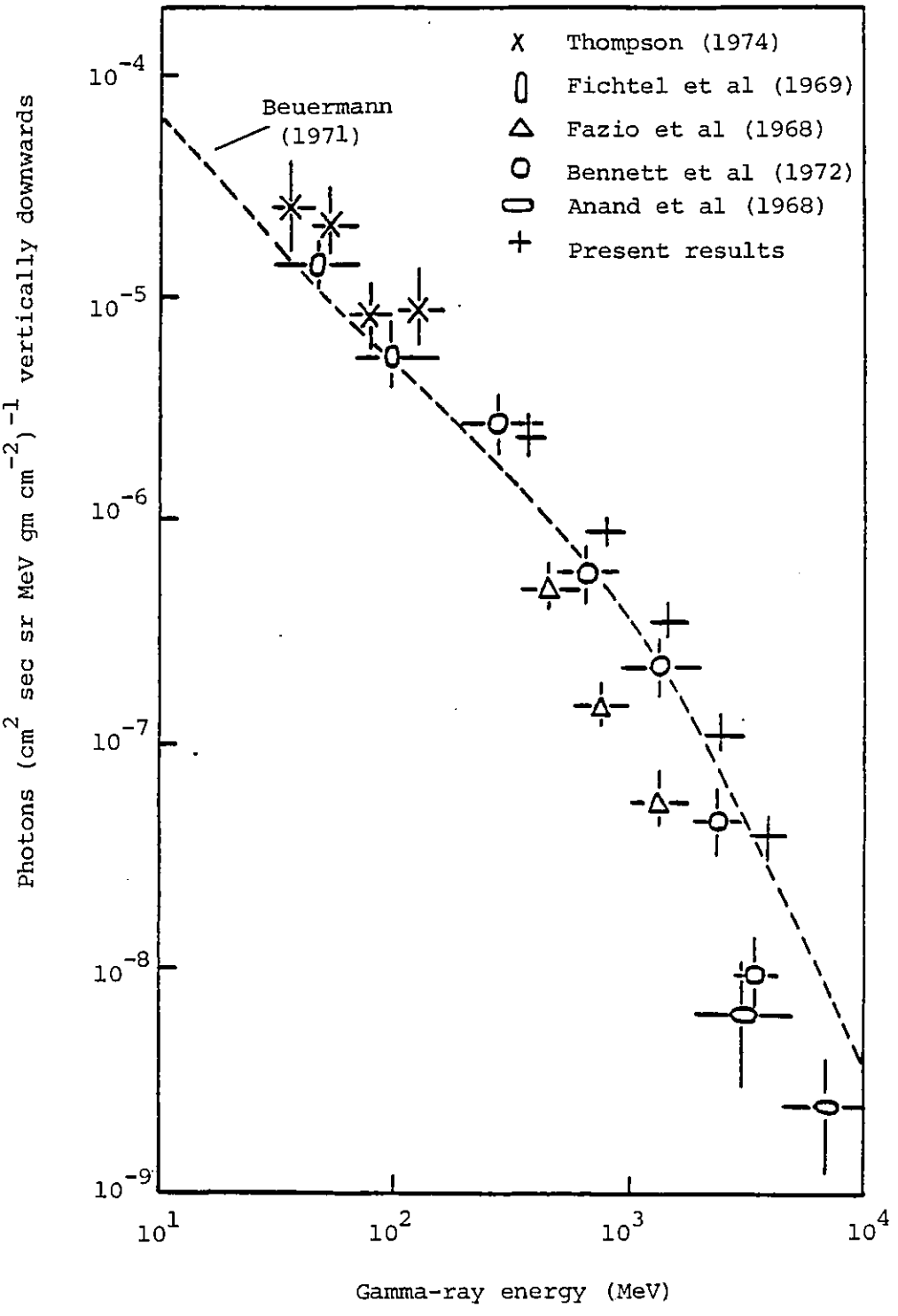

Figure 5.6 Comparison of the atmospheric spectrum measured by various experiments, normalised to 4.5 GeV cut-off, 1 gm/cm^2 depth and solar minimum conditions.

secondaries (of which at least two interacted in scintillator C), or if they interacted in the calorimeter in such a way as to produce back-scattered products which entered scintillator C.

The theory above can be tested by comparing the observed excess gamma flux with that predicted from the known incident cosmic ray flux, given the anticoincidence efficiency and the interaction probabilities in the converter and calorimeter.

The incident cosmic ray flux at 2.7 gm depth and 8.8 GeV cut-off is 0.03 p/cm^2 sec ster (Ormes and Webber, 1964). This includes a contribution of .0027 p/cm^2 sec ster from cosmic ray secondaries which, if incident in showers, could give rise to two or more tracks in the spark chamber thereby satisfying the scintillator cut-off criterion. (Of course the event would have to satisfy the 'apex' condition in the converter which would require in practice that the tracks were sufficiently close together that it would appear to the computer as if they had originated from the same area in the converter.) It should be mentioned that a flux of 0.03 p/cm^2 sec ster is equivalent to a count rate of 750 cts/min, taking the geometric factor of the detector as 400 cm^2 ster, which is much smaller than the observed rate (see section 2.6) which was 2200 cts/min for flight II 1975, but the difference is no doubt due to upward moving events arising from cosmic ray interactions in the calorimeter.

The anticoincidence efficiency was measured using ground level mu-mesons and was found to exceed 97% (see section 2.3.3). This corresponds to a flux of leaking cosmic rays of approximately $0.03 \times 0.03 = 0.9 \times 10^{-3}$ p/cm^2 sec ster.

The interaction length of a cosmic ray proton in lead is 190 gm cm^{-2}. Thus the probability of a cosmic ray interacting in the lead converter, which was half a radiation length thick (2.96 gm cm^{-2}) is

2.96/190 ≈ 2%. On the other hand, the probability of a cosmic ray interacting in the lead glass calorimeter which was 7 radiation lengths deep (24.5 cm) is 24.5 x 3.6/137 ≈ 64%, where 3.6 gm cm^{-3} is the density of lead glass and 137 gm cm^{-2} is the interaction length in lead glass. The probability of an interaction in the calorimeter producing a back-scattered soft charged component is difficult to compute theoretically, however it can be estimated given that the observed excess above 2 GeV was 2 x 10^{-4} p/cm^2 sec ster, of which about half was thought to be due to cosmic ray leakage (see section 5.1.3). Thus, if P_b is the probability of an interaction in the calorimeter producing back-scattered particles, then

$$0.03 \times 0.03 \times (0.02 + 0.64 \times 0.98 \times P_b) = 10^{-4}$$

i.e. $$P_b = 0.147$$

Thus P_b ≈ 15% under the assumption that cosmic ray leakage contributed about half the excess at zero depth.

5.1.4 Depth Curves

The depth curves for atmospheric gamma rays in the five different energy intervals are shown in Figures 5.7a)-e). There is close agreement between data from all the flights with the exception of flux measurements taken in 1973 at the highest altitude. It is possible that the altitude measurement was in error : there was no radar check in 1973 as there was in 1975. Alternatively, the cosmic ray flux may have been overestimated. The detector drifted well to the North East of Longreach (the launch site in 1973) and there is no theoretical estimate of the flux in this region.

It can be seen that the depth curves all rise to the Pfotzer maximum at 100 gm cm^{-2} and then fall off beyond this.

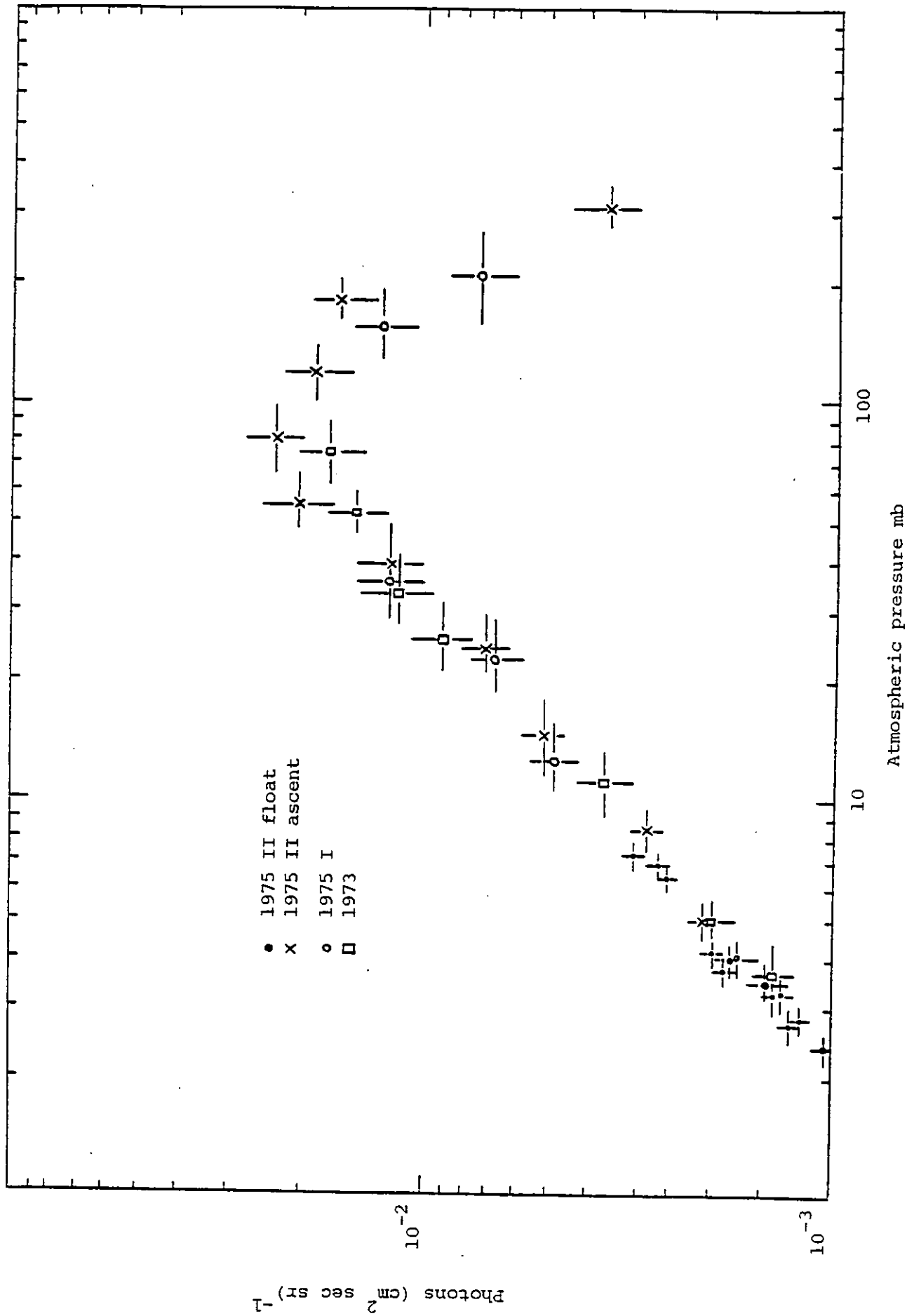

Figure 5.7a Depth curve for atmospheric gamma-rays in the energy range $0.2 < E < 0.7$ GeV.

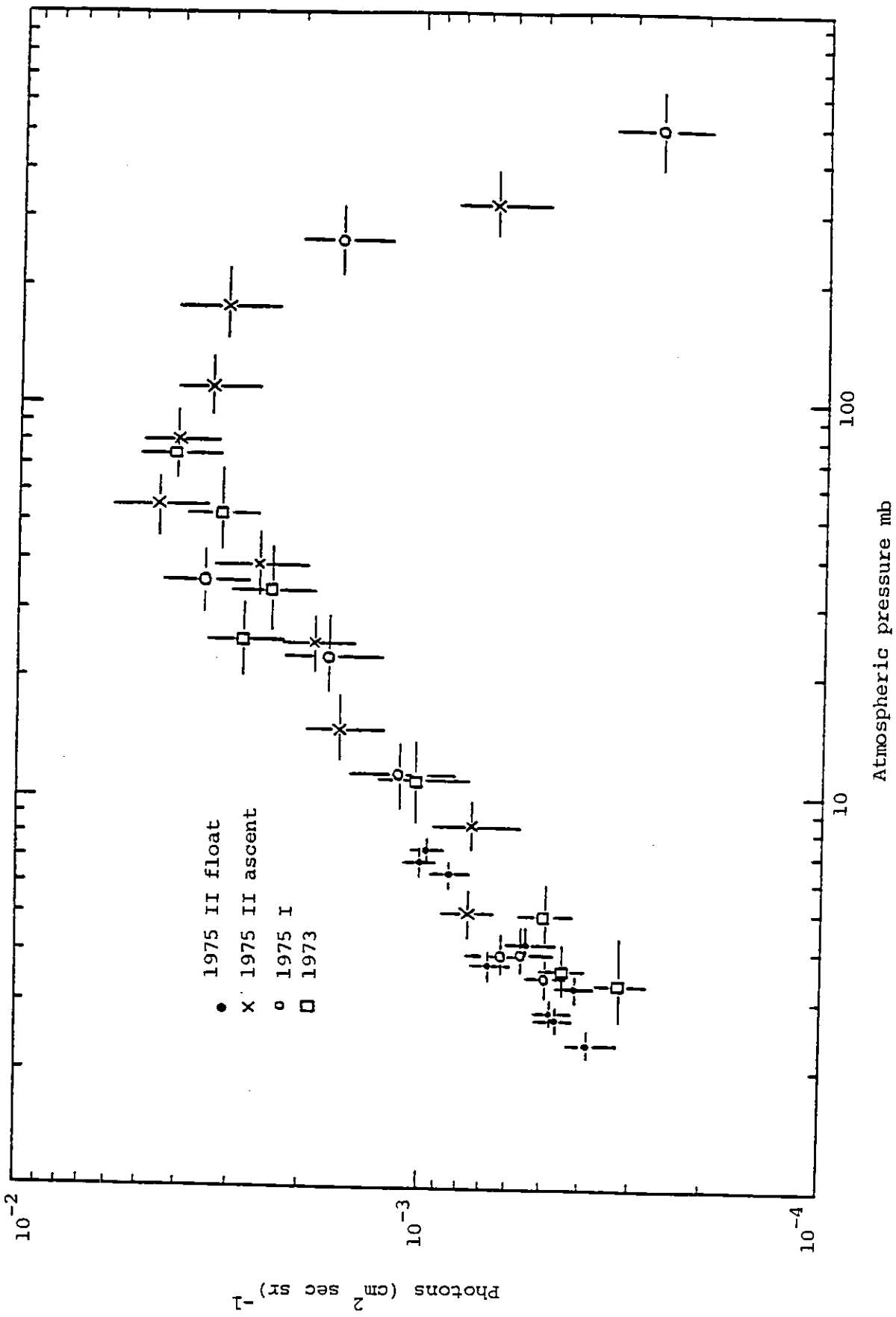

Figure 5.7b Depth curve for atmospheric gamma-rays in the energy range 0.7 < E < 1.0 GeV.

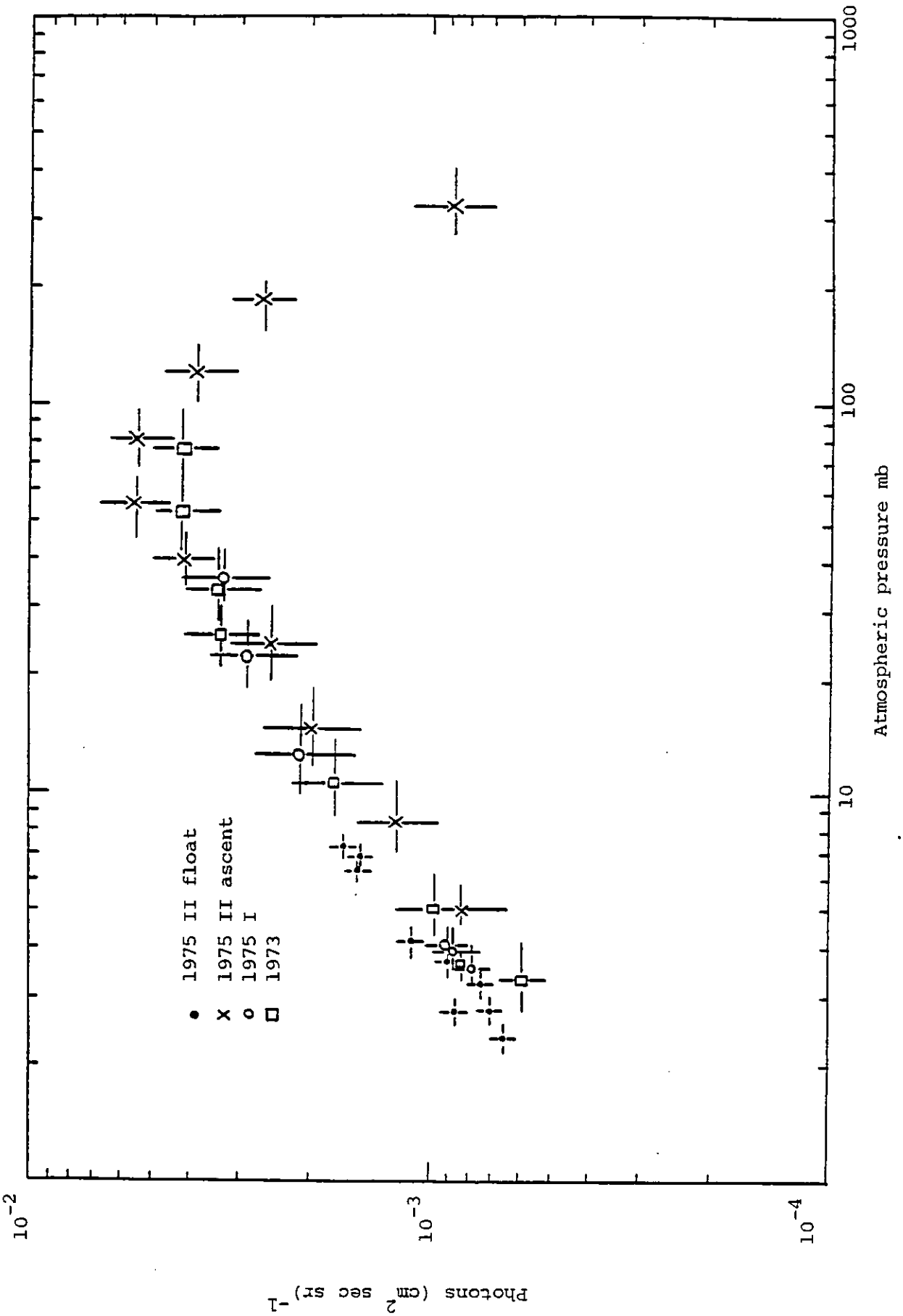

Figure 5.7c Depth curve for atmospheric gamma-rays in the energy range 1.0 < E < 2.0 GeV.

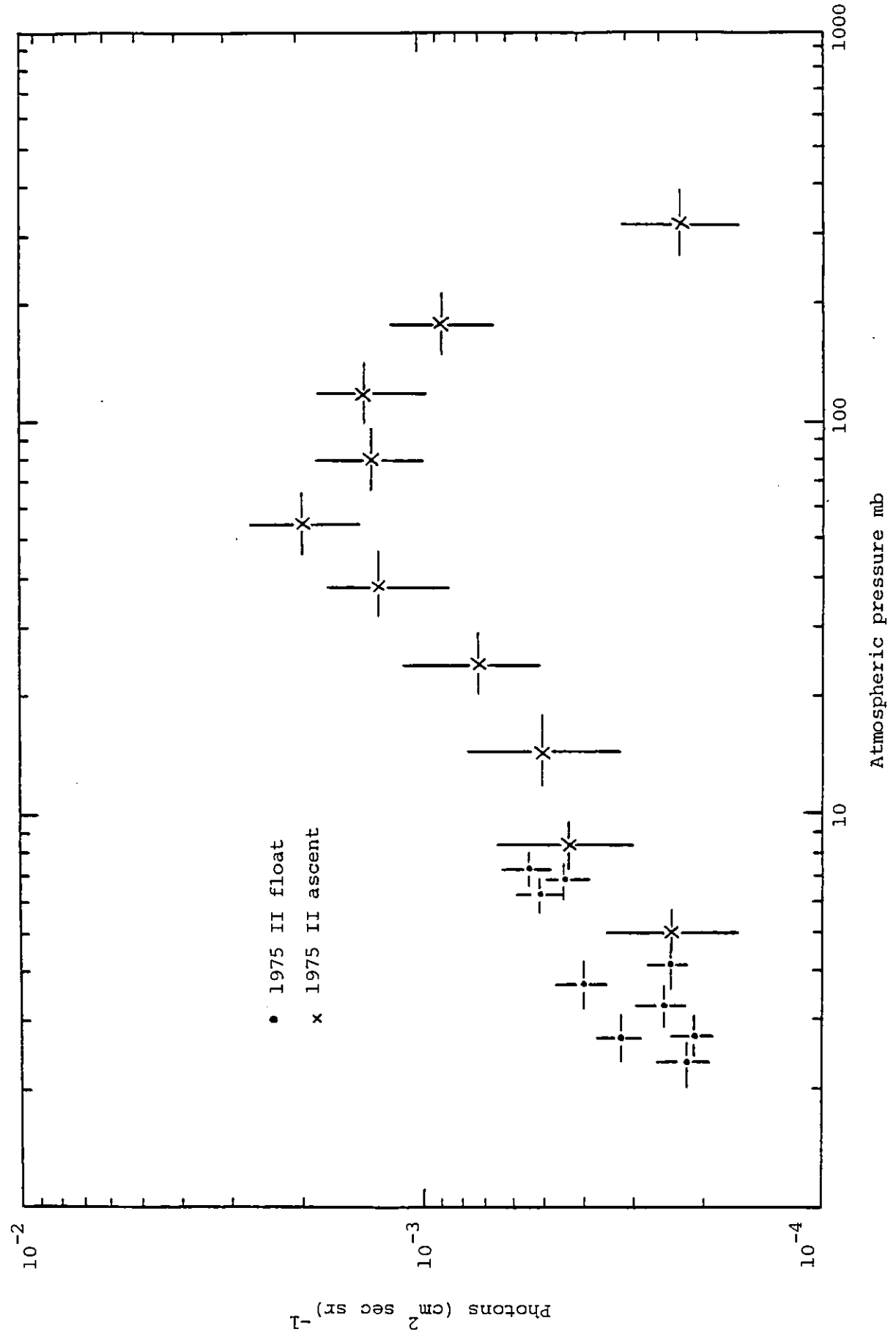

Figure 5.7d Depth curve for atmospheric gamma-rays in the energy range 2.0 < E < 3.0 GeV.

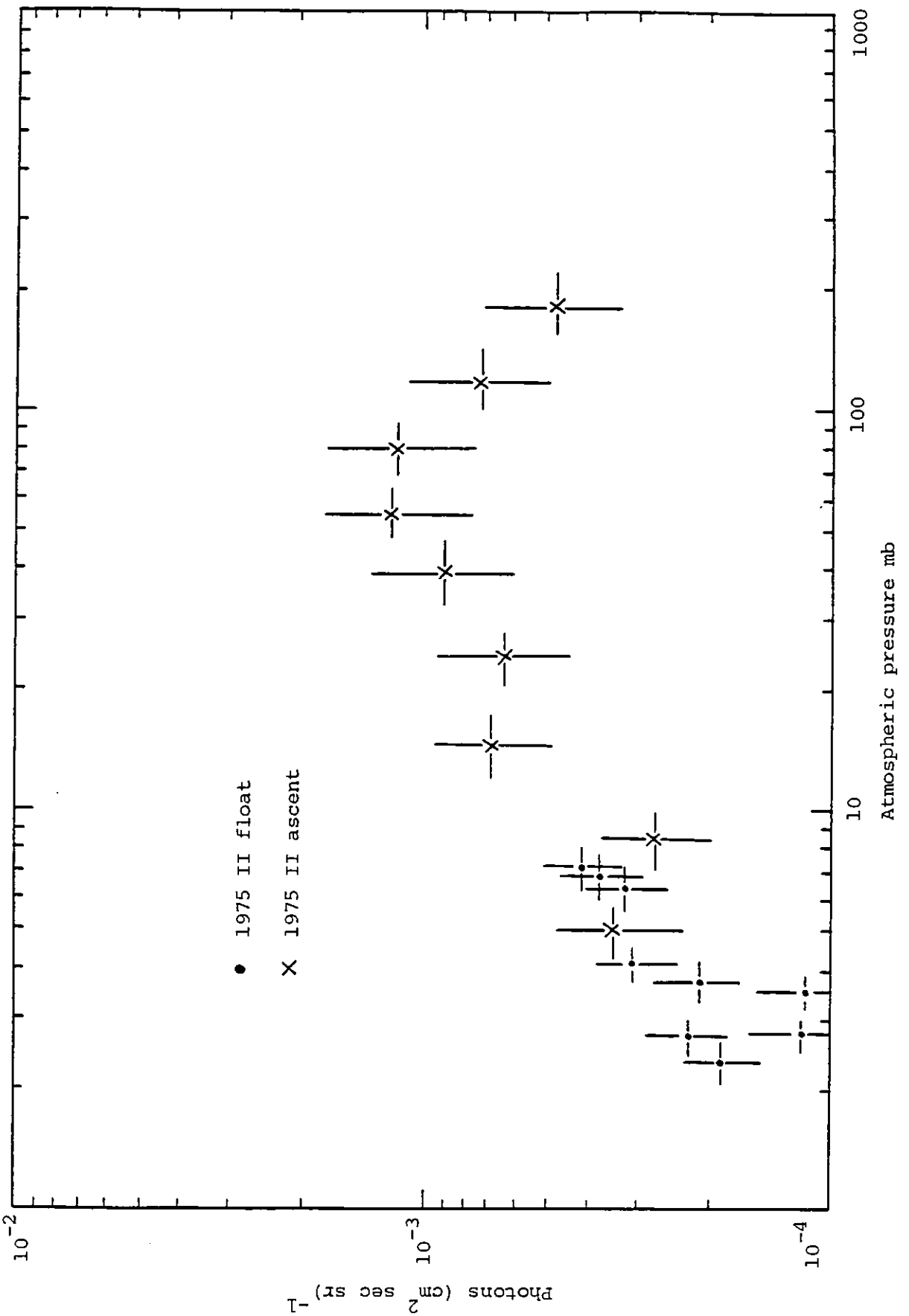

Figure 5.7e Depth curve for atmospheric gamma-rays in the energy range 3.0 < E < 5.0 GeV.

5.2 Results from the Galactic Plane

The flight and exposure programs were used to produce a skymap and an exposure map in galactic coordinates. Only those events which had previously satisfied all criteria regarding spark coordinates, scintillator and lead glass pulse heights, etc. in the calibration program, were considered by the flight program. Here, the events were analysed for arrival direction in Galactic coordinates using bins 2° wide in longitude and of such a width in latitude as to give bins of equal solid angle normalised to 2° x 2° on the Galactic equator. The exposure to each of these bins was calculated in the exposure program from the geometry of the detector, the different efficiency factors described in section 4.3.4 and the flight record (that is, the variation of altitude, longitude and latitude with time) which was required to transform the pointing direction of the detector into the galactic frame of reference. The exposure map for the 1975 (11 hour) flight is shown in Figure 4.6.

The division of the observed counts by the exposure was performed in the flux program (see section 4.3.5). In the calculations, only bins having an exposure greater than 10% of the maximum exposure were used. Bins within $|\ell^{II}| < 30°$ were combined into latitude strips of 2° width and the number of counts, the total exposure and the average flux were determined for each strip. Beginning at the galactic equator, adjacent strips were then combined into bands, whose width was equal to the angular resolution of the detector in the energy range under consideration (300-600, 600-1400, 1400-2500 MeV; 1400-5000 MeV if unit II). At high galactic latitudes, the bands were widened further to improve the statistics.

Figures 5.8-5.10 show the fluxes as a function of Galactic latitude in the three different energy ranges for each of the three

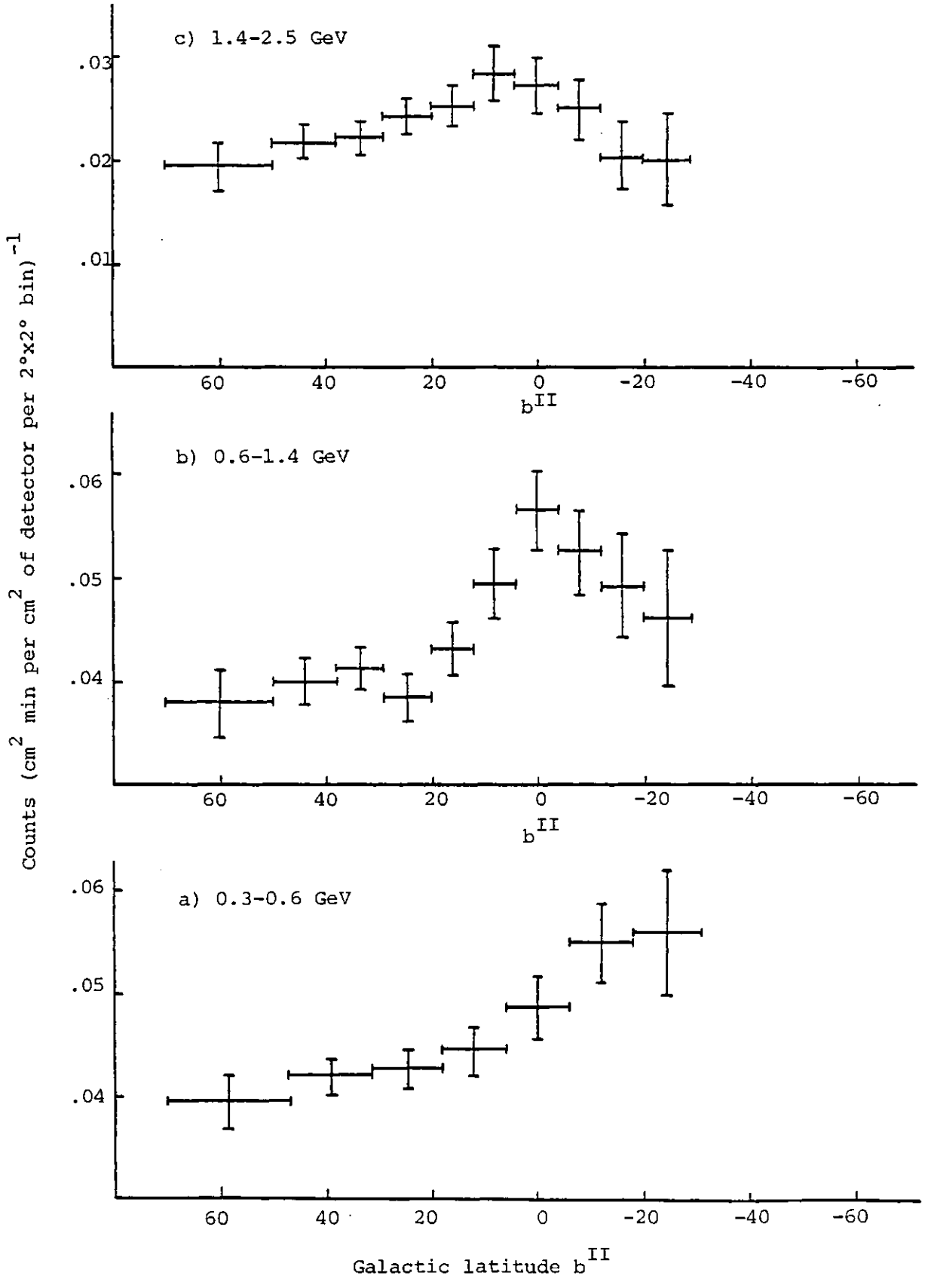

Figure 5.8 Gamma fluxes as a function of Galactic latitude for the 1973 flight before correction was made for the east-west effect and the variations in altitude and latitude.

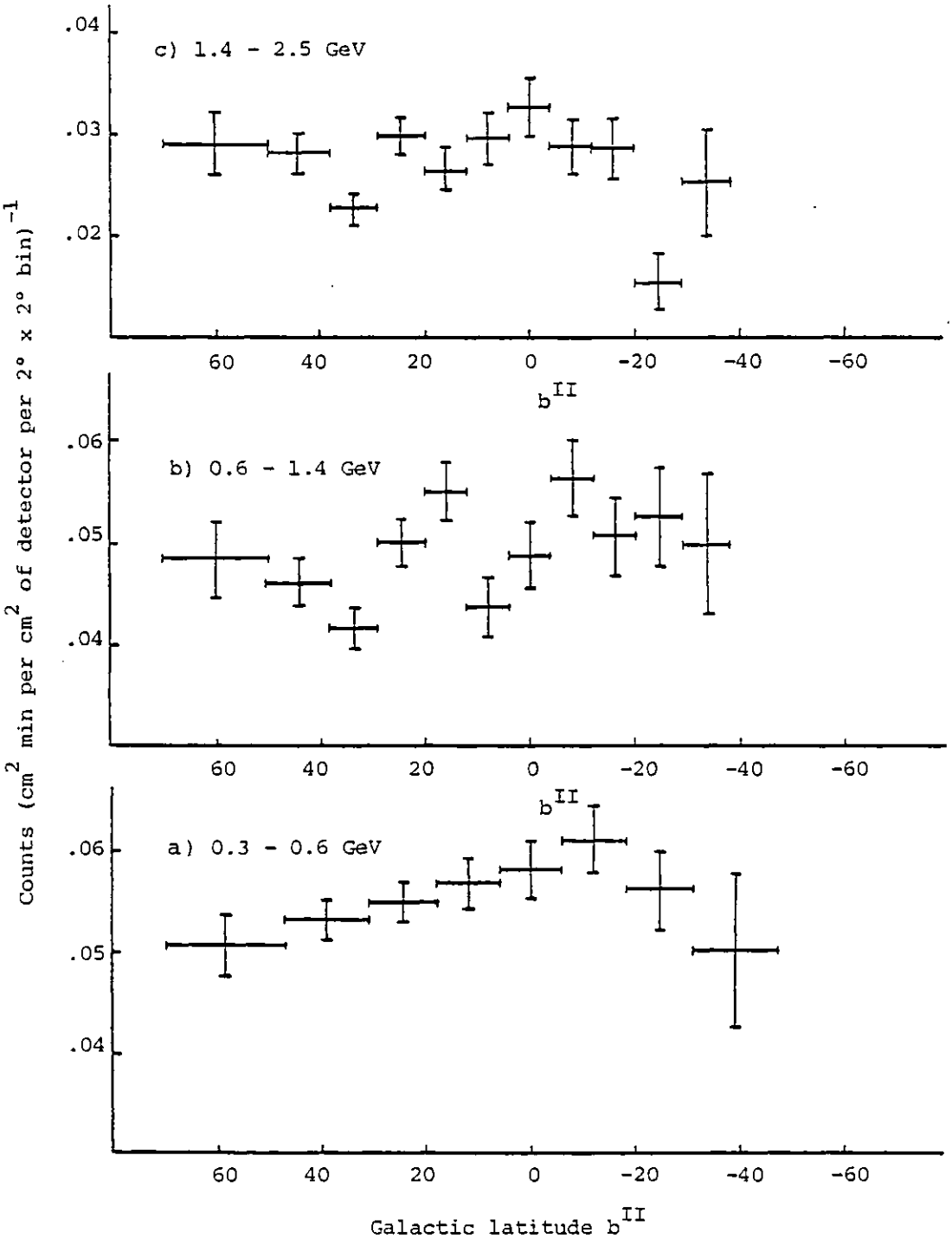

Figure 5.9 Gamma fluxes as a function of Galactic latitude for the 1975 I flight before correction was made for the east-west effect and the variations in altitude and latitude.

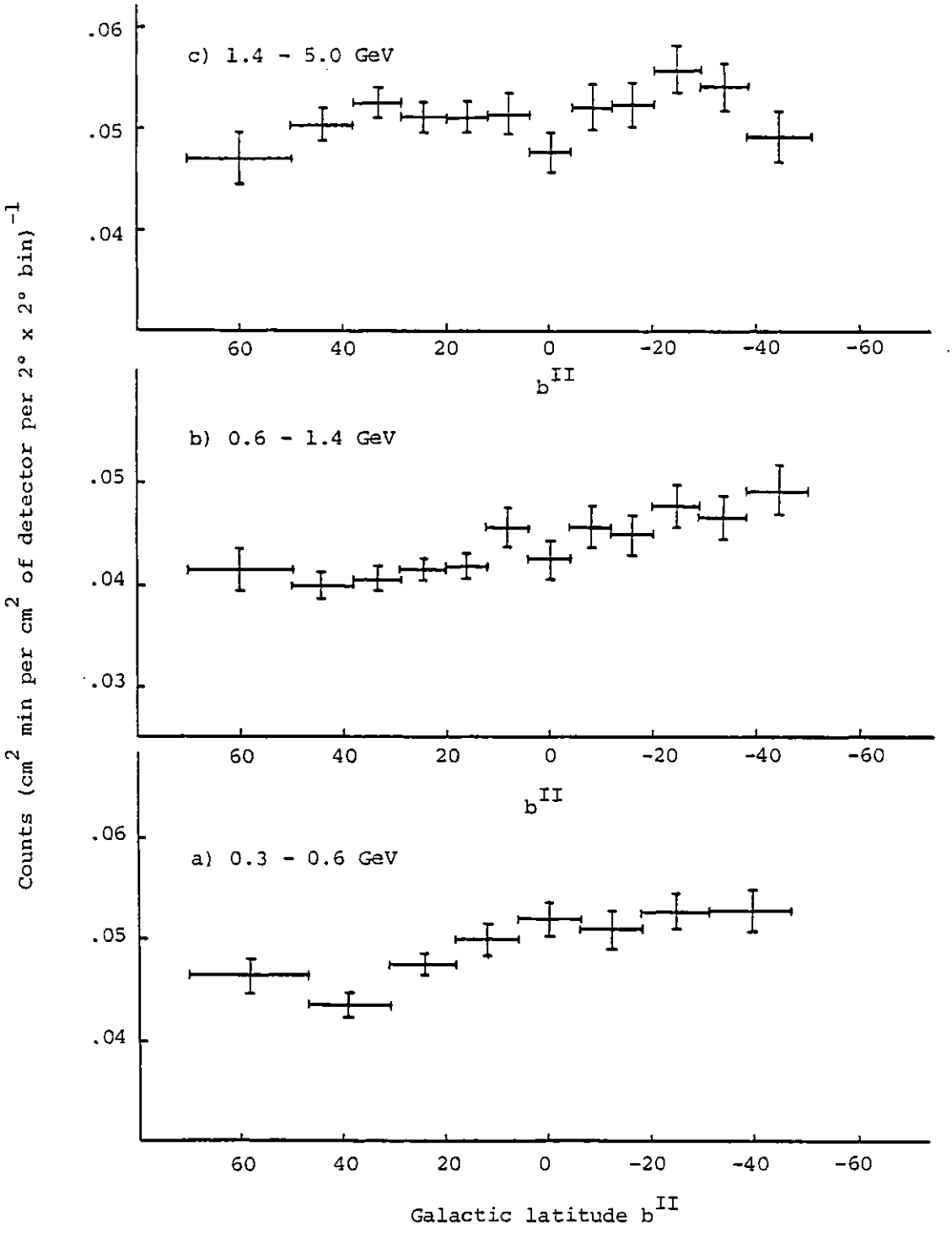

Figure 5.10 Gamma fluxes as a function of Galactic latitude for the 1975 II flight before correction was made for the east-west effect and the variations in altitude and latitude.

balloon flights (1973 and 1975). Ideally, any galactic signal would appear as an anisotropy above a level background, however the atmosphere itself produces a small anisotropy, due to the East-West effect and the variations in altitude and latitude of the balloon (see sections 5.1.1, 5.1.2). To compensate for the East-West difference, the counts were weighted, in a modified version of the flight program, according to their direction of arrival in the geomagnetic frame of reference, as described in section 5.1.1. The altitude-latitude variation was removed by introducing an additional time-dependent efficiency factor into the exposure computer program. This factor, which was normalised to a value of unity at an altitude of 3 mb, used the gamma-ray production rates/gm cm^{-2} (which were known as a function of energy from the slopes of Figures 5.4a)-e)) to determine the rate for all values of the product of depth (mb) and cosmic ray flux CR; the variation of CR with time, as plotted in Figure 5.2, having also been added to the exposure program.

This method of weighting the counts and exposures to correct for the atmospheric anisotropy has the disadvantage that source fluxes as well as background fluxes are given weighted values. However if the weighting factor is normalised to unity at the position of the source under study then the error which is introduced into the measured flux is negligible.

Figures 5.11-5.13 show the corrected fluxes as a function of latitude for the different energy bands and flights. The enhancement observed in the medium-energy range in 1973 (and reported by Clayton, 1975 who measured a 3.9σ signal from the Galactic plane) was confirmed, but with reduced significance - 2.9 standard deviations for 43 excess photons. This is equivalent to a differential galactic flux of $9.18 \pm 3.17 \times 10^{-6}$ photons cm^{-2} sec^{-1} rad^{-1} 100 MeV^{-1}, which was calculated

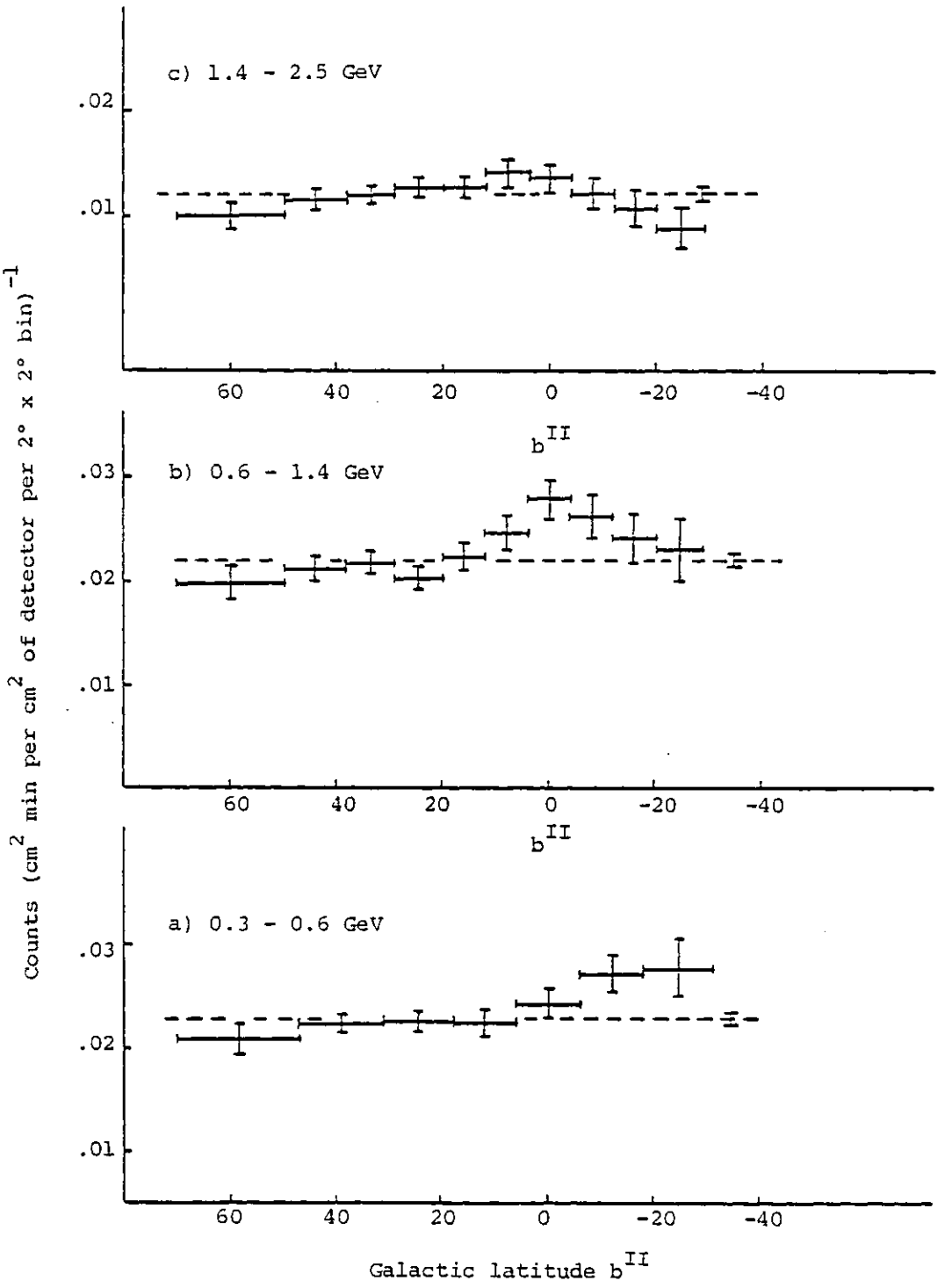

Figure 5.11 Gamma fluxes as a function of Galactic latitude for the 1973 flight after correcting for the east-west effect and the variations in altitude and latitude.

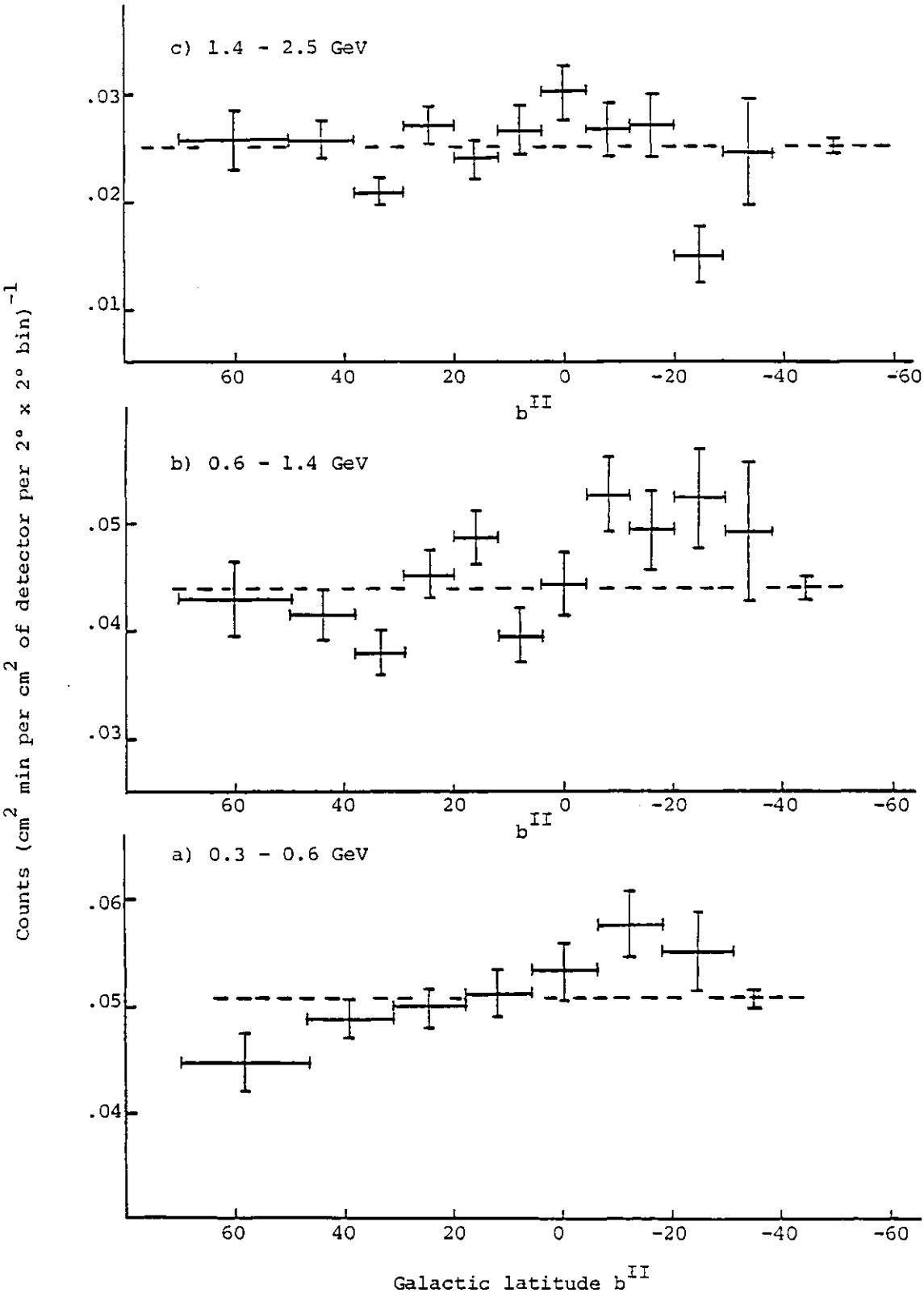

Figure 5.12 Gamma fluxes as a function of Galactic latitude for the 1975 I flight after correcting for the east-west effect and the variations in altitude and latitude.

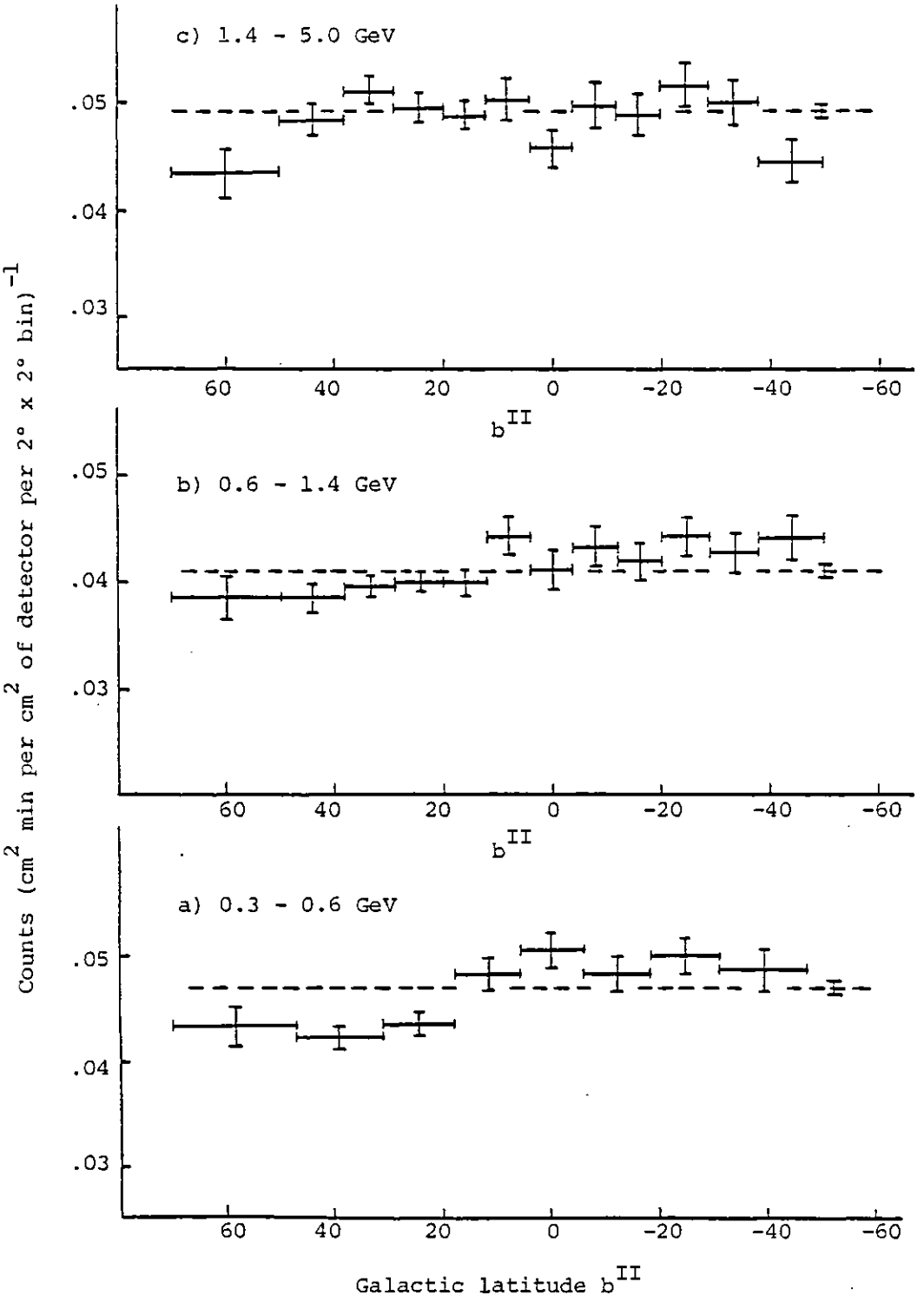

Figure 5.13 Gamma fluxes as a function of Galactic latitude for the 1975 II flight after correcting for the east-west effect and the variations in altitude and latitude.

using the following formula :

$$I(E) = \frac{N \times g(E) \times C \times j(E) \times n}{AT \times A \times 60 \times (\frac{2}{57.3}) \times \varepsilon(E) \times E_n} \text{ photons cm}^{-2} \text{ sec}^{-1} \text{ rad}^{-1} \text{ 100 MeV}^{-1} \quad (5.2)$$

where N is the excess number of counts observed above the background in a 2n° wide strip, and AT is the exposure in units of (cm^2 min per cm^2 of the detector per 2° x 2° bin). A is the detector area, (2/57.3) is the conversion factor for degrees to radians and E_n the width of the energy interval in 100 MeV's. The other factors were defined in section 5.1.3 : g(E) corrects for the energy resolution of the calorimeter, C is the correction for atmospheric absorption, j(E) compensates for the loss in efficiency due to the scintillator cut-off and $\varepsilon(E)$ is the converter efficiency.

However, neither of the 1975 flights saw an increase in flux from the Galactic plane (see Figures 5.12b, 5.13b). Indeed, when the results from the three flights are combined in Fig.5.14b, the signal observed in 1973 disappears and, within the statistical errors of the measurements, a flat distribution is seen.

There was no significant flux near $b^{II} = 0$ in the low and high energy intervals from the three flights. Again, despite the apparently large spread of several distributions, the scatter on the points in these plots is consistent with a random distribution around the weighted mean, which is shown as a horizontal line, according to simple chi-squared (χ^2) tests, although in several instances, it is possible to obtain a better fit to a simple curve. This last point indicates that the various sources of non-uniformity in the background flux may not have been fully accounted for in the computations. For example, the corrections introduced into the flight and exposure computer programs were not, presumably,

entirely successful in removing the East-West effect and the variations in cut-off rigidity and altitude. This could be partly due to errors in the altitude measurement and local deviations of the cut-off rigidity from the model value, which were mentioned as possible sources of error in section 5.1.3. On the other hand, it may be that the sun was affecting the gamma background. No correction was made for solar activity because there were no major solar events during the balloon flights. However, it is not inconceivable that a minor flare, say, could dump charged particles into the atmosphere and thereby give rise to flux variations.

Figure 5.14 shows the gamma fluxes as a function of Galactic latitude in the three different energy bands derived from data obtained in all the flights. In summing this data the flux measurement from each flight (corrected of course for atmospheric effects) has been weighted according to the efficiency and background level for that flight.

2σ upper limits on the line flux from the Galactic plane were calculated using equation 5.2 from the counts collected at $b^{II} = 0$. The upper limits are given in Table 5.3 and are plotted in Figure 5.15 which also shows the differential spectrum measured by COS-B (Bennett et al, 1977) from the same region of the Galaxy. The horizontal bars on the upper limits represent the energy interval over which the measurement was made.

Our 2σ upper limits are consistent with the COS-B spectrum and provide further evidence of a smaller than expected contribution from π° decay to the total emission.

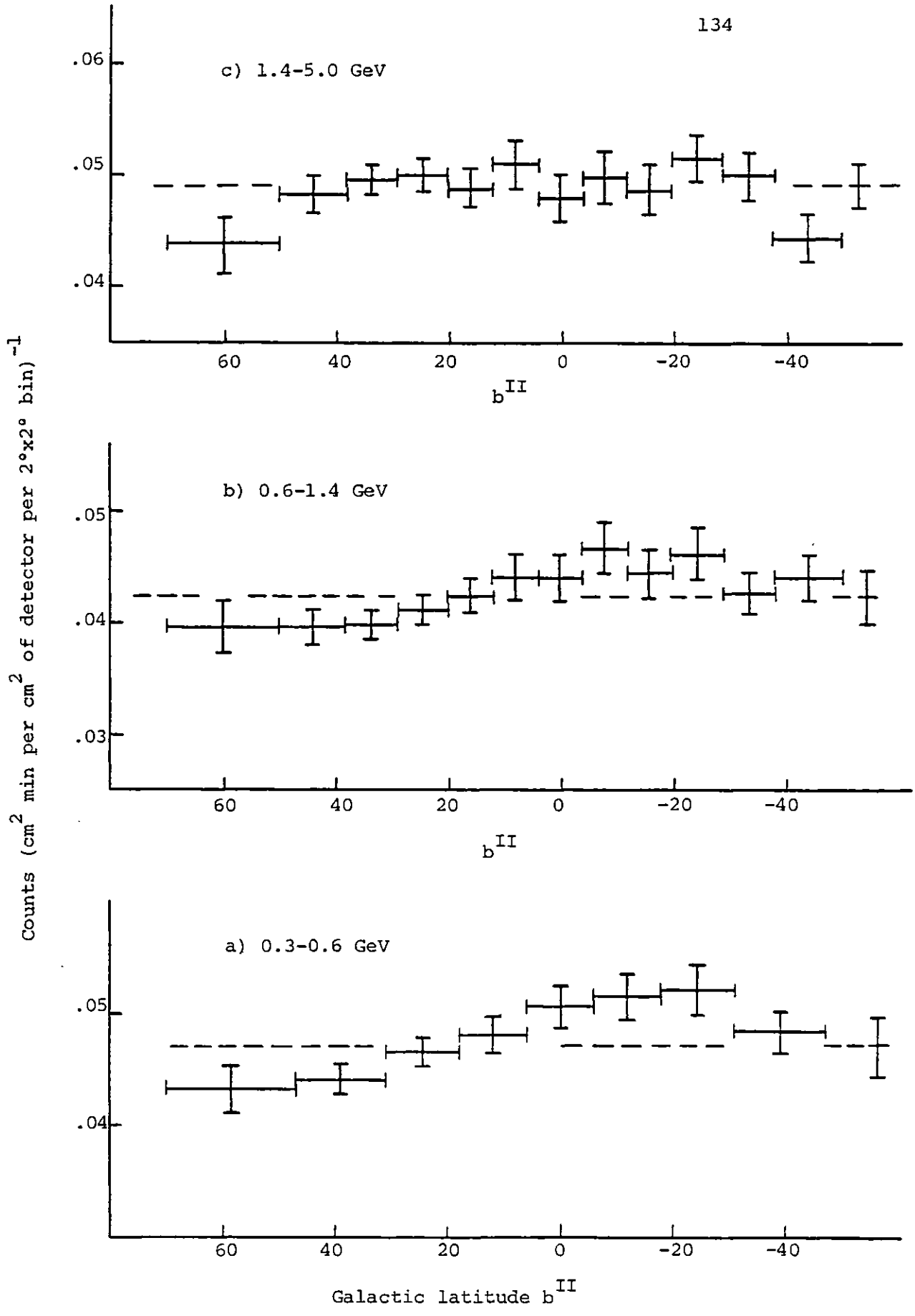

Figure 5.14 Gamma fluxes as a function of Galactic latitude derived from data obtained in all the flights as described in section 5.2. The horizontal line is the weighted mean excluding the bin at $b^{II}=0°$.

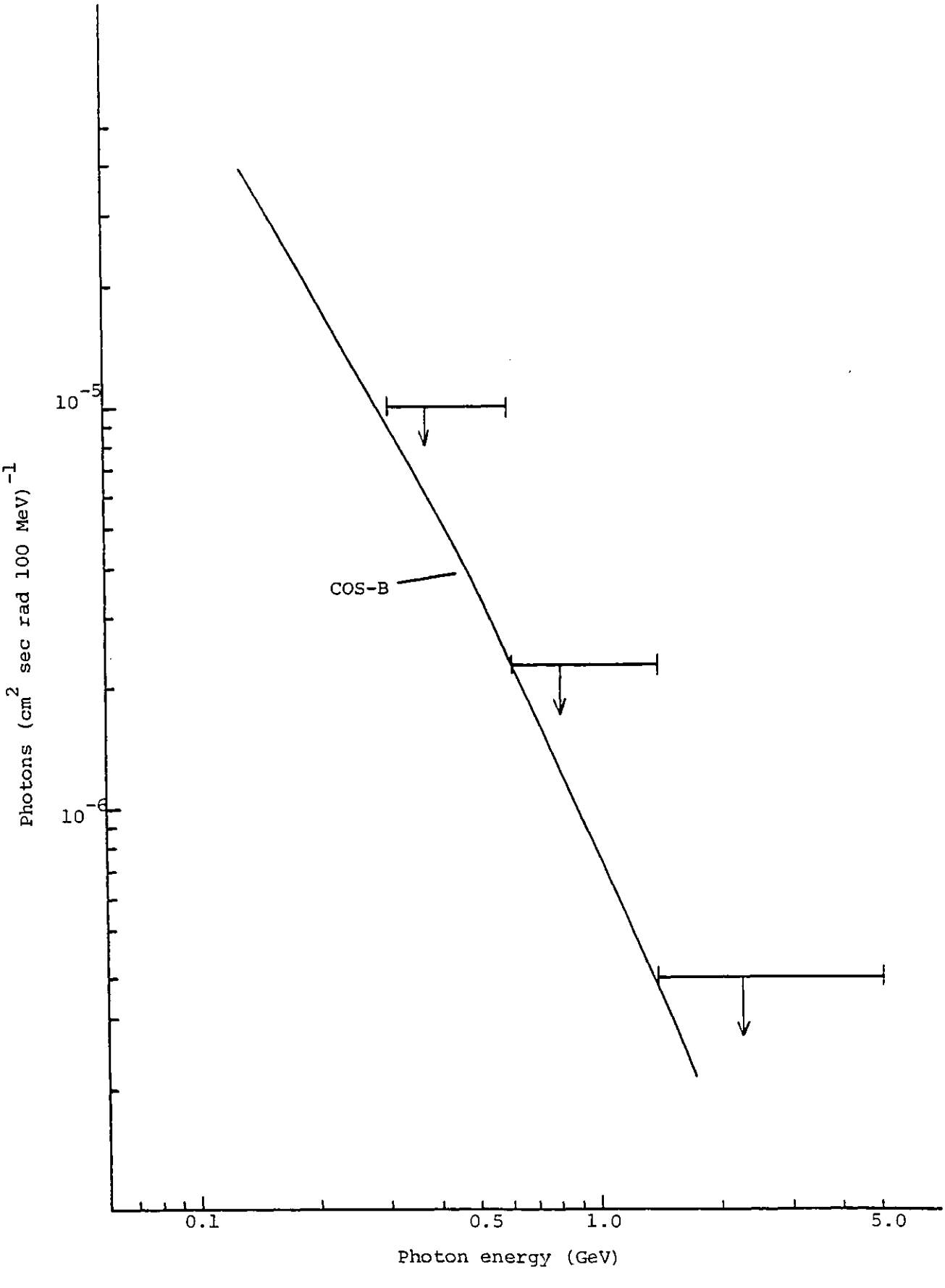

Figure 5.15 Upper limits from the balloon flights compared with the COS-B spectrum for the emission from the Galactic plane.

TABLE 5.3

Energy Range (GeV)	2σ upper limits ph$(cm^2 sec\ rad\ 100\ MeV)^{-1}$	Width of strip
0.3-0.6	1.03×10^{-5}	$\|b^{II}\| < 6°$
0.6-1.4	2.27×10^{-6}	$\|b^{II}\| < 4°$
1.4-5.0	3.79×10^{-7}	$\|b^{II}\| < 4°$

5.3 Point Sources

The sky map of gamma events produced by the flight program was examined together with the corresponding exposure map for evidence of point source emission. This was undertaken for two energy intervals 0.3-0.6 GeV and 0.6-2.5 GeV using data obtained from the three balloon flights of 1973 and 1975. Instead of adopting a scanning procedure, specific sources were studied e.g. COS-B gamma sources including the Vela pulsar, well-known hard X-ray sources and other regions of interest. Bins adjacent to the possible source position were summed together to include an angle equal to the angular resolution of the instrument in the energy range under consideration. The total number of counts was compared with the number expected from the background, the background flux being measured in the surrounding bins.

Table 5.4 contains the observed and expected number of events from the various sources in the two energy intervals. Although several enhancements of marginal significance were seen, there was no excess $> 3\sigma$ and therefore 95% confidence upper limits were placed on all the sources (see Table 5.4). The limits quoted for solar emission apply for conditions of negligible solar activity, as there were no major solar events at the time of the flights.

TABLE 5.4

Source	Energy (MeV)	Observed Counts	Expected Counts	2σ Upper Limits (10^{-6} ph cm^{-2} s^{-1})
Sun	300-600	43	54	5.47
	600-2500	34	33	4.63
Vela Pulsar	300-600	27	18	16.1
	600-2500	11	10	9.95
PSR 0740-28	300-600	46	47	7.41
	600-2500	23	38	4.91
PSR 1822-09	300-600	58	47	6.54
	600-2500	30	27	4.89
2CG 218-0	300-600	17	13	9.98
	600-2500	10	10	7.85
2CG 235-1	300-600	47		7.66
	600-2500	29	27	5.43
2CG 353+16	300-600	95	95	4.31
	600-2500	67	55	4.29
2CG 356+0	300-600	101	92	4.87
	600-2500	60	54	3.74
2CG 366-0	300-600	114	84	4.85
	600-2500	56	64	3.21
SCO X-1	300-600	79	73	4.51
	600-2500	44	47	3.39
SCO X-2	300-600	43		6.94
	600-2500	24	28	4.81

CHAPTER VI

PULSARS

6.1 Introduction

The longitudinal profile of gamma radiation along the Galactic plane, with a broad enhancement within ±40° in longitude of the Galactic centre, was originally established by the OSO-3 satellite (Kraushaar et al, 1972). The confirmation of the overall shape of the distribution by SAS-2 (Fichtel et al, 1975) heralded the appearance of many theoretical articles attempting to explain the distribution.

Most authors supported the argument that the high energy gamma radiation results primarily from diffuse processes in interstellar space- interactions of cosmic ray nuclei with interstellar matter. For example, Bignami and Fichtel (1974), assuming that cosmic rays are galactic, proposed that the cosmic-ray density is proportional to the matter density and that the constituents of interstellar hydrogen i.e. neutral atomic, ionised atomic and molecular are distributed in a spiral pattern consistent with 21 cm radio observations and density wave theory. They assumed that the amounts of atomic and molecular hydrogen within the inner Galaxy are the same, however Stecker et al (1975), using surveys of 2.6 mm carbon monoxide emission, argued that molecular hydrogen is far more abundant in this region. Stecker et al also concluded that the cosmic ray density is not uniform, but is proportional to the total gas density to the 0.3 power.

These and other similar attempts e.g. Paul et al (1974, 1975),

Schlickeiser and Thielheim (1974) to reproduce the gamma-ray longitudinal distribution using detailed cosmic-ray and matter distributions may be premature, in view of the COS B results. From an analysis which is not complete, COS B has detected 25 point-like sources. It is confidently predicted that many additional sources will be discovered when currently available and forthcoming COS B data is analysed. If this is realised, the localised source contribution to the total Galactic gamma emission will become very important.

Two of the observed sources are uniquely identified with the Crab and Vela pulsars and it is tempting to conclude that pulsars are gamma-ray sources. It is therefore appropriate to consider the possible pulsar contribution. This is discussed later, but firstly COS B observations of the pulsed gamma-emission from the Crab and Vela are reviewed. This is followed by a brief description of the theory of pulsars and their surrounding magnetospheres, with special emphasis on the predicted gamma-ray emission.

6.2 Crab and Vela gamma-ray sources

These have very similar gamma-ray light curves consisting of two narrow peaks of approximately equal intensity separated by 0.42 of the period. The Crab pulsar exhibits this double peak structure, with the same phase relationship, at other wavelengths (radio, optical and X-ray) unlike Vela which has two peaks in the optical band, one peak only in the radio region and produces no detectable pulsed X-ray emission.

There are spectral differences between the Crab and Vela gamma-ray sources. The energy spectrum of the pulsed emission from the Crab pulsar is shown in Figure 6.1a. The spectrum can be fitted with a single power law :

$$I(E) = (2.0 \pm 0.2) \times 10^{-7} E^{-(2.2 \pm 0.2)} \text{ photons cm}^{-2} \text{ sec}^{-1} \text{ GeV}^{-1}$$

It is compared with the spectrum of the total emission in Figure 6.1b. Above 400 MeV, the spectra show good agreement, consistent with the emission above 500 MeV being 100% pulsed. Between 50 and 400 MeV, the total spectrum lies above the pulsed spectrum and the average pulsed fraction is only 55%. Within statistical errors, the pulsed spectrum extrapolates to measurements at hard X-ray energies.

The Vela pulsed spectrum is shown in Figure 6.2a and is superimposed on the total spectrum in Figure 6.2b. Within the statistical uncertainties the spectra are identical, which indicates a pulsed fraction of at least 90% in the energy range from 50 MeV to 3.2 GeV. The integrated pulsed flux above 100 MeV is $\sim 1.2 \times 10^{-5}$ photons cm^{-2} sec^{-1}. The upper limits of the pulsed X-ray flux are a factor of 4 below the extrapolation of the pulsed gamma-ray spectrum, implying two different emission mechanisms for X-rays and gamma-rays.

COS-B and SAS-2 have conducted surveys to detect gamma-ray emission from other radio pulsars. Both searches were based on a chi-squared (χ^2) test on the phase histograms obtained by folding the gamma-ray arrival times with the values of the period P and the period derivative $\dot{P}$ extrapolated to the epoch of the gamma-ray observations. SAS-2 reported evidence of gamma-ray emission from two radio pulsars PSR 1747-46 and PSR 1818-04 (Ogelman et al 1976), however no positive results were obtained by COS-B and the gamma-ray pulsation of PSR 1818-04 was not confirmed (Kanbach et al, 1977). However, the difficulty in observing γ-ray pulsars should be stressed. First of all, the poor statistics increases the probability of obtaining spurious results. Secondly, precise values of $P,\dot{P}$ are essential because of the long observation times necessary to collect sufficient gamma-ray data. The

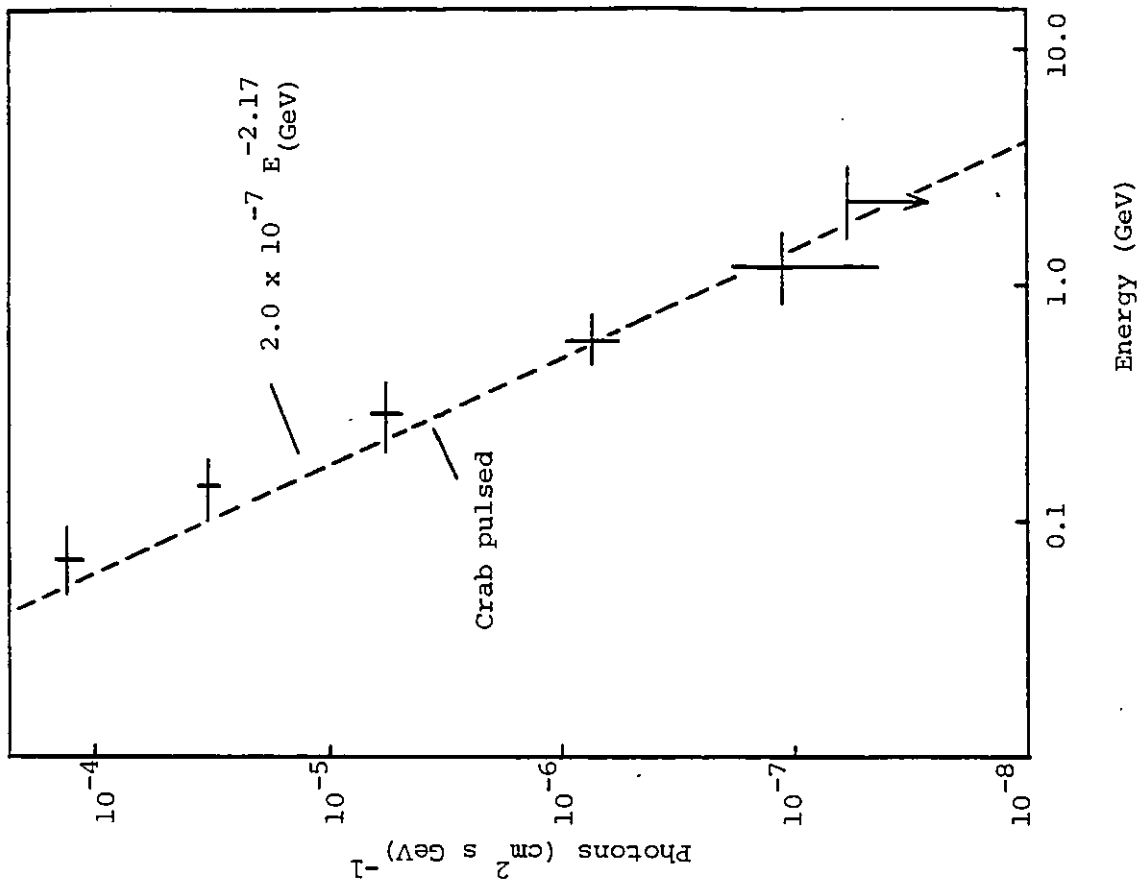

Figure 6.1b Energy spectrum of the total emission from the Crab gamma-source.

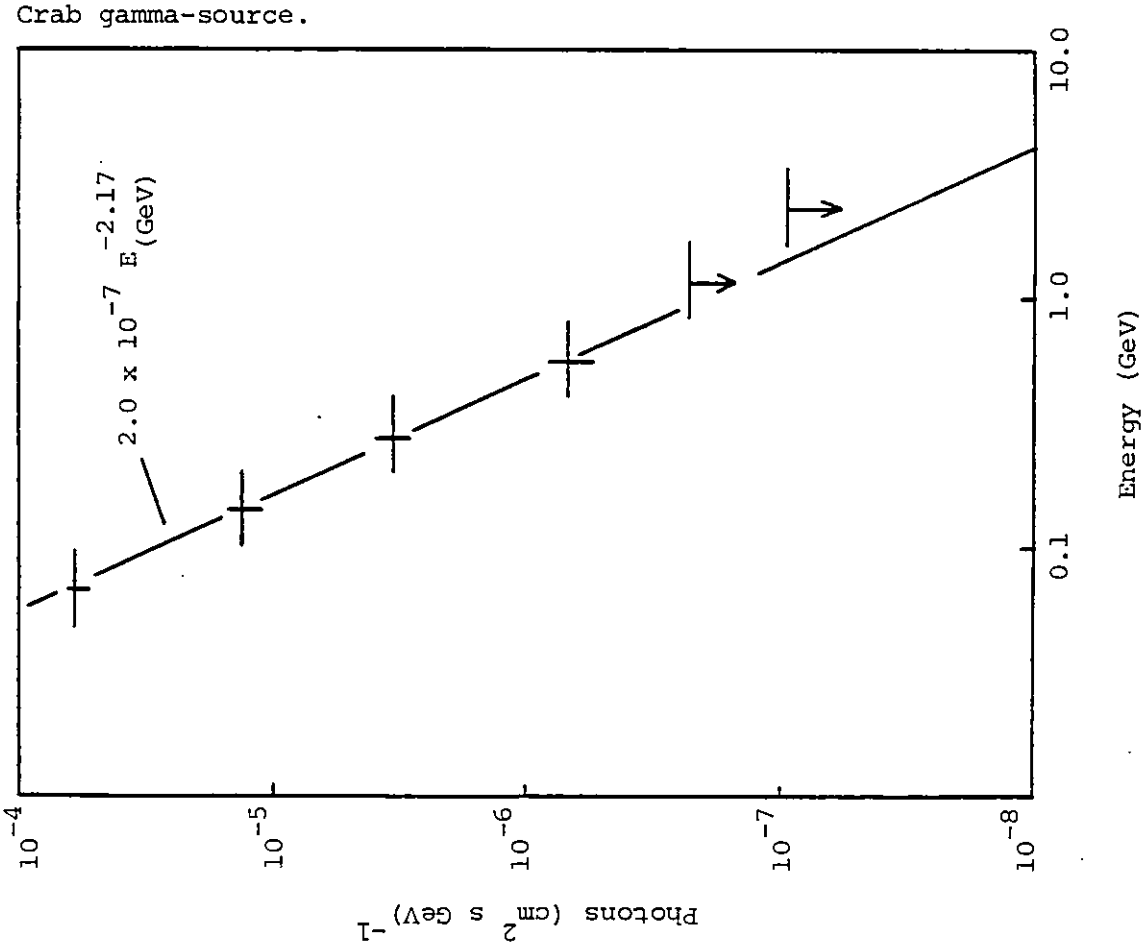

Figure 6.1a Energy spectrum of the pulsed emission from the Crab pulsar.

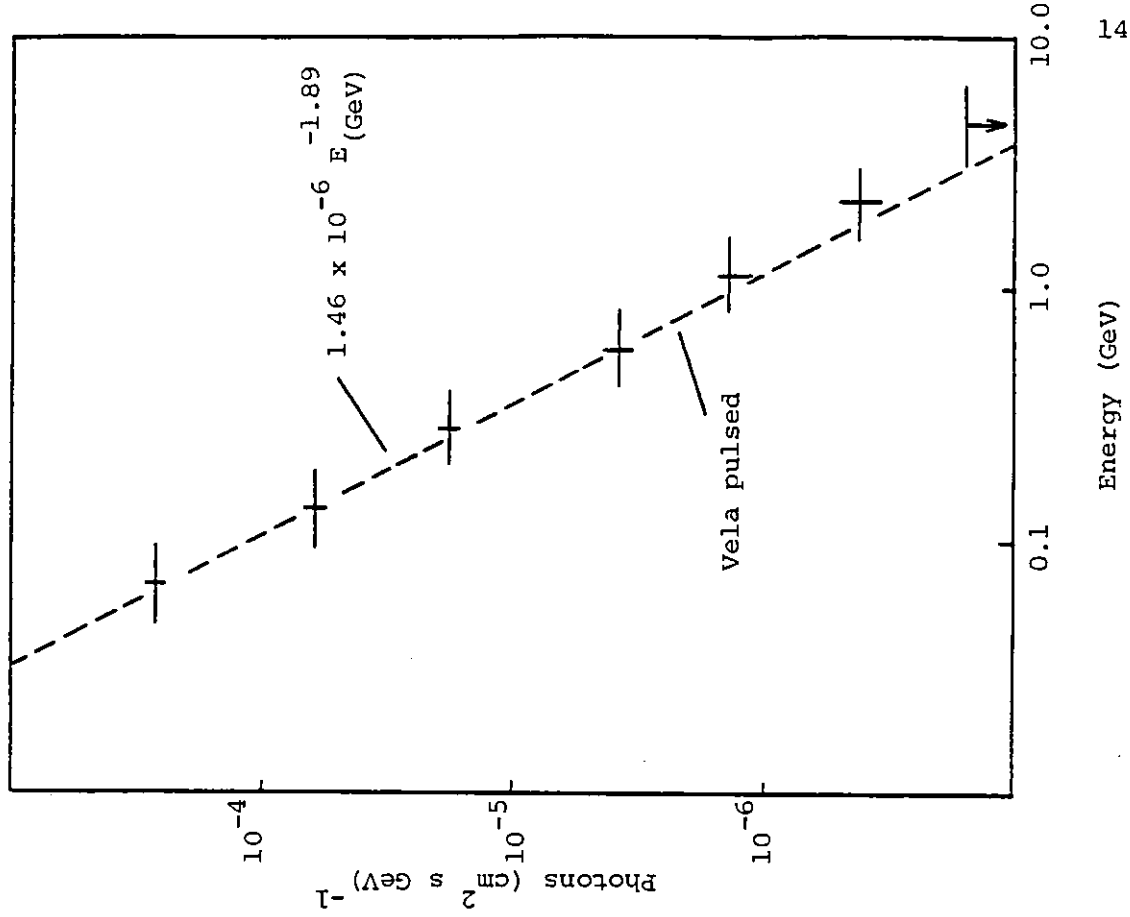

Figure 6.2b Energy spectrum of the total emission from the Vela gamma-source.

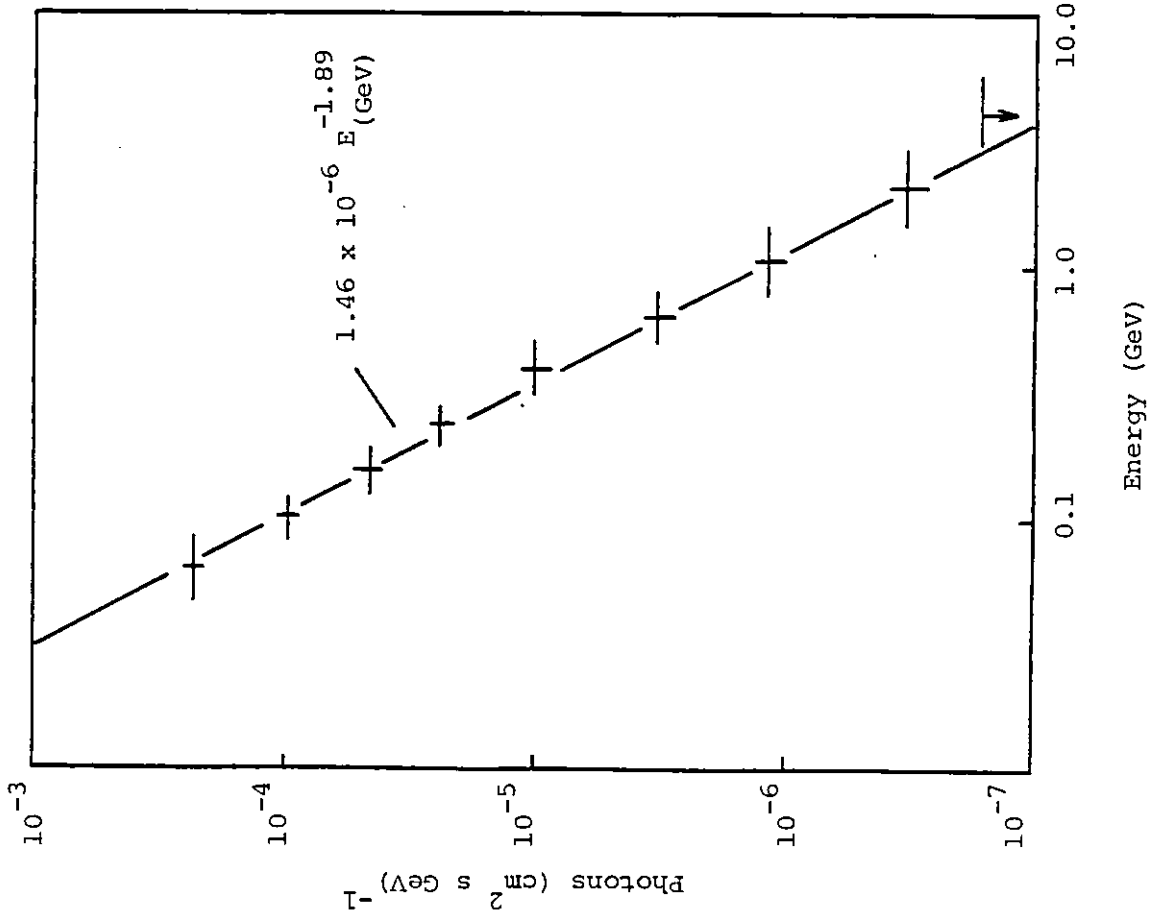

Figure 6.2a Energy spectrum of the pulsed emission from the Vela pulsar.

radio timing parameters should be contemporary with the gamma-ray measurements. Extrapolation over long time intervals between the radio and gamma-ray observations is inaccurate, because of unpredictable irregularities in the period i.e. glitches.

6.3 Pulsar Theory

It is generally accepted that pulsars are rapidly rotating, highly magnetised neutron stars. Because of the intense gravitational fields at the surfaces of neutron stars, the scale height of a neutral atmosphere would be very small - approximately 1 cm for a surface temperature of 10^6K - thus early models of the pulsar magnetosphere considered vacuum conditions only. The existence of an atmosphere of charged particles was first shown by Goldreich and Julian (1969). The plasma-filled magnetosphere arises from induced electric fields generated by the rotating magnetic field of the pulsar. The electric field at the surface is of order

$$|E| \approx \Omega r_o B/c$$

where r_o is the stellar radius, Ω is the angular velocity and B is the magnetic field. For the Crab pulsar, $B = 10^{12}$ gauss and $\Omega = 200$ sec^{-1}. The field is then approximately 10^{12} V cm^{-1}, which exceeds the effect of the gravitational field by many orders of magnitude. Thus factors determining the scale height are dominated by electrostatic forces. The electric field is sufficiently strong to overcome the surface binding energies and charged particles will be emitted from the star to fill the surrounding region. Because of the intense magnetic field, the particles are forced to corotate with the star. Corotation will continue until the velocity of corotation equals the velocity of light.

The surface where this condition occurs is a cylinder - the velocity-of-light cylinder, with a radius

$$R_L = c/\Omega \approx 5 \times 10^9 \text{ P cm}$$

where P is in seconds.

Figure 6.3 shows the field pattern obtained by Goldreich and Julian. The open field lines originate near the poles and cross the velocity-of-light cylinder; the closed field lines do not penetrate the light cylinder. The extreme closed field line originates at an angular distance θ_o from the poles, given by

$$\sin \theta_o \approx \left(\frac{\Omega r}{c}\right)^{\frac{1}{2}}$$

and meets the light cylinder tangentially. Since electrons and protons are guided by the magnetic field lines, they can only escape from the magnetosphere along the open field lines.

Goldreich and Julian considered a simplified system (an axi-symmetric rotator, with the rotation and magnetic dipole axes parallel) whereas the magnetic axis must be inclined to the rotation axis in order to produce a periodic signal. They do not give a self-consistent description of the currents and fields surrounding the star. Furthermore, the assumption of Goldreich and Julian that charged particles are emitted freely from the star may be invalid because the very strong magnetic fields will tend to compress the crystalline crust and thereby increase the binding energies of the electrons and ions in the surface material. In order to overcome this restriction, a large fraction of the available electric potential must, presumably, be developed immediately above the polar cap. Thus Ruderman and Sutherland (1975) have suggested the

Figure 6.3 The Goldreich-Julian model of the magnetosphere of a pulsar with parallel magnetic and rotation axes. Open field-lines cross the light cylinder and are deflected back to form a toroidal field component. The plus and minus signs indicate the charge of particular regions of space.

formation of vacuum gaps of 100 m thickness above the star surface.

Despite the different theories on the distribution of the electric field, there is broad agreement that the particles emitted from the star will acquire sufficient energy to emit high energy gamma rays. Because of the strong magnetic field, the lifetime against synchrotron radiation is very short therefore the particles will flow parallel to the field lines with essentially zero pitch angle. However, the field lines will be curved in general, thus the electrons will be accelerated transversely and will radiate. This radiation, which is similar to synchrotron radiation, is called curvature radiation. The characteristic frequency for this radiation, analogous to the synchrotron relation, is

$$\omega_c \approx 3/2\ \gamma^3\ c/\rho_c$$

where γ is the Lorentz factor of the injected particle and ρ_c is the radius of curvature of the field-line. For $\gamma \approx 10^7$ and $\rho_c \approx 10^8$ cm, $\omega_c \approx 5 \times 10^{23}$ sec^{-1} i.e. gamma-rays with energy $E_\gamma = 1$ GeV. Sturrock (1971) has extended this argument and suggested the formation of a cascade process, whereby energetic gamma-rays moving in a magnetic field of $\sim 10^{12}$ gauss produce electron-positron pairs. The secondary particles are, in turn, accelerated and radiate gamma photons, which create further pairs. In this fashion, a large fraction of the available rotational energy may be converted into gamma rays.

A possible interpretation of the pulsed nature of the gamma-emission is two 'lighthouse' beams of radiation produced by particles flowing from the polar regions and along the open field lines.

6.4 Pulsar contribution to the Galactic gamma-ray emission

A re-appraisal of the contribution from point sources to the total gamma-ray emission has occurred, following the COS B discoveries. However, there were several authors who predicted an important contribution prior to the observational evidence e.g. Higdon and Lingenfelter (1976). They studied the possible pulsar contribution to the total gamma-ray emission and concluded that unresolved, short-period pulsars with luminosities comparable to the Crab and Vela sources could produce a substantial fraction of the total gamma-ray emission at energies > 100 MeV. Moreover, they point out that until the contribution of discrete sources is fully understood, the observed longitudinal variation of gamma-ray emission cannot be interpreted as evidence of either large-scale cosmic-ray gradients in the Galaxy or a Galactic origin of cosmic-rays.

Because of the limited statistical significance of the pulsar radio data available in 1976, Higdon and Lingenfelter, noting the qualitatively similar radial distributions of pulsars and carbon monoxide, assumed the pulsar density distribution was proportional to the better determined carbon monoxide (CO) distribution of Gordon and Burton (1976).

Carbon monoxide is considered a tracer of molecular hydrogen, H_2, an important constituent of interstellar gas. H_2 has few spectral features - the strongest emission feature occurs in the ultraviolet band, however large-scale galactic mapping is not possible because inter-stellar dust absorbs UV radiation. Molecular hydrogen occurs predominantly in dense, cool interstellar clouds, coexisting with other molecules. Excluding H_2, the most abundant molecule is carbon monoxide, which has a radio spectral line at 2.64 mm. It is thought that the most important source of CO excitation in clouds is the collision of CO with H_2, thus

2.64 mm radio measurements have been used to estimate the density of H_2.

However, the accuracy of CO as a tracer of molecular hydrogen has lately been questioned (Erice, 1979); indeed the validity of the assumption of proportionality between the pulsar and CO distributions is uncertain. Evidently, a pulsar distribution with improved statistics is required and this has recently become available with the publication of the latest survey from Molonglo Radio Observatory, Australia (Manchester et al, 1978).

In this survey, virtually all of the sky south of declination +20 was uniformly searched, resulting in the detection of 224 pulsars. Of these, 155 were new discoveries bringing the total number of known pulsars to 305. The positions, periods, dispersion measures, pulse widths and mean flux densities were measured for all of the newly detected pulsars. The sample of 224 pulsars has been analysed by Manchester (1979) to derive galactic distributions of pulsars.

6.4.1 Galactic distribution of radio pulsars

In his analysis, Manchester follows the techniques used by Taylor and Manchester (1977). The galactic distribution is assumed to be cylindrically symmetric. The number of detectable pulsars having periods between P and P+dP, luminosities between L and L+dL, galactocentric radii between R and R+dR, and perpendicular distances from the Galactic plane between z and z+dz is given by

$$N(P,z,R,L)\,dPdzdRdL = V(P,z,R,L)\;\rho(P,z,R,L)\,dPdzdRdL \qquad 6.1$$

where $V(P,z,R,L)dzdR$ is the volume of the Galaxy between z and z+dz and R and R+dR searched for pulsars of period P and luminosity L, and

$\rho(P,z,R,L)dPdL$ is the space density of pulsars having periods between P and P+dP and luminosities between L and L+dL at the galactic position (z,R). If the distributions of pulsars with respect to these parameters are uncorrelated, the density can be separated into four functions

$$\rho(P,z,R,L) = \rho_P(P)\ \rho_z(z)\ \rho_R(R)\ \rho_L(L) \qquad 6.2$$

Manchester defines the radio luminosity as $L = Sd^2$, where S is the mean pulsar flux density in mJy and d is the distance in kpc. Distances are estimated from the dispersion measure, assuming an electron density at z = 0 of 0.03 cm^{-3} and an electron density scale height of 1 kpc.

Manchester argues that the period distribution of pulsars is not affected by selection effects because the observed range of pulsar periods (from 33 ms to > 4 sec) lies comfortably within the short and long period cut-offs of the survey. Since the Molonglo survey did not discriminate against pulsars at high Galactic latitudes (i.e. large z) Manchester also maintains that the observed z-distribution of pulsars is a good approximation of the true distribution.

The z-distribution of pulsars is shown in Figure 6.4. It is adequately fitted by an exponential curve of scale height 350 pc. This value is surprisingly large compared with the 80 pc scale height for O-B stars, possible progenitors of pulsars, and 60 pc for SNR's.

The survey revealed a correlation between P and z. Short period pulsars have a smaller value of $|z|$ than those with long periods. This is consistent with the argument that pulsars are born close to the Galactic plane and move away during their lifetime. Because of the correlation between P and z one cannot separate ρ_P and ρ_z in equation 6.2, however Manchester contends that the survey did not seriously select against either parameter and consequently the volume V in equation 6.1

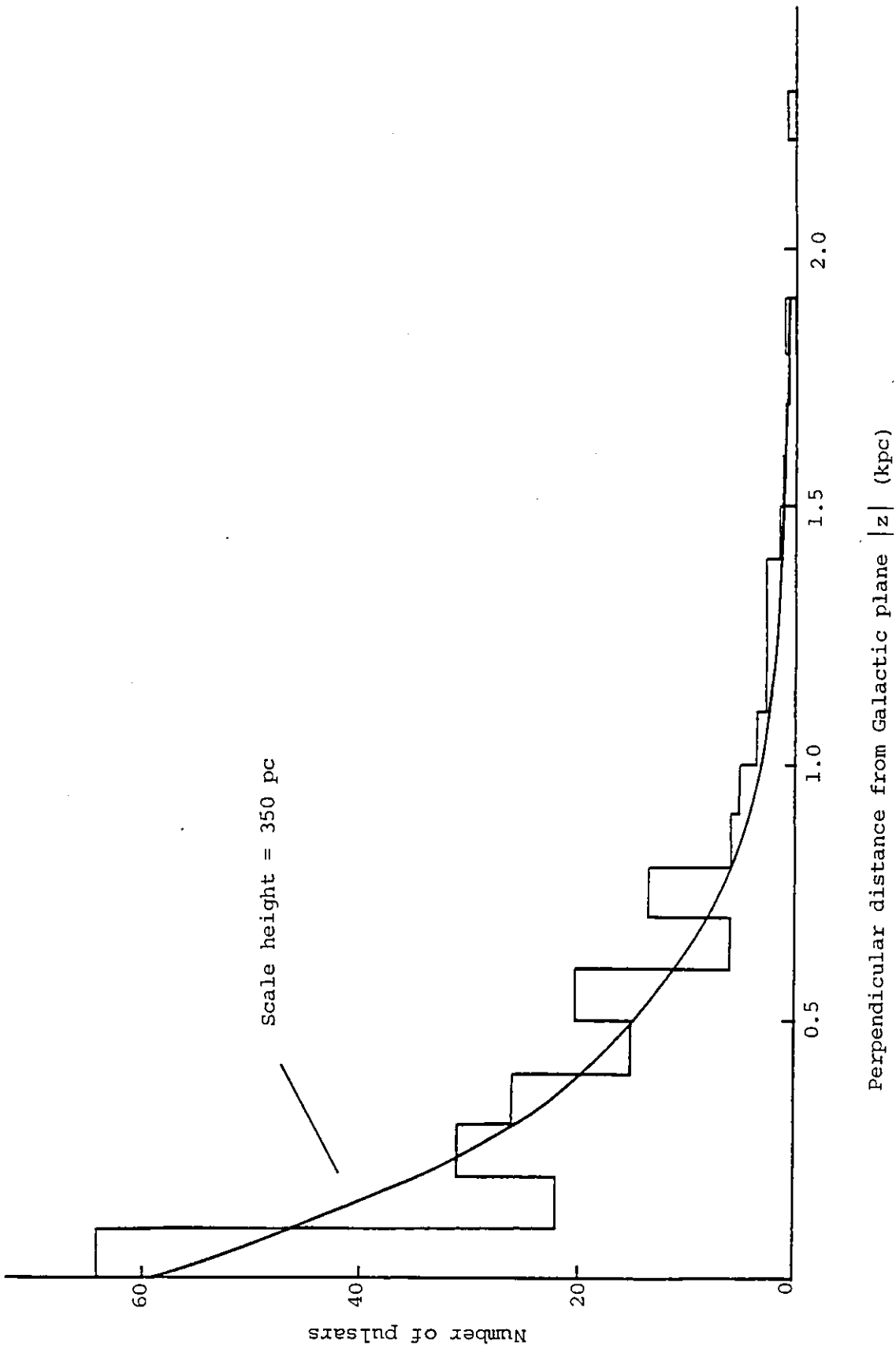

Figure 6.4 Observed distribution of $|z|$ for 224 pulsars detected in the second Molonglo survey.

is essentially independent of P and z, that is

$$V(P,z,R,L) = V(R,L)$$

The observed distributions of galactocentric radius R and radio luminosity L (shown in Figures 6.5a,b) are modified by selection effects. The peak at R ≈ 10 kpc in the radial distribution and the fall-off in the number of low luminosity pulsars are both a consequence of the limited sensitivity of the survey. To remove the selection effects, the volume V(R,L) was computed using a Monte Carlo method and equation 6.1 solved by iteration to give the logarithmic luminosity function $\phi(L) = L\rho_L(L)$ and the radial distribution $\rho_R(R)$. The two derived distributions are shown in Figures 6.6a,b. The luminosity function for pulsars in the solar neighbourhood is a power law of slope -1. The radial distribution shows that the density of pulsars decreases with galactocentric radius for R ≥ 6 kpc. (It should be mentioned here that the total number of potentially observable pulsars, obtained by integrating the radial distribution, is consistent with a pulsar birth-rate of 1 every 5 years, assuming a mean life-time for pulsars of 10^7 years, which exceeds current estimates of supernova occurrence rates.)

6.4.2 Determination of pulsar density distribution

In order to derive a pulsar density distribution of the form n(l,b,r), where l,b are the Galactic longitude and latitude respectively and r is the radial distance from the sun, density values were taken from Figure 6.6b. Values between R = 4 and R = 14 kpc only were used because the statistical errors outside this range are large. The effect of the cut-offs is small, since the area contained within 4 kpc is only 8% of the total area and, for the outer part, the fall-off in density

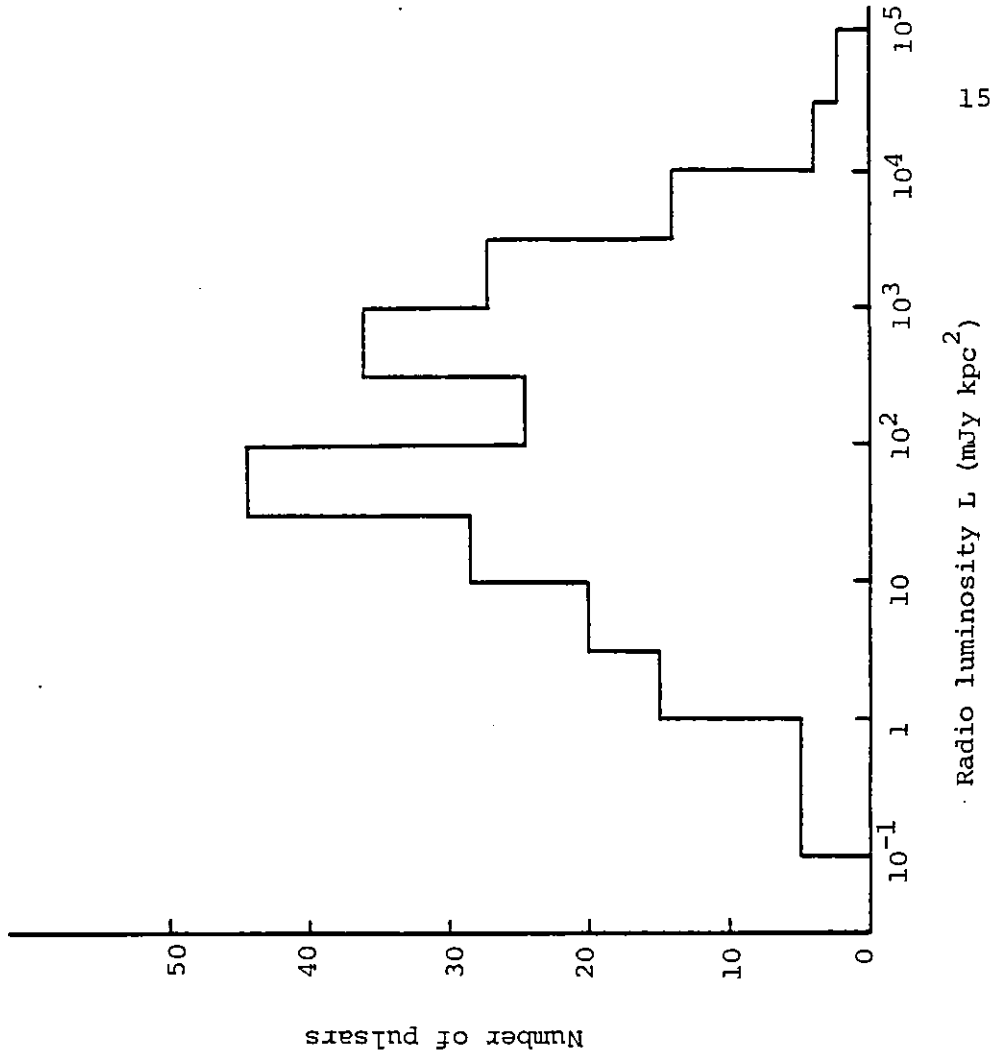

Figure 6.5b Observed distribution of radio luminosity L for pulsars.

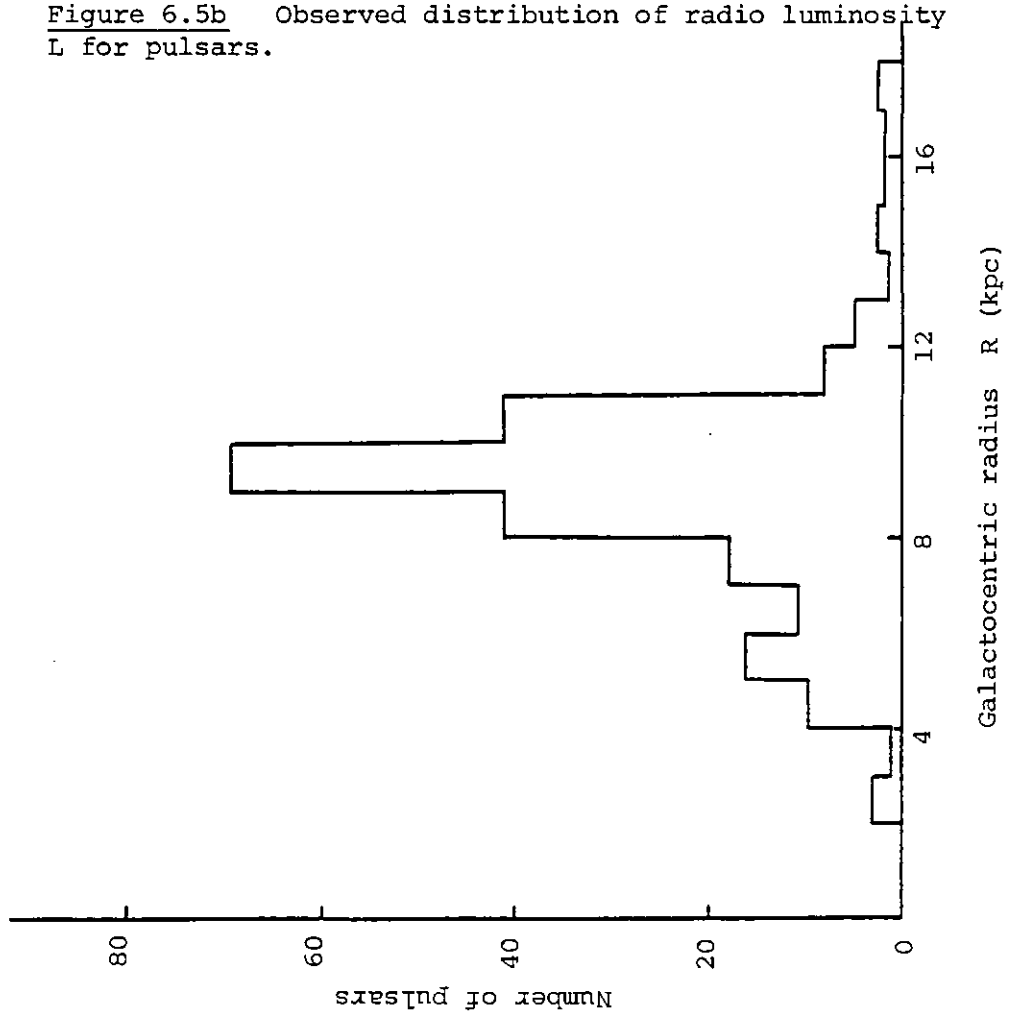

Figure 6.5a Observed distribution of galactocentric radius R for pulsars.

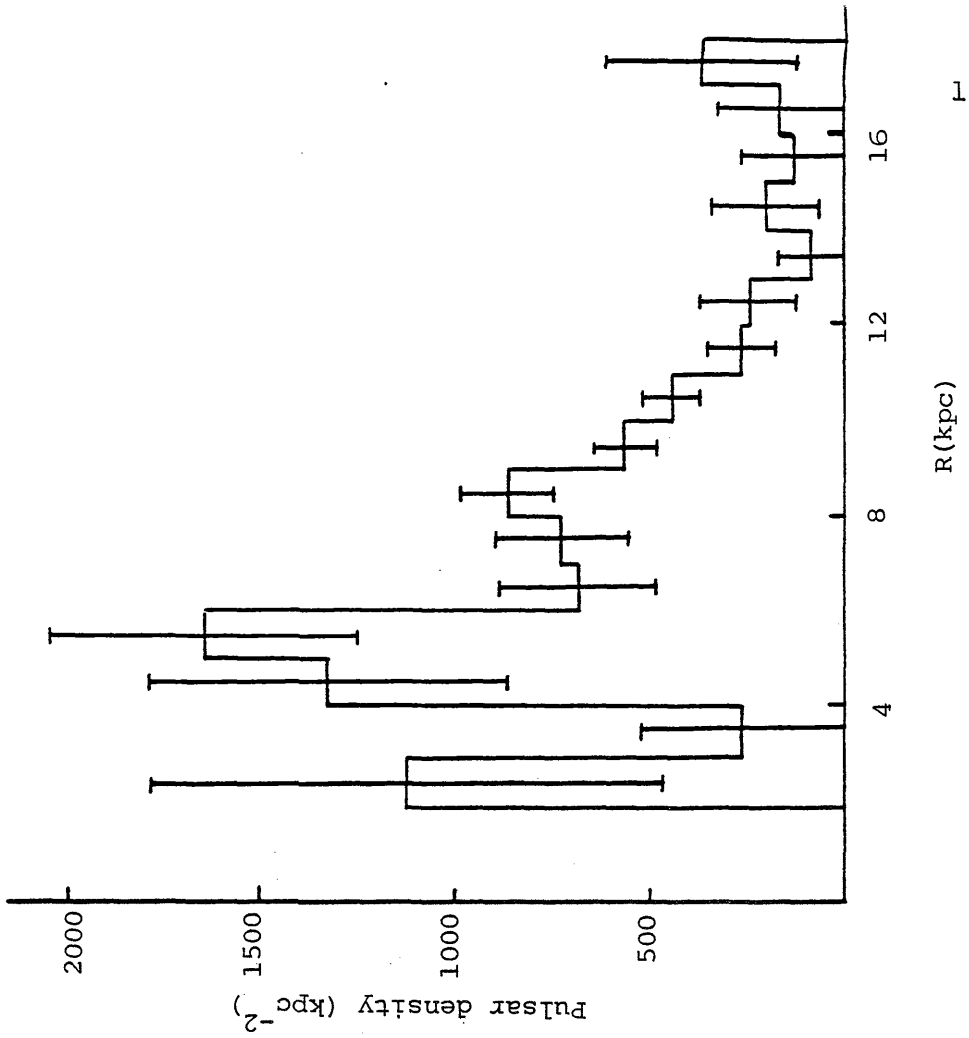

Figure 6.6b Derived radial distribution for pulsars. (Error bars denote ±σ and represent statistical errors only.)

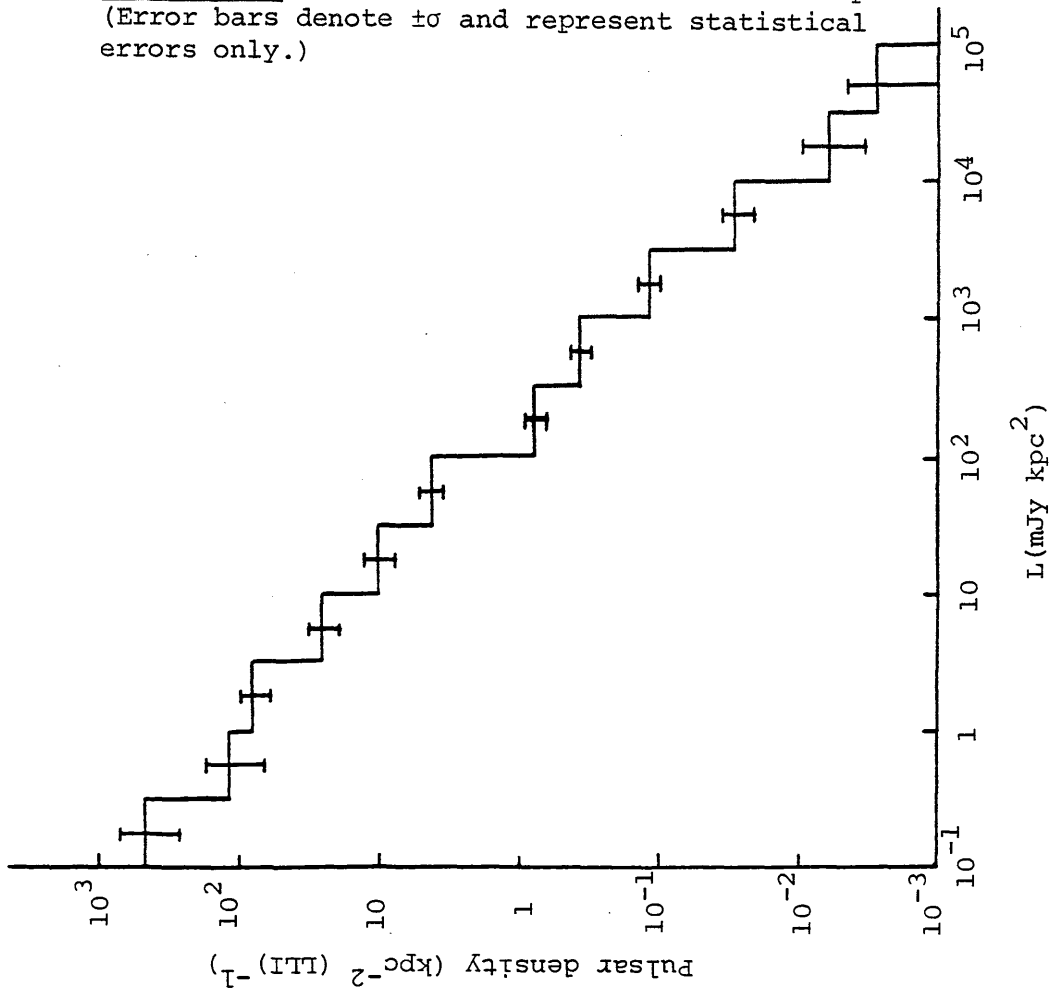

Figure 6.6a Derived luminosity function for pulsars in the local region. The ordinate gives the density of pulsars projected onto the Galactic plane per logarithmic luminosity interval (LLI).

is believed to be genuine. Table 6.1 shows the density values adopted on the equatorial plane as a function of galactocentric radius. The z-distribution of pulsars was represented by an exponential curve of scale height 350 pc, with $|z_{max}| = 1.5$ kpc. It was folded into the radial distribution to produce a density distribution N(R,z). This was transformed into heliocentric Galactic coordinates using the parametric equations :

$$z = r \tan |b| \quad \text{and}$$

$$R = (D_{GC}^2 + D^2 \cos^2 |b| - 2DD_{GC} \cos |b| \cos l)^{\frac{1}{2}}$$

where D_{GC} = Sun-Galactic centre distance (10 kpc) and

D = pulsar-sun distance

Integration over b,l in steps of 1° and 10° respectively was then performed to give the number of pulsars as a function of radial distance from the sun in 10° longitude intervals.

TABLE 6.1 DENSITY VALUES ADOPTED

Galactocentric Distance (kpc)	Equatorial Density (kpc^{-2})	Galactocentric Distance (kpc)	Equatorial Density (kpc^{-2})
4-5	1330	9-10	550
5-6	1630	10-11	460
6-7	670	11-12	290
7-8	710	12-13	250
8-9	870	13-14	130

6.4.3 Correlation of gamma emission with radio emission

The derived radio luminosity function for pulsars is a power law of slope -1. An equivalent gamma luminosity function is required, in order to estimate the total pulsar gamma-ray luminosity.

A comparison between the radio and gamma luminosities (later denoted by L_R, L_γ respectively) of pulsars is only possible for the Crab and Vela sources because these are the only two confirmed gamma emitting radio pulsars. Both pulsars have $L_\gamma/L_R = \eta_\gamma/\eta_R = 10^6$, where η_γ and η_R are efficiency parameters defined as the ratio of the gamma and radio luminosities to the known rotational energy loss rate dE/dt, E being the rotational energy of the neutron star. If the above value for η_γ/η_R were common to all pulsars, then pulsars with $\eta_R > 10^{-6}$ could not exist because η_γ cannot exceed 1. In fact, the majority of observed pulsars have $\eta_R > 10^{-6}$, as shown in Figure 6.7, which is a plot of η_R against apparent age, τ; constructed from a compilation by Taylor and Manchester (1975) and including the improved parameters of known pulsars published in the latest survey (Manchester et al, 1978). In order to estimate L_R from the observed radio fluxes Manchester has used a bandwidth of 400 MHz at 400 MHz and taken the beamwidth to be $2\pi W/P$ rads where W is the width of the radio peak and P is the pulsar period.

The anomalously high ratio η_γ/η_R ($\approx 10^6$) for the Crab and Vela pulsars implies either a) these two pulsars do not belong to the general population of pulsars or b) the ratio of efficiencies is a function of pulsar age. If b) is true, Figure 6.7 indicates that $\eta_\gamma/\eta_R \approx 10^4$ for $\tau \approx 10^6$-10^7 years, since η_R is typically 10^{-4} (a gamma efficiency of $\sim$ 1 is assumed). If this apparent fall-off in the ratio η_γ/η_R for older pulsars is genuine, then the radio efficiency must increase faster with age than η_γ.

Considering the time dependence of η_R alone, the data in Figure

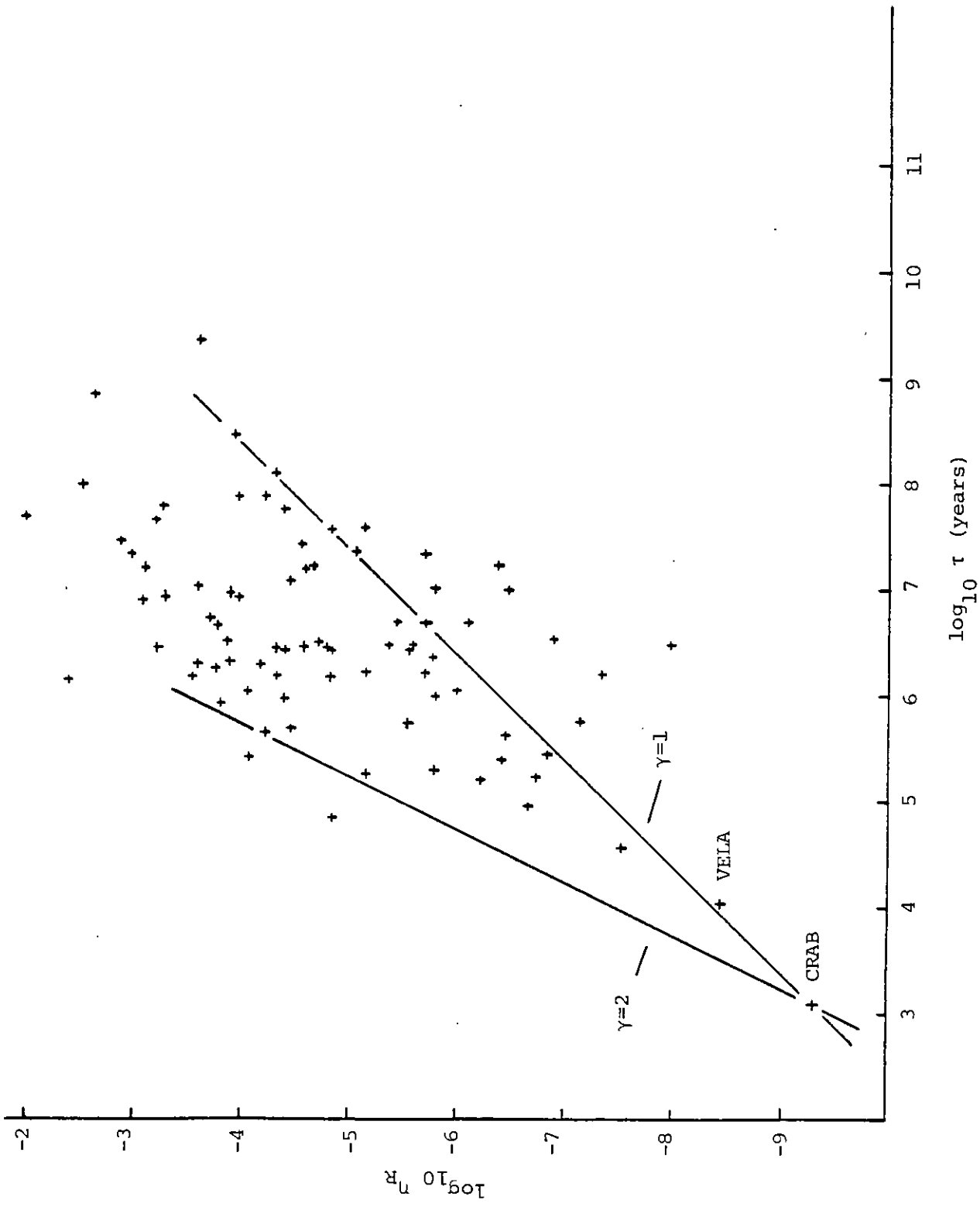

Figure 6.7 Radio efficiency η_R plotted against apparent age τ for the observed pulsars.

6.7 suggest a general trend of increasing radio efficiency with age, albeit with a rather high spread. Using the Crab and Vela as normalisation points, most pulsars are contained within the power laws of slope $\gamma = 1$ and $\gamma = 2$. A simple statistical study on the majority of pulsars (with $\tau = 10^5$-10^8 years i.e. excluding Crab and Vela) was performed. For each decade of τ, a frequency distribution of η_R was constructed and an average pulsar radio efficiency calculated. The values of $\bar{\eta}_R$, which confirm the above observation of increasing efficiency with age, are well fitted by a power law of slope 0.5 (see Figure 6.8a). Thus if Crab and Vela are typical pulsars i.e. one assumes they will evolve to become members of the main body of pulsars, the curve describing the time development of the radio efficiency would appear to flatten off after 10^5 years, as represented by the dotted line in Figure 6.8a.

The gamma efficiencies of Crab and Vela also conform to a trend of increasing efficiency with apparent age. The two data points are fitted by a power law of slope 1.35, which is slightly steeper than the theoretical prediction of ~ 1 (Ruderman and Sutherland, 1975). Again a break in the power-law time dependence of η_γ would appear to occur because the gamma-ray efficiency cannot be greater than unity, by definition. (If one extrapolates the best-fit line through the Crab and Vela points, then $\eta_\gamma = 1$ for $\tau \approx 5 \times 10^5$ years.) However, nothing can be said a priori about the behaviour of η_γ for $\tau \gtrsim 10^5$ years. The efficiency may decrease or the gamma-ray emission may indeed turn off at large values of τ, although several authors e.g. Arons (1980) believe the gamma efficiency does increase with age and reaches an asymptotic limit of ~ 1 because, it is argued, the screening effects in the pulsar magnetosphere diminish with time.

To summarise, further study of the relative dependences of η_γ

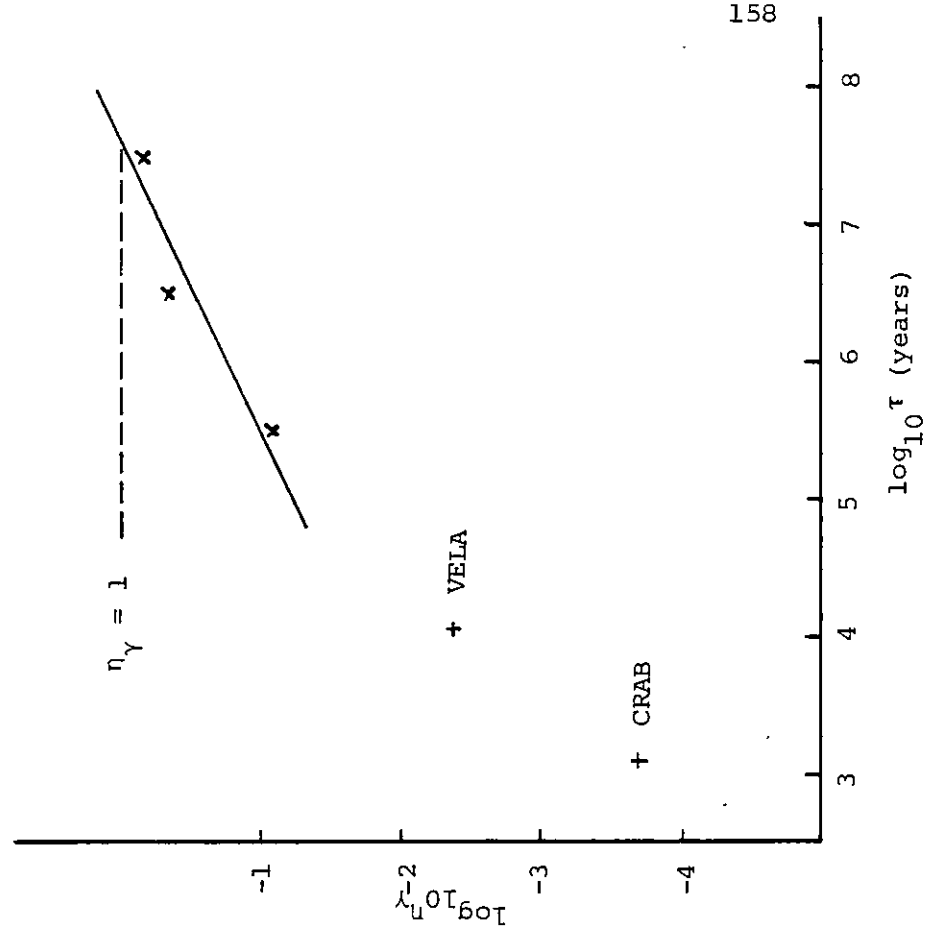

Figure 6.8b Gamma efficiency η_γ of pulsars as a function of age.

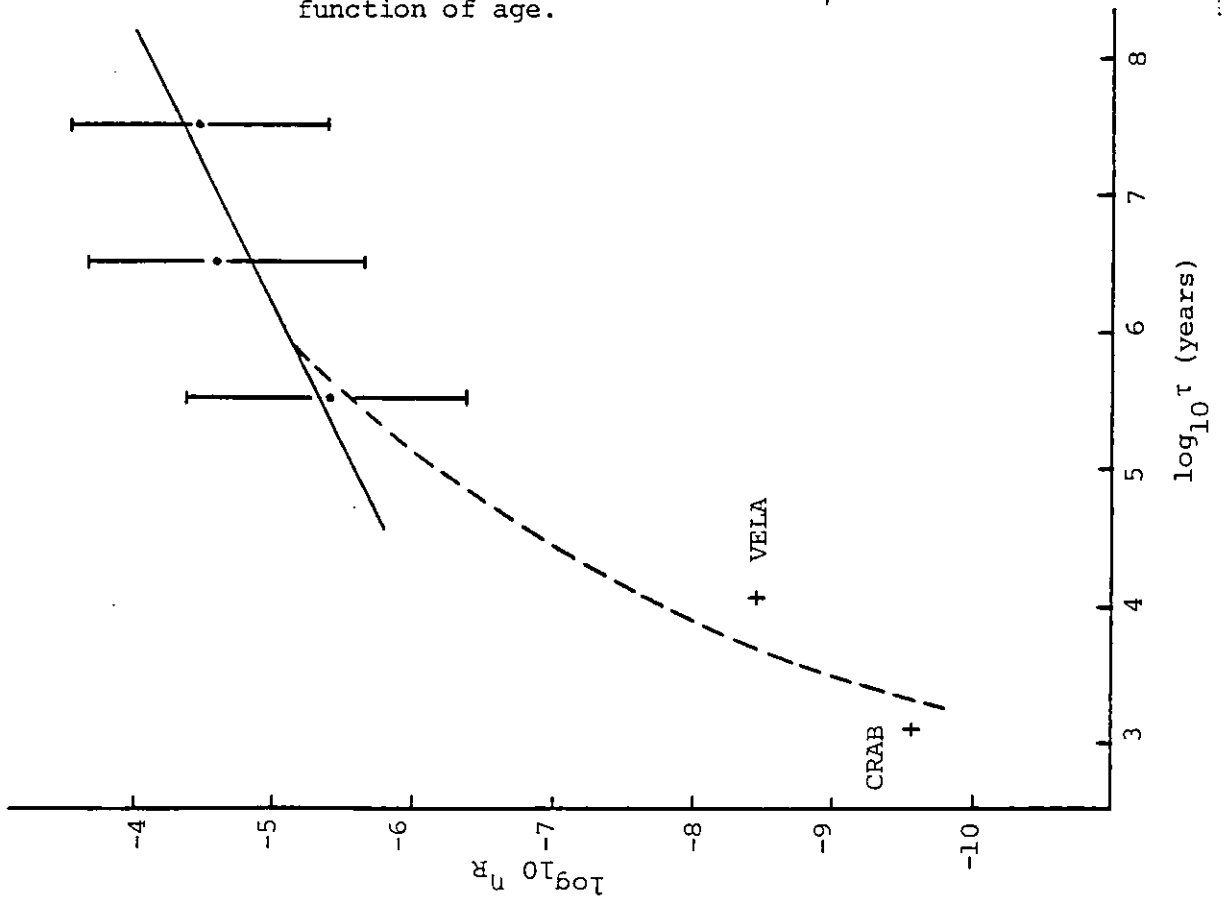

Figure 6.8a Radio efficiency of pulsars as a function of age.

and η_R on τ must await better statistics : certainly additional radio data should be forthcoming when the period derivatives of the newly discovered pulsars are measured.

6.4.4 Calculation of pulsar contribution to total gamma flux

In this analysis, two alternatives for the ratio η_γ/η_R are considered. First, η_γ/η_R is treated as a constant and secondly it is assumed to be a simple function of luminosity.

i) The assumption that η_γ/η_R is a constant may not be unreasonable given that the objective is to determine the contribution to the total gamma-ray emission from the general pulsar population, excluding the Crab and Vela whose contributions at Galactic longitudes 185° and 264° respectively are well-known. There is a possibility that the curves representing the time dependence of η_γ and η_R may flatten off after $\sim 10^5$ years and during the transition between $\tau = 10^5$ and $\tau = 10^7$ years say, the two curves may be approximately parallel. Since this range of τ includes most of the observed pulsars, it may be that η_γ/η_R is approximately the same for the majority of pulsars.

The value used for η_γ/η_R was obtained by superimposing the best fit line through the radio data points for $\tau = 10^5$-10^8 years (the power law of slope 0.5 described earlier) on to Figure 6.8b which is a plot of gamma efficiency against apparent age for the Crab and Vela pulsars. (The best-fit line is normalised to a gamma efficiency of 0.5 for $\tau = 10^7$ years.) The ratio of the gamma and radio normalisation constants ($\approx 10^4$) was used for η_γ/η_R.

The gamma-ray intensity, I_γ, of a particular number of pulsars, N, is then given by

$$I_\gamma = k_R \int_{L_1}^{L_2} \frac{\eta_\gamma}{\eta_R} L_R^{-1} \, dL_R \qquad 6.3$$

where $N = k_R \int_{L_1}^{L_2} L_R^{-1} \, dL_R/L_R$ and L_R^{-1} is the luminosity function. L_1 and L_2 are the radio luminosity cut-offs (0.1 and 10^5 mJykpc^2 respectively).

Given the pulsar distribution N(r,l = 10°), equation 6.3 was used to calculate the pulsar gamma-ray luminosity in 10° longitude intervals, after integrating over r. The flux values (typically 5 x 10^{-7} photons/cm^2 rad.sec in the Galactic centre region) indicate a pulsar contribution to the total gamma-ray flux of less than 1% in this case.

ii) Here η_γ/η_R is assumed to vary as $L_R^{1/3}$. This dependence was chosen from a consideration of the discussion in the previous section. There it was suggested that η_γ/η_R may range from 10^4 for 'old' pulsars to 10^6 (the observed value for the Crab and Vela pulsars), whereas, the spread in values of L_R spans at least six orders of magnitude. The $L_R^{1/3}$ dependence was introduced into equation 6.3 to give the gamma flux in 10° longitude intervals. The flux values ($\sim 10^{-5}$ p/cm^2 rad.sec in the GC region) were added to the emissions expected from cosmic ray interactions with atomic and molecular hydrogen, assuming a uniform cosmic ray intensity. The results are compared with the COS B data in Figure 6.9, both averaged over 10° in Galactic longitude and integrated between ± 5° in latitude. Figure 6.9 shows that the pulsar contribution, which amounts to ∿ 10% of the total Galactic flux in this case, still does not account for the broad enhancement about the Galactic centre.

This value of ∿ 10% for the pulsar contribution should be compared with ∿ 30% obtained by Higdon and Lingenfelter (1976) for the expected contribution from unresolved, short period pulsars with gamma luminosities similar to that observed from the Crab and Vela pulsars. The difference in the two values is not surprising if one

considers the pulsar data used by Manchester to derive the luminosity function, which is used in my analysis. Since 1976, very few short-period (< 100 ms) radio pulsars have been discovered, even though the various surveys maintained full sensitivity to much shorter periods. The majority of observed pulsars have periods of $\sim$ 1 sec. Consequently, most pulsars have rotational energies and, by implication, radio and gamma luminosities orders of magnitude less than the corresponding values for the Crab and Vela.

There is further evidence which seems to rule out the possibility that pulsars are significant contributors : the latitude distribution of pulsars is much wider than the corresponding distribution of high energy gamma rays.

Although it is unlikely that a pulsar contribution can explain the increased Galactic gamma-radiation between $270 < \ell < 80°$, a significant contribution from discrete sources in general is possible. COS B has detected 25 sources at energies above 100 MeV. In addition to the Crab and Vela sources, one has been identified with an extragalactic source (the quasar 3C273) and another is related to the ρ Oph dark cloud. The remaining 21 sources have no obvious counterparts at other wavelengths. From the latitude distribution, it appears that most sources are Galactic. The average distance of the sources is estimated to be 2-7 kpc (cf. with 0.5, 2 kpc for Vela and Crab respectively). They have a high gamma-ray luminosity, typically (0.4-5) x 10^{29} watts. Hermsen (1980) has investigated the possible source contribution using the latest COS B catalogue and he concludes that gamma-ray sources may contribute between 40% and 100% to the total intensity within 60° of the Galactic centre. Thus as Hermsen states the longitudinal variation of the gamma-ray emission may not require detailed models for the spatial distribution of cosmic rays and interstellar gas.

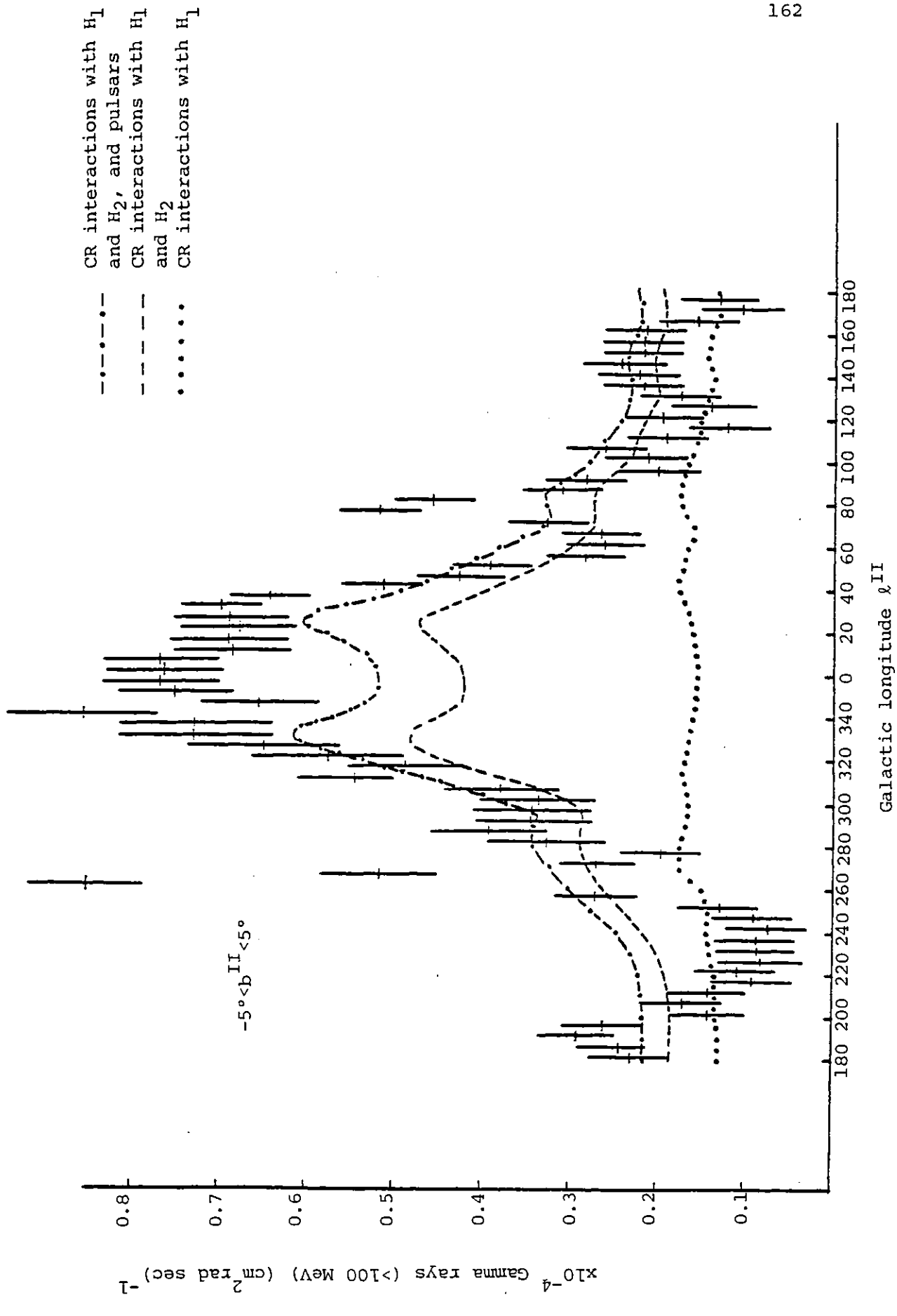

Figure 6.9 COS-B observations of high energy gamma-rays plotted as a function of Galactic longitude and compared with the combined gamma emissions expected from pulsars and cosmic ray interactions with atomic and molecular hydrogen.

REFERENCES

Anand, K.C., Daniel, R.R. and Stephens, S.A., 1968, Can.J.Phys., 46, S484.

Arons, J., 1980, IAU Symposium No.94 (Bologna), Origin of Cosmic Rays, D. Reidel Publ. Co., Dordrecht, Holland.

Bennett, K., 1973, PhD Thesis, University of London.

Bennett, K., Penengo, P., Rochester, G.K., Sanderson, T.R. and Sood, R.K., 1972, Nature, 238, 31.

Bennett, K., Scarsi, L., Bignami, G.F., Boella, G., Buccheri, R., Hermsen, W., Koch, L., Mayer-Hasselwander, H.A., Paul, J.A., Pfeffermann, E., Stiglitz, R., Swanenburg, B.N., Taylor, B.G. and Wills, R.D., 1977, 12th ESLAB Symposium on Gamma Ray Astronomy, Frascati.

Beuermann, K.P., 1971, JGR, 76, 4291.

Bignami, G.F. and Fichtel, C.E., 1974, Ap.J. Letters, 189, L65.

Byerley, A., 1975, Chelsea College, London.

Christ, H., Peters, R., Bignami, G.F., Burger, J.J., Hermsen, W., Paul, J.A., Pfeffermann, E., Taylor, B.G., Voges, W.H. and Wills, R.D., 1974, Nucl. Instr. Metho., 116, 477.

Clayton, P.G., 1975, PhD Thesis, University of London.

Erice, 1979, European Study Conference, "Gamma Ray Astronomy after COS-B".

Fazio, G.G., 1967, Ann.Rev.Astron. and Astrophys., 5, 481.

Fazio, G.G., Helmken, H.F., Cavrack, S.J. and Hearn, D.R., 1968, Can.J. Phys., 46, S427.

Fichtel, C.E., Kniffen, D.A. and Ogelman, H.B., 1969, Astrophys.J., 158, 193.

Fichtel, C.E., Hartman, R.C., Kniffen, D.A., Thompson, D.J., Bignami, G.F., Ogelman, H., Ozel, M.E. and Tumer, T., 1975, Astrophys.J., 198, 163.

Frye, G.M. and Smith, L.H., 1966, Phys.Rev. Letters, 17, 733.

Ginzburg, V.L. and Syrovatskii, S.I., 1965, Space Sci. Rev., 4, 267.

Goldreich, P. and Julian, W.H., 1969, Astrophys.J., 157, 869.

Gordon, M.A. and Burton, W.B., 1976, Astrophys.J., 208, 346.

Gould, R.J. and Schreder, G.P., 1967a, Phys.Rev., 155, 1404.

Gould, R.J. and Schreder, G.P., 1967b, Phys. Rev., 155, 1408.

Hayakawa, S., 1952, Prog.Theor.Phys., 8, 571.

Heitler, W., 1954, The Quantum Theory of Radiation, Oxford Press, London.

Hermsen, W., 1980, PhD Thesis, University of Leiden, Netherlands.

Higdon, J.C. and Lingenfelter, R.E., 1976, Ap.J. Letters, 208, L107.

Hutchinson, G.W., 1952, Phil.Mag., 43, 847.

Kanbach, G., Bennett, K., Bignami, G.F., Boella, G., Bonnardeau, M., Buccheri, R., D'Amico, N., Hermsen, W., Higdon, J.C., Lichti, G.G., Masnou, J.L., Mayer-Hasselwander, H.A., Paul, J.A., Scarsi, L., Swanenburg, B.N., Taylor, B.G. and Wills, R.D., 1977, 12th ESLAB Symposium on Gamma Ray Astronomy.

Kraushaar, W.L., Clark, G.W., Garmire, G.P., Borken, R., Higbie, P., Leong, V., and Thorsos, T., 1972, Ap.J., 177, 341.

Manchester, R.N., Lyne, A.G. and Taylor, J.H., 1978, Mon.Not.R.Astr.Soc., 185, 409.

Manchester, R.N., 1979, Austr.J.Phys., 32, 1.

McDonald, F.B., 1958, Phys.Rev., 109, 1367.

Morrison, P., 1958, Nuovo Cimento, 7, 858.

Ögelman, H.B., Fichtel, C.E., Kniffen, D.A. and Thompson, D.J., 1976, Ap.J., 209, 584.

Olsen, H., 1963, Phys.Rev., 131, 406.

Ormes, J. and Webber, W.R., 1964, Phys.Rev.Letters, 13, 106.

Paul, J., Cassé, M. and Cesarsky, C.J., 1974, 9th ESLAB Symposium on Gamma Ray Astronomy, ESO SP-106, 246.

Paul, J., Cassé, M. and Cesarsky, C.J., 1975, Proc.14th International Cosmic Ray Conference, München, 1, 59.

Perez-Mendez, V. and Pfab, J.M., 1965, Nucl.Instr.Meth., 33, 141.

Perola, G.C. and Scarsi, L., 1966, Nuovo Cimento, 66A, 718.

Quenby, J.J. and Wenk, G.J., 1962, Phil.Mag., 7, 1457.

Rossi, B. and Greisen, K., 1941, Rev.Mod.Phys., 13, 240.

Ruderman, M.A. and Sutherland, P.G., 1975, Ap.J., 196, 51.

Schlickeiser, R. and Thielheim, K.O., 1974, Phys.Letters, 53B, 369.

Schwinger, J., 1949, Phys.Rev., 75, 1912.

Sood, R.K., Rochester, G.K. and Clayton, P.G., 1974, Nucl.Instr.Meth., 117, 311.

Sood, R.K., Bennett, K., Clayton, P.G. and Rochester, G.K., 1975, Proc. 14th Int. Cosmic Ray Conf., Munich, 1, 35.

Sood, R.K., Clayton, P.G., Roff, C.E., Hughes, J.B. and Rochester, G.K., 1982, J.Phys.E. : Sci.Instrum., Vol.15, 462.

Stecker, F.W., 1971, Cosmic Gamma Rays, Mono Book Corp., Baltimore, Md.

Stecker, F.W., 1973, Astrophys. and Space Sci., 20, 47.

Stecker, F.W., 1975, Origin of Cosmic Rays, J.L. Osborne and A.W. Wolfendale (eds), D. Reidel Publ. Co., Dordrecht, Holland.

Stecker, F.W., Solomon, P.M., Scoville, N.Z. and Ryter, C.E., 1975, Ap.J., 201, 90.

Sturrock, P.A., 1971, Ap.J., 164, 529.

Taylor, J.H. and Manchester, R.N., 1975, Astron. J., 80, 794.

Taylor, J.H. and Manchester, R.N., 1977, Ap.J., 215, 885.

Thompson, D.J., 1974, JGR, 79, 1309.